HYDROTHERMAL SYNTHESIS, CHARACTERISATION AND PHOTOCATALYTIC ACTIVITY OF TUNGSTEN(VI) OXIDE NANOWIRES CO-DOPED WITH CHLORINE AND CALCIUM

BY

ONOGWU, Sarah Udenyi
(MTech/SPS/2018/7989)

DEPARTMENT OF CHEMISTRY
SCHOOL OF PHYSICAL SCIENCES
FEDERAL UNIVERSITY OF TECHNOLOGY MINNA

OCTOBER, 2023

ABSTRACT

This research focused on the synthesis, characterisation and photocatalytic behavior of chlorine and calcium co-doped tungsten(VI) oxide nanowires composites for the removal of reactive dye and selected heavy metals from indigenous dyeing wastewater. Response Surface Methodology optimization based on Box –Behnken Design was employed for the hydrothermal synthesis of WO_3 nanowires where sodium-tungstate and oxalic acid were used as precursors. Nacl and Ca (NO_2 salt acted as structure directing agent and dopants and were mixed at different ratios to prepare Cl-Ca co-doped WO_3 nanowires composites through one pot- wet-hydrothermal method. The prepared WO_3 based nanowires were characterised for their absorption band, morphology, elemental composition, microstructure, mineral phase and surface area. The UV-Visible spectroscopy showed the reduction of band gap energy from 2.7 eV for undoped WO_3 to 2.2 eV for 4c:1a co-doped WO_3 nanocomposites. HRSEM/HRTEM, analysis confirmed that the synthesized WO_3 were monoclinic, highly crystalline, compacted spherical shaped nanowires with a diameter between 104.5 nm – 125.nm. The EDS revealed W and O as the dominant element irrespective of the synthesis conditions for pure WO_3. The EDS results for the co-doped samples revealed W, O as the dominant elements and Ca, Cl in varying amounts. The HRSEM/HRTEM results of the Cl-Ca co-doped WO_3 showed morphological changes and the formation of large and narrow bundles nanowires of different length depending on the Cl-Ca mixing ratio. The XRD analysis demonstrated phase change from monoclinic to triclinic due to the presence of Cl and Ca in the lattice layers of WO_3 nanowires composite. XRD pattern of the doped-WO_3 suggests that all the peak positions shifted to a lower diffraction angle due to the expansion of the lattice of WO_3. BET analysis revealed an appreciable increase (4.216 m^2 g^- - 16.031 m^2g^{-1}) in surface area as the dopants was introduced which suggested existence of synergistic effect between the two dopants. The removal efficiency of reactive dye in the dyeing wastewater via batch photoreaction method was 35, 55, 60, 90, & 94 for WO_3, 1c:1a, 1c:2a, 2c:1a & 4c:1a respectively at contact time of 240 min. The percentage Chemical Oxygen Demand (COD) removed was 28, 47, 50, 80, and 90 for WO_3, 1c:1a, 1c:2a, 2c:1a & 4c:1a respectively. The order of performance of the nanomaterials with respect to the removal of target pollutants was: pure WO_3 < 1c:1a < 1c:2a < 2c:1a < 4c:1a for both reactive dyes and COD due to the differences in their crystallite size and surface area. The experimental data best suited to Pseudo second-order and the study demonstrated that the catalyst Cl-Ca-WO_3 with mixing ratios (4:1) was reusable after fifth cycles and can be used for the removal of the target pollutants.

TABLE OF CONTENTS

Content	Page
Cover page	i
Title page	ii
Declaration	iii
Certification	iv
Dedication	v
Acknowledgements	vi
Abstract	viii
Table of contents	ix
List of Tables	xii
List of Figures	xiii
List of Plates	xv
Lists of Abbreviations	xvi
CHAPTER ONE	1
INTRODUCTION	1
1.1 Background of the Study	1
1.2 Statement of the reearch problem	5
1.3 Justification of the study	7
1.4 Aim and Objectives of the study	8
1.5 Scope of the Study	8

CHAPTER TWO 9

LITERATURE REVIEW 9

2.1 Photocatalytic Technology 9

2.2 Mechanism of Heterogenous Photocatalysis 10

2.3 Tungsten Oxde (WO_3) Nanowires 13

2.3.1 Shortcomings of WO_3 nanowires 15

2.3.2 Doping of WO_3 nanowires with metals & doping of WO_3 nanowires with non-metals 16

2.4 Methods of Syntheizing WO_3 nanowires 18

2.4.1 Hydrothermal Method 19

2.5 Characterisation Methods 23

2.5.1 UV-Visible Spectroscopy 23

2.5.2 High Resolution Scanning Electron Microscopy (HRSEM) 24

2.5.3 High Resolution Transmission Electron Microscopy (HRTEM) 25

2.5.4 Energy Dispersive X-Ray Spectra (EDS) 25

2.5.5 Selected Area Electron Dffraction (SAED) 26

2.5.6 X-Ray Dffraction 26

2.5.7 Branauer Emmett & Teller (BET) 27

2.6 Indigenous dyeing wastewater 28

2.6.1 Health & Environmental Impact of local dyeing wastewater 28

2.6.2 Reactive dyes 29

2.6.3 Heavy metals in dyeing wastewater 30

2.7 Chapter Summary & Research gaps 30

CHAPTER THREE 31

MATERIALS AND METHODS 31

3.1 Materials 31

3.1.1 Sampling & Sample Pretreatment 32

3.2 Hydrothermal Synthesis of Nanowires 34

3.2.1 Hydrothermal synthesis of WO_3 nanowires 34

3.2.2 One-pot Hydrothermal synthesis of chlorine - calcium co-doped WO_3 nanowires 35

3.2.3 Characterisation of synthesized WO_3 and Cl-Ca/co-doped WO_3 nanowires 35

3.2.3.1 Identification of Minerelogical Phase 35

3.2.3.2 Morphological arrangement and elemental composition analysis 36

3.2.3.3 Microstructure and crystalline analysis 36

3.2.3.4 Absorption Band determination by UVVisible spectroscopy 36

3.2.3.5 Surface Area Evaluation by BET 37

3.2.4. Physico-chemical assessment of the wastewater 37

3.2.4.1 Determination of pH 37

3.2.4.2 Determination of Biological oxygen Demand (BOD) 38

3.2.4.3 Determination of Chemical oxygen Demand (COD) 38

3.2.4.4 Determination of Total organic Carbon (TOC) 39

3.2.4.5 Identification of Azo dye in Indigeneous dyeing wastewater 40

3.2.4.6.Determination of heavy metals in the Indigeneous dyeing wastewater 40

3.2.5 Blank and control experiment 41

3.2.5.1 Adsorption Process 41

3.2.5.2 Photocatalytic activity of the synthesized WO_3, Cl/Ca-codoped nanowires 41

3.2.6 Data Analysis 42

3.2.6.1 Zero-order reaction expression 43

3.2.6.2 First-order reaction expression 43

3.2.6.3 Second-order reaction expression 43

3.2.7 Regeneraton and Reuseability Studies 43

CHAPTER FOUR 45

RESULTS AND DISCUSSION 45

4.1 Characterisation of undoped WO_3 Nanowires 45

4.1.1 UV-visible absorption and band gap energy determination 45

4.1.2 XRD Analysis of undoped WO_3 based nanowires 50

4.1.3 XRD Pattern of Chlorine and Calcium of co-doped WO_3 nanowires 52

4.1.4 HRSEM analysis of the undoped WO_3 nanowires synthesized at different conditions 55

4.1.5 HRSEM analysis of chlorine and calcium co-doped WO_3 nanowires 58

4.1.6 EDS analysis of the undoped WO_3 nanowires 60

4.1.7 EDS analysis of the Cl-Ca doped WO_3 nanowires 63

4.1.8 HRTEM analysis and SAED Pattern of the undoped WO_3 nanowires 64

4.1.9 BET results of synthesized undoped WO_3 and doped 4c:1a, 2c:1a nanowires 67

4.1.10 Physico-chemical characterisation of Indigeneous dyeing Wastewater. 70

4.1.11 Photocatalytic Degradation 74

4.2 Heavy metals analysis in the treatment wastewater 79

4.3 Kinetics study 83

4.4 Reaction mechanism of the Enhanced WO_3 Photocatalyst 87

4.5 Reuseability/Stability studies 88

4.5.1 XRD analyssis after Photodegradation 88

CHAPTER FIVE 91

CONCLUSION AND RECOMMENDATIONS 91

5.1 Conclusion 91

5.2 Recommendations 93

5.3 Contribution to Knowledge 93

REFERENCES 95

APPENDICES 106

LIST OF TABLES

Table	Page
2.1 Semiconductor Photocatalyst and their corresponding Band gap energy	12
3.1 List of chemical/reagents	32
3.2 List of Analytical Equipment	33
3.3 Box-Behnken Design employed in the synthesis of WO_3 nanowires	34
4.1 Calculated band gap of the undoped and co-doped WO_3 nanowires	48
4.2 Elemental composition of the undoped nanowires	59
4.3 Elemental composition of the doped nanowires	63
4.4 BET surface area, pore size and pore volume of doped and undoped samples	68
4.5 Physico-chemical characterization of the Indigenous dyeing wastewater	69
4.6 Comparison of the Photocatalytic Performance with Previous studies and this study	77
4.7 Heavy metal concentration in Raw and Treated Wastewater samples	79
4.8 Kinetic Parameter for reactive dye degradation as an indicator Parameter from Dye Wastewater	82
4.9 Kinetic Parameter for (Chemical Oxygen Demand) COD degradation as an indicator Parameter from Dye Wastewater	84

LIST OF FIGURES

Figures	Page
2.1 Mechanism of Heterogeneous Photocatalysis	10
2.2 The Cubic Phase of c-WO_3	14
2.3 The Monoclinic Phase of γ-WO_3	15
4.1 UV-spectrum of the undoped WO_3 nanowires prepared at different synthesis conditions	44
4.2 UV-spectrum of doped sample at 1c:1a of the dopants	45
4.3 UV-spectrum of doped sample at 1c:2a of the dopants	45
4.4 UV-spectrum of doped sample at 2c:1a of the dopants	46
4.5 UV-spectrum of doped sample at 4c:1a of the dopants	46
4.6 Band gap plot of the undoped and doped sample	48
4.7 XRD pattern of WO_3 prepared at different conditions	50
4.8 XRD patterns of Cl and Ca doped WO_3 nanowires at different mixing ratios	52
4.9 Elemental composition of undoped nanowires prepared at 1 mol/dm^3, 200 ^oC and 1h 30 min	60
4.10 Elemental composition of undoped nanowires prepared at 1mol/dm^3, 140^oC and 2 h 30min	60
4.11 Elemental composition of undoped nanowires at 0.55 mol/dm^3, 200^oC and 2 h 30 min	61
4.12 EDS analysis of the Cl & Ca doped WO_3 nanowires	62
4.13 BET plot of Undoped WO_3	63
4.14 BET plot of doped sample (2c:1a)	67
4.15 BET plot of doped sample (4c:1a)	67
4.16 UV-Visible Spectrum of the raw wastewater	71

4.17 Comparison of the reactive dye degradation efficiency 74

4.18 Comparison of the COD degradation efficiency 75

4.19A Effect of contact time on the adsorption of metal ions using WO_3 80

4.19B Effect of contact time on the adsorption of metal on using 2c:1a 80

4.19C Effect of contact time on the adsorption of metal ions by using 4c:1a 81

4.20 XRD Pattern of the 4c:1a before & after photocatalytic degradation of the wastewater 88

4.21 Reusability tests of 4c:1a nanowires 89

LIST OF PLATES

Plates	**Page**
I- HRSEM Micrographs of the undoped WO_3 nanowires	55
II-IIHRSEM Micrographs of the doped WO_3 nanowires	57
III-HRTEM Micrographs of undoped and doped WO_3 nanowires	64

LIST OF ABBREVIATIONS

BET	Brauneur Emmett Teller
HRSEM	High Resolution Scanning Electron Microscopy
HRTEM	High Resolution Transmission Electron Microscopy
UV/VISIBLE	Ultraviolet Visible Spectroscopy
XRD	X-ray Diffraction

CHAPTER ONE

INTRODUCTION

1.1 Background of the study

Industrial growth and development have been linked to the production of various products such as foods, drug, cosmetic, agricultural, textile and other products some of which are for human consumption to improve their standard of living (Pona *et al*., 2021). Most of these industrial operations usually lead to generation of wastewater that depletes water quality in the environment. In Nigeria, the numbers of local dyeing industries have increased due to the total folding up of the existing textile industries in different part of the country. Dyeing of plain fabric with different organic dyes for a predetermined period of time is simple with no special skills and the dyeing activities have created millions of jobs for the teaming youths and even elderly ones. As at today, the demand for dyed clothes and their acceptance among the citizens continue to increase.

On the other hand, wastewater generated during dyeing and printing of fabrics contain several unreacted toxic dyes such as reactive dyes, methylene blue, methyl orange, rhodamine B, congo red, disperse violet 26 and crystal violet which are harmful to human health (Dutta *et al*., 2021). Reactive dyes which are the focus of this study are consistently used in various applications such as pharmaceutical, cosmetics, food, paper, and leather and textile industries.

In particular, Indigenous or local dyeing wastewater generated usually have high alkaline pH, residual color, total suspended solids (TSS), high amount of chemical oxygen demand (COD), biochemical oxygen demand (BOD), total organic carbon (TOC)(Baba *et al*.,2020)

and heavy metals and salts (Yassen and Scholz, 2018). Thus, direct release of such wastewater into the surroundings (neighboring soils and ditches) affect the soil quality and increase its susceptibility to erosion, resulting to low productivity and decrease food chain supply (Baba *et al*.,2020). Most of these dyes especially the reactive types have teratogenic and mutagenic effects on both aquatic and human lives; and also cause kidney disease in human (Dutta *et al*., 2021).

Over time, several methods have been employed for the treatment of indigenous dyeing wastewater which include physiochemical and chemical methods such as coagulation, flocculation, electrocoagulation (Michel *et al*., 2019), adsorption technology (Abidemi *et al.*, 2019),photo Fenton process (Muszynski *et al*., 2019), ultrafiltration (Cao *et al*., 2020), ion exchange (Maslova *et al*.,2020), membrane separation (Ibrahim *et al*., 2020), filtration (Azam *et al*., 2021), electro dialysis (Min *et al*., 2021) and biological methods. However, these methods have shortcomings such as high cost of maintenance, low efficiency, high energy consumption, use of sophisticated equipment and time consuming (Silveira *et al*., 2020). Additionally, the generation of toxic sludge during the process and occupation of space by the sludge is also considered another problem. Hence, the need to develop advanced and environmentally - benign method based on the use of Nano-based material for the removal and degradation of toxic contaminants from indigenous dyeing wastewater.

Heterogeneous semiconductors metal oxides such TiO_2, ZnO, CdS, WO_3 nanowires are capable of degrading a wide variety of organic pollutants found in wastewater (Jamjourn *et al*., 2021)). The metal oxides behave as catalyst under light sources causing an induction of a charge separation process followed by the generation of electron-hole pair capable of

oxidizing organic substrates onto their surfaces into harmless compounds. Tungsten(VI) oxide (WO_3) is a semiconductor metal oxide that has gained wider research interest due to its uniqueness as a photocatalyst (Nagyne-kovacs *et al*., 2019), effective as a gas sensor, used as an electrochromic device, secondary batteries and an electrocatalytic oxygen evolution (Wang *et al*., 2020) Also, due to its unique morphology as one dimensional (1D) photocatalyst, WO_3 nanowires have advantage of improved stability and activity compared to its zero dimensional (0D) nanoparticles. WO_3 nanowire is physio-chemically stable, mechanically robust in aqueous solutions has high surface to volume ratio, improved surface scattering of electrons and photons and considered to be non-toxic (Razali *et al*., 2021). Depending on the temperature, WO_3 exist in different phases which include monoclinic (γ-WO_3), triclinic (δ-WO_3), orthorhombic (β-WO_3) and tetragonal (α-WO_3). Furthermore, due to its high band gap (2.7- 2.8 eV) they are capable of absorbing ultraviolet light (Ofori *et al*., 2015) and also has high stability of destroying contaminants of both natural and manmade (Maleki *et al*., 2019).

Various methods have been employed in the synthesis of WO_3 nanowires. These include spray pyrolysis (Leng *et al*., 2019), vapor–liquid-solid (VLS) (Wang *et al*., 2013), vapor transport (Liu *et al*., 2013), solid phase reaction (Lee *et al*., 2014; Ma *et al*., 2017), solvothermal (Guo *et al*., 2016), and hydrothermal (Tehrani *et al*., 2020). Of all these methods, the hydrothermal method is considered simple and most versatile method of synthesizing nanowires from aqueous solutions under controlled temperature and pressure. Hydrothermal method is widely used because water is usually employed as a solvent during synthesis (Wu *et al*., 2019). However, WO_3 has a very weak photocatalytic activity in the visible region due to its fast recombination of photogenerated electron–hole pairs which

results in low quantum efficiency (Mohagheghian *et al.*, 2017). Hence, there is need to improve and extend the absorption threshold of WO_3 nanowires to the visible region through incorporation of metals, non-metals, and metalloids via a process known as doping. Doping simply means the incorporation of foreign impurities like metal or non-metals ions onto the lattice layer of a semiconductor in order to improve its photocatalytic property. (Kahng *et al*., 2019). Metal ion dopants enhances photocatalytic activity in the visible region by direct contact between the metal and the semiconductor metal oxide which lead to the formation of an electric field based on electron transfer between the two substrates according to Fermi level difference (Silveira *et al*., 2020). The interaction usually results to the shifting of energy band edge and reduction of electron – hole recombination rate (Kahng *et al*., 2019). In non – metal doping, the dopants raise the maximum valence band edge of the semiconductor metal oxide and causes significant narrowing of the band gap energy. Due to the large ionic size of calcium as an s-block element than the host atom (tungsten) it is suitable for doping because it is capable of stabilizing the lattice system and strengthen the chemical bonds in WO_3 (Pradana *et al*., 2018). Chlorine as a p-block element can substitute oxygen ions (O^{2-}) in WO_3 lattice system due its electronegativity and hence increase the surface acidity of WO_3 and consequently making it a stable and efficient catalyst for photoactivity in the visible region (El-yazeed *et al*., 2020).

In the course of time, researchers have employed conventional optimization of synthesizing metal oxide nanoparticles where one factor is varied and others variable are kept constant. This approach is expensive, time consuming and often resulted to wastage of chemicals (Vakilinezhad *et al*., 2018). In recent times attention has been shifted to the optimization of synthesis procedure using statistical design of experiment (DOE) involving response surface

methodology (RSM) (Behzadi *et al*., 2020). RSM is highly effective, saves time especially with minimum number of experiments based on the interactive effects of different process parameters (Talebi *et al*., 2017). Thus, in this study, Response surface methodology optimization based on Box–Behnken Design (BBD) was employed for the synthesis of WO_3 nanowires and Chlorine-Calcium co-doped WO_3 nanowires via hydrothermal method. The undoped and doped prepared nanowires were characterised using different analytical techniques. The adsorptive and photocatalytic behavior of Chlorine-Calcium co-doped WO_3 nanowires for the removal and degradation of reactive dyes in indigenous dyeing wastewater was also examined. The reusability potential of the prepared chlorine-calcium co-doped Tungsten (VI) oxide nanowires was also examined.

1.2 Statement of the Research Problem

One major source of water pollution has been linked to intermediate products and sometimes the unreacted raw materials in the wastewater discharged into various water bodies. Globally, the textile industry is known to use large volume of water more than any other industry. An average sized textile mills consume about 200Litres of water per kg of fabric processed per day (Navin *et al*., 2018). Indigenous dyeing industry also used approximately 80 Litres of water per day and discharge same volume of untreated water into the environment. The dyeing wastewater is characterised by relatively high chemical oxygen demand (COD) values due to the presence of different types of dyes, high amount of total suspended solids (TSS), high amount of biochemical oxygen demand (BOD), total organic carbon (TOC), heavy metals and salts.

The presence of pollutants in dye wastewater has been considered to have human health related effects such as skin degeneration, allergic reactions, nausea, asthma, liver and kidney dysfunction. The conventional methods of treating dyeing wastewater such as coagulation, dissolved air floatation, submerged membrane, biological e.t.c do not efficiently remove these dyes completely and the likely formation of toxic sludge during the process often occur.

Undoped WO_3 with a narrow band gap of 2.7 – 2.8 eV has weak photocatalytic activity in the visible region and thus recombination of the photo generated charge carriers is likely to occur. These photo generated charge carriers do not participate in the redox process that takes place at the surface of WO_3, hence researchers have focused on doping with metal or nonmetals. Monodoping with either metals or non-metals alone has been reported to create defects in semiconductor metal oxides for example creating oxygen vacancies which can act as a recombination site which can lead to decrease in the photocatalytic activity (Kahng *et al*., 2019). Furthermore, high concentration of non-metal dopants in WO_3 often results to a decrease in photo activity. Heavy metals such as Pb, Cu, Ni and Cd and others present in wastewater have environmental effects and also adverse effect on humans. The presence and exposure to these metals has been reported to cause various health issues such as respiratory issues, skin rashes, weak immune systems, chest pain and renal failure amongst others (Mood-Balali *et al*., 2021).

1.3 Justification of the Study

In order to continuously improve and sustain the standard of living of people especially in the urban areas, there is need to address the issue of water pollution and one way to do that

is to encourage the treatment of wastewater before they are being discharged into the environment.

The synthesis of 1D WO_3 nanowires using an inorganic salt via hydrothermal method for photocatalytic degradation of water pollutants (complex organic structure dyes) has been identified as a green cleanout non-toxic sludge generation technology compared to other conventional methods. The synthesis of 1D WO_3 nanowire via the hydrothermal method is less complicated, requires low process temperature and expected to give nanowires a well crystallized and controlled particle size (Ahmadian *et al*., 2019).

Doping of WO_3 nanowires with calcium and chlorine is further expected to reduce the band gap energy of the host material and give rise to a higher photocatalytic activity in the visible region than the undoped WO_3 nanowires. Co-doping WO_3 with s-block element (calcium) and p-block element (chlorine) is expected to create more energy levels in the conduction band and valance band followed by narrowing of its band gap and thus improve it photocatalytic activity.

Application of semiconducting chlorine-calcium co-doped WO_3 nanowires as an adsorbent/photo catalyst platform in environmental remediation is expected to lower the COD, BOD, TOC, DO values in the dyeing wastewater to tolerable limits thereby reducing the fundamental ecological problem.

1.4 Aim and Objectives of the Study

The aim of the study was to synthesise and characterise chlorine and calcium co-doped WO_3 nanowires for the photocatalytic degradation of reactive dyes and selected heavy metals

removal in indigenous dyeing wastewater. The aim was achieved through the following objectives which are;

i. Synthesis of Tungsten trioxide (WO_3) nanowires from Sodium tungsten dihydrate and oxalic acid precursor based on Box-Behnken Design via hydrothermal method
ii. Synthesis of Chlorine-Calcium co-doped Nanowires (Cl-Ca/WO_3) via a combination of wet impregnation- hydrothermal methods.
iii. Characterisation of the synthesized WO_3, and Cl-Ca/WO_3 nanowires using Ultraviolet-Visible Spectroscopy, High Resolution Scanning Electron Microscope (HRSEM), Energy Dispersive Spectroscopy (EDS), High Resolution Transmission Microscope (HRTEM), X-ray Diffraction (XRD), Brunauer-Emmett-Teller (BET) N_2 adsorption-desorption method.
iv. Application of the synthesized WO_3, Cl-Ca/WO_3 nanowires for the photocatalytic degradation of the organic molecules and the heavy metal removal in the dyeing wastewater under visible-light.
v. Evaluation of experimental data using different kinetic models and examine the regeneration potentials of the synthesized WO_3, Cl-Ca/WO_3 nanowires.

1.5 Scope of the Study

This research was limited to the hydrothermal synthesis of WO_3, and Cl-Ca /WO_3 nanowires and its characterisation. It also evaluates the photocatalytic activities of the synthesized nanowires for the treatment of indigenous dyeing wastewater

CHAPTER TWO

LITERATURE REVIEW

2.1 Photocatalytic Technology

The field of photocatalysis has been a subject of considerable investigation among researchers for quiet some decades due to the simplicity in design, environmental friendliness, ease of operation at ambient temperature (Zhang *et al*., 2019). Photocatalytic technology has been recognized as a potential approach to water and wastewater remediation, air purification, paint production, bio tissues and biosensors generation (Belver *et al*., 2019). The term "photocatalysis" is often referred to the activation of a chemical process by solid photocatalyst through irradiation by UV or visible light source (Belver *et al*., 2019). During this process, incident light interacts with the surface of a solid catalyst prompting the movement of electron from valence band to conduction band and a subsequent generation of an electron-hole (e^-/h^+) pair especially when energy of the photon of light is equal or higher than the band gap(E_g) of the semiconductor material in question. In photocatalysis, the rate of reaction depends on the frequency of the irradiated light which acts as an initiator of the photoreaction (Imitiaz *et al*., 2019). Photocatalysis has wide range of applications in the field of material science which includes removal or degradation of organic and inorganic species from gas phase or aqueous systems for environmental clean-up, purification of water, industrial and health applications (Xu, 2021). However, the two most significant applications of photocatalysis are in solar water splitting and the treatment of air and water containing atmospheric and organic pollutant (Koe *et al*., 2019).

Depending on the phase differences of the reactants and catalysts, semiconductor photocatalysis can be classified into two types namely; homogeneous photocatalysis and

heterogeneous photocatalysis. Hence, for the sake of this research, the latter will be focused on heterogeneous photocatalysis which is described as a process which includes large varieties of reactions such as reduction-oxidations, dehydrogenation, and transfer of charge carriers, bacterial inactivation, organic pollutant degradation, water detoxification or purification under both UV and visible light irradiation (Xu, 2021) Examples of such photocatalysts are the noble metals such as platinum (Pt), palladium (Pd), ruthenium (Ru) and rhodium(Rh) and transition metal oxides such as titanium (TiO_2), zinc (ZnO), tungsten(WO_3) and others (Koe *et al*.,2019).

2.2 Mechanism of Heterogeneous Photocatalysis

The mechanism of heterogeneous photocatalysis involves seven key processes taken place simultaneously as shown in Figure 2.1.

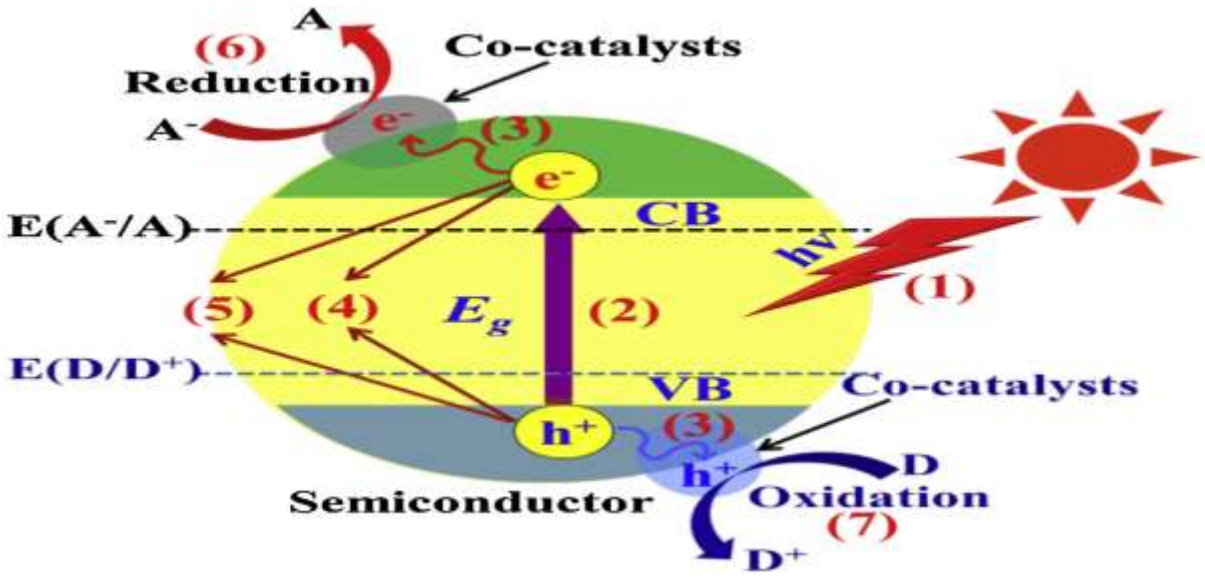

Figure 2.1. Mechanism of heterogeneous photocatalysis showing the various stages: (1) light incidence; (2) charge excitation; (3) charge separation and transfer; (4) bulk charge recombination; (5) surface charge recombination; (6) surface reduction reactions; and (7) surface oxidation reactions (Wen *et al*., 2016)

These reaction steps include: incidence of light (stage 1), charge excitation (stage 2), charge separation and transfer (stages 3, 4and 5), surface electrocatalytic interactions (stages 6 and 7)

$$e^- CB + h^+ VB \longrightarrow \text{energy} \quad (1)$$

$$H_2O + h^+ VB \longrightarrow .OH + H^+ \quad (2)$$

$$O_2 + e^- CB \longrightarrow O_2^{\cdot -} \quad (3)$$

$$.OH + \text{pollutant} \longrightarrow H_2O + CO_2 \quad (4)$$

$$O_2^{\cdot -} + H^+ \longrightarrow .OOH \quad (5)$$

$$.OOH + .OOH \longrightarrow H_2O_2 + O_2 \quad (6)$$

$$O_2^{\cdot -} + \text{pollutant} \longrightarrow CO_2 + H_2O \quad (7)$$

The first two stages occur upon the irradiation of light with an energy equal to or greater than the band gap energy (E_g) of the semiconductor resulting to an excitation of an electron from the valence band(VB) to the conduction band (CB) and subsequent generation of a positive hole in the VB. The band gap energy is an energy barrier between the VB (highest energy band occupied with electrons) and the conduction band (lowest energy band empty of electrons) in a semiconductor (Belver *et al*., 2019). However, an unfavorable charge recombination can occur in the bulk (stage 4) and on the surface of the semiconductor (stage 5) which is detrimental to the charge separation and transfer (stage 3) to the surface or interface active sites of the semiconductor. These active sites are regarded as the decisive factor for determining the photocatalytic quantum efficiency of a semiconductor metal oxide (Belver *et al*., 2019). Furthermore, only those energetic electrons and holes that migrate to

the surface of the semiconductor without recombination can be trapped by the active site or co-catalysts. This further stimulated the electro-catalytic reduction (stage 6) and oxidation (stage 7) reactions of the reactants adsorbed on the surface of the semiconductor respectively. Furthermore, the size of the band gap of a photocatalyst determines its color and optical properties in the visible region of the electromagnetic spectrum (Mamba and Mishra, 2016). Some common semiconductors and their band gap are shown in Table 2.1.

Table 2.1: Semiconductor photocatalyst and their corresponding Band Gap energy

Semiconductor	Band gap (eV)
Fe_2O_3	2.3
CdS	2.5
WO_3	2.8
TiO_2(rutile)	3.0
TiO_2(anatase)	3.2
ZnO	3.2
SnO_2	3.5
CdSe	1.7
g-C_3N_4	2.7
Cu_2O	2.2
ZnS	3.6
SiC	3.0

(Mamba and Mishra, 2016)

2.3 Tungsten oxide (WO_3) Nanowires

Tungsten oxide (WO_3) also known as tungsten trioxide is an important n-type semiconductor with a band gap of 2.8eV and has attracted much interest among material scientist due to its excellent physical and chemical properties (Arvisdea *et al*.,2021). WO_3 as an excellent transition metal oxide is naturally abundant, cost effective, less toxic towards living organisms and environmentally friendly (Madare and Hassel, 2019). Due to its unique properties, it has been employed in diverse applications such as gas sensing, fuel cells, water splitting, solar cells, batteries and optical devices (Arvisdea *et al*., 2021). Its intense absorption within the solar spectrum and high thermal and physiochemical stability makes WO_3 a good candidate for a visible photocatalyst for the degradation of pollutant in wastewater under ultraviolet or visible irradiation compared to other metal oxides such as ZnO, CdS, SiO_2 (Han *et al*., 2016). The photocatalytic property of WO_3 depends on its morphology, structure, composition, crystal phase (Guo *et al*., 2016).

Tungsten trioxide shows structural polymorphism and phase transitions at different temperature during heating or cooling. The most common phase found at room temperature is monoclinic I (γ-WO_3) formed at a temperature from 17-330 ^oC (see Figure 2.3). However, below this temperature, two other crystallographic phases exist; monoclinic II (e-WO_3) at a temperature below 43 ^oC and triclinic (δ-WO_3) at a temperature ranging between -43^oC to 17 ^oC. When the temperature is heated above 330 ^oC, transformation of monoclinic phase (γ-WO_3) to orthorhombic β-WO_3 usually occurs and the material remains stable up to 740 ^oC and at a temperature greater than 740 ^oC, tetragonal α-WO_3 is formed. Cubic c-WO_3 is also available as another phase of WO_3 (Figure 2.2). It is found in powders when impurity atoms

like H, Li or Na are present or in thin films where it can be developed alongside the monoclinic phase (Madare and Hassel, 2019).

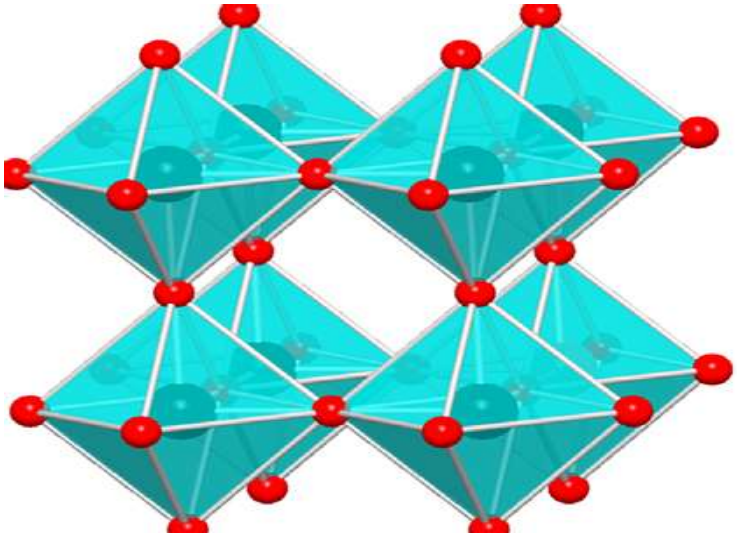

Figure 2.2: The cubic phase of c-WO_3 where the red small spheres represent the oxygen atoms and the black large spheres inside the polyhedral represent the tungsten atoms (Madare and Hassel, 2019)

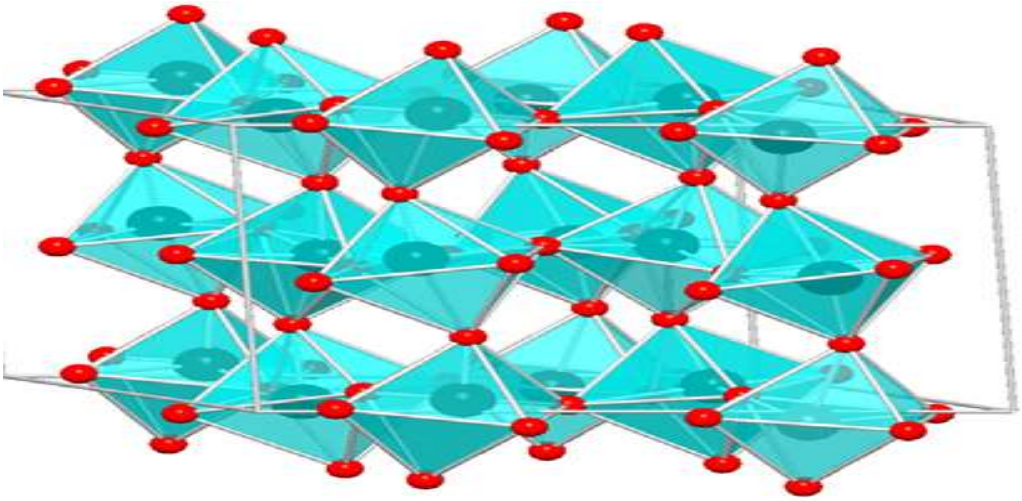

Figure 2.3: The monoclinic phase of γ-WO_3 where the red small spheres represent the oxygen atoms and the black large spheres inside the polyhedral represent the tungsten atoms (Madare and Hassel, 2019)

2.3.1. Shortcomings of WO_3 nanowires

Just like other semiconductors, WO_3 photocatalytic activity has limitations such as low conduction band edge potential which makes it difficult to minimize oxygen all through its presence in aqueous solution. This usually causes the occurrence of recombination and thus photocatalyst thus responsible for its low photocatalytic efficiency (Razali *et al*., 2021). More so, Kumar and Rao (2015) had asserted that WO_3nanowires are often confronted with the generation of blue shifts at the absorption edge which prevents the absorption of photons of light, thus mitigating some charge carries to participate in the redox reaction. Hence there is need to improve the catalytic activity of WO_3 nanowire through the incorporation of different metallic and non-metallic impurities onto its lattice layers.

2.3.2 Doping of WO_3 nanowires with metals and doping of WO_3 nanowires with non-metals

The photocatalytic behavior of semiconductor metal oxides can be improved through the introduction of heteroatoms into their crystal lattice points (Kahng *et al*., 2019). This phenomenon is known as doping which can be defined as the addition of impurities into semiconductor in order to modify its band structures (Belver *et al*., 2019). Dopants tends to accelerate the charge carrier's separations and transfer, creates more active sites which will improve effective redox reactions on the surface of WO_3 nanowires. In addition, the doping of WO_3 nanowires also improve its optical properties through band gap reduction or shift in absorption band edges (Madare and Hassel, 2019). In the case of metal doping, there is usually a direct contact between the metal and the semiconductor metal oxide which lead to the formation of an electric field based on electron transfer between the two substrates

according to Fermi level difference. The interaction usually results to the shifting of energy band edge and reduction of electron – hole recombination rate (Kahng *et al*., 2019). Researchers have employed different metals to alter the optical properties of WO_3 nanowires, some of which are reviewed as follows.

Zappa (2019) prepared an integrated Nb-doped WO_3 nanowires in conductometric device via a low-cost thermal oxidation method for a high performing hydrogen gas sensor. It was observed that the nanowires were made up of a few tens of diameters and a high surface roughness. The Nb dopant promoted the growth of the nanowires without any effect on the size of the nanostructure.

Zhang *et al*. (2020) utilized solvothermal method to synthesize copper doped $W_{18}O_{49}$ nanowires for photocatalytic reduction of CO_2. The result showed that doping with copper could affect the morphology and that the doped $W_{18}O_{49}$ had improved photocatalytic capability of reducing CO_2 than pure $W_{18}O_{49}$. Also, the doped $W_{18}O_{49}$ exhibited poor hydrophilicity in comparison with pure $W_{18}O_{49}$ nanowires and this could reduce the active sites occupied by H_2O molecules and hence significant for CO_2photocatalytic reduction. More so, Cu^+ dopant did not only change the conduction edge of the $W_{18}O_{49}$ nanowires, it also hampered its electron-hole recombination rate. Thummavichai *et al*. (2021) synthesized Na-doped WO_x bronze nanowires via solvothermal method. The Na dopants were observed to have changed the band gap energy value of WO_3 and displayed a high removal efficiency of over 90 % of photocatalytic activity over methylene blue under three conditions (dark, visible and UV light).

Chen *et al*. (2022) reported the successful synthesis of Mn doped and K doped WO_3 nanowires with a very good morphology, aspect ratio and high density prepared by chemical vapor deposition. It was observed that the doped WO_3 changed the WO_3 from monoclinic phase to hexagonal phase due to the presence of the dopants supplying charge traps and acting as scattering centers for carriers which in turn makes the life cycle of the electron –hole pair to be longer.

In non – metal doping, the dopants adjust the electronic structure of WO_3. It also propels the formation of new energy levels above and within the valence band of the semiconductor metal oxide and causes significant narrowing of the band gap energy, increasing the photo response in visible light and the photocatalytic efficiency (Govindaraj *et al*., 2020). In addition, non - metals dopants increase the conductivity of WO_3 which is related to the quashing of the photogenerated e^-/h^+ pair recombination on the photocatalyst efficiently (Han *et al*., 2016). Overtime non -metals like S, N, C and F have been used as dopants for WO_3 photocatalytic performance. This is carried out by the mixing of the p states of the dopants with the O 2p states, which enhances a reduction in the band gap. The dopants in the crystal structure act as electron traps averting the recombination with photogenerated hole. For instance, Han *et al*., (2016) investigated the photocatalytic activity of S-WO_3 nanowires. The effect of the dopant concentration on the properties of the S-WO_3 was investigated and the photo degradation of methyl orange under visible light compared to the undoped WO_3 nanowires. The result showed that 3% S-WO_3 exhibited the highest photocatalytic activity over photo degradation of methyl orange (MO).

2.4 Methods of Synthesizing WO_3 Nanowires

Two main approaches are involved in the synthesis of nanowires and other nanomaterials in general. There is the top down and bottom-up approach. As the name implies, the top-down approach simply involves the reduction of bulk material into nanoscale size. In other words, cutting, milling, shaping of materials into the preferred shape and size takes place. The size reduction is carried out by various processes such as mechanical milling/ball milling, chemical etching, thermal ablation/laser ablation, explosion process and sputtering. The bottom approach involves synthesis by chemical reaction amongst ions, atoms or molecules using salts as precursor. These salts are being mixed to form a homogenous solution (Pal Singh *et al*., 2020). Some methods under this approach include chemical precipitation, vapor deposition sol-gel process, aerosol process, spray pyrolysis, green synthesis, microwave synthesis and hydrothermal methods. Whilst the top-down approach offers more complexity, requires more sophisticated equipment for handling, less environmentally friendly, the bottom-up approach has none of the aforementioned especially the hydrothermal method of synthesis.

2.4.1 Hydrothermal method

Hydrothermal method is a simple, versatile and most widely used in the synthesis of inorganic materials from aqueous solutions under low temperature and low-pressure conditions (Tehrani *et al.,* 2020). The parameters that are usually adjusted during the synthesis include temperature, pressure, time, pH and the concentration of the precursor while water is the most commonly used solvent during the synthesis process (Nagyne-kovacs *et al*., 2019; Wu *et al*., 2019). In this method, the solubility of the solid which is usually the precursor increases because of the temperature and pressure generated above the critical point

of the solvent used. This method offers some advantages which include one step synthetic procedure, environmental–benign because non-toxic solvents are used during synthesis and no residual waste is produced alongside the final products, cost effective, good dispersion in solution. In other words, due to the intense conditions in the autoclave, nearly all materials can be made soluble (Wu *et al*., 2019). More so, the hydrothermal method offers the formation of well-crystallized nanostructures (Nagyne-kovacs *et al*., 2019).

Several researchers have employed the hydrothermal method to prepare well organized arrays of WO_3nanowires and other semiconductor nanowires and are reviewed as follows; Wanjun *et al*. (2016) reported the hydrothermal synthesis of WO_3 nanowires in the presence of Guanidine sulfate and evaluated its photocatalytic activity on the degradation of methylene blue (MB) in aqueous solution. It was also observed that the concentration and composition of the inorganic salt determined the shape of the nanostructures. Also, during the process of synthesis, the addition of different dispersants enhanced the photocatalytic performance of the WO_3 nanowires with 72% degradation rate of methylene blue.

Han *et al*. (2016) prepared S-doped WO_3 nanowires (S-WO_3) nanowires using hydrothermal method by low-temperature solid–state annealing treatment. It was characterised using SEM, EDX, XPS, and XRD, Raman spectroscopy, DRS and UV-vis and photocurrent responses. The SEM images showed the formation of thin wires with an average length of 2.1µm. However, doping with sulphur did not change the morphology of the nanowires but rather influenced the light harvesting capacity of WO_3 nanowires by 3%.

Lu *et al*. (2018) reported the preparation of ultrathin hexagonal WO_3 nanowires (U-WO_x NW) by modified hydrothermal method and were characterised using TEM, IR, XRD and

XPS. Also, the photocatalytic performance of the nanowires was also studied. The XRD result showed the formation of hexagonal phase of WO_3, though the crystallite size was not calculated. The obtained U-WOx NW showed impressive absorption tail in the visible region and near the infrared region causing oxygen vacancies which was beneficial for photocatalysis. It also showed over 90 % degradation of methyl orange at 80 minutes' irradiation time.

Hu *et al*. (2018) reported the synthesis and characterisation of WO_3/Graphene Nanocomposite for enhanced photocatalytic activities via the one step In-situ hydrothermal reaction using sodium tungstate and graphene oxide as precursor. The synthesized WO_3/GR nanocomposite was confirmed by TEM, SEM, EDS, Raman spectroscopy and XPS. The composite enhanced visible light activity required for photocatalysis. They also reported that the presence of the graphene in the composite promoted the electron transfer and optical property of the composite. XRD result confirmed the formation of hexagonal phase of WO_3 on the graphene however the crystallite size of the nanocomposite was not calculated. The WO_3/GR composite showed improved photocatalytic efficiency of 83% in visible light which was double that of pure WO_3 with 43% efficiency.

Nagyne-kovacs *et al*. (2019) reported the effect of pH in the hydrothermal preparation of monoclinic tungsten oxide. Also, the importance of various additives such as ethanoic acid (CH_3COOH), sodium perchlorate ($NaClO_4$) and sodium sulphate (Na_2SO_4) on the crystal structure and morphology was investigated. From the results obtained it was found that the samples had similar nanosheets-like morphology when CH_3COOH, $NaClO_4$ were used as additives and even when none was used at a temperature of 180^oC and 200^oC. However,

when Na_2SO_4 was used elongated like sheets were obtained at a temperature of 180^oC, which can be attributed to the structure directing role of Na_2SO_4. In the case of effect of pH, the samples prepared at pH of 0.1 and at a temperature of 180^oC and 200^oC were all pure monoclinic phase of WO_3.

Pauekphong *et al*. (2019) also reported the synthesis of WO_3/TiO_2 nanowires by hydrothermal method.WO_3/TiO_2 nanowires were synthesized successfully by hydrothermal method. The effect of doping dosage on crystal structure, morphology, band gap energy and the defect concentration of the synthesized sample were also studied and further characterised. Only the monoclinic phase was formed at calcination temperature of 400^oC for 2 hours. Although the doping of the TiO_2 with WO_3 did affect the lattice parameter, band gap energy, crystallite size and the effect concentration of the already doped sample, but doping with 5 mol of WO_3 into TiO_2 nanowire gave the best result for application as electrochemical sensors and ionic batteries.

Shen *et al*. (2019) synthesized Co doped WO_3 nanowires with modified and improved electrochromic properties by seed free hydrothermal method. The effect of Co dopants on the structure and electrochromic performance on the WO_3 nanowires was also explored. It was observed that doped WO_3 nanowires showed notable modification in surface morphology with vertically aligned nanostructure compared with the pure WO_3 nanowire film. Also, the doped WO_3 nanowire films had better electrochromic properties with maximum transmittance modulation of 76.7% at a wavelength of 890 nm and over 4000 cycle stability. The above observation could be ascribed to the vertically aligned nanostructure of

the films which made available a large surface area, an accessible intercalation sites and a rapid ions diffusion pattern.

Tehrani *et al.* (2020) reported the hydrothermal synthesis and characterisation of WO_3 nanostructures. 1D and 2D WO_3 nanostructures by hydrothermal method and the effect of reaction time were also studied to explore the structural, morphological and optical properties. Analytical techniques such as XRD, FESEM, FTIR and DRS were used to analyze the prepared samples and the results showed that the morphological changes of the nanostructures depend strongly on the duration of time used and the concentration of capping agents.

Silveira *et al*. (2020) reported the synthesis of Mo-doped WO_3 nanowires for the adsorption of methylene blue dye from wastewater. The effect of Mo-WO_3 nanowires as an adsorbent was studied. The report indicates that on the addition of molybdenum, the morphology of the As-synthesized WO_3 nanowires changes from large bundles to narrow bundles with an increasing number of isolated thin nanowires. Also, by increasing the percentage of Mo, the As-synthesized nanowires bundles exhibited faster and improved removal of methylene blue from wastewater and doping with molybdenum also changed the porosity, surface area and crystalline structure of the undoped WO_3.

2.5 Characterisation Methods

Characterisation of nanowires are based on assay of its physicochemical properties such as surface areas, morphologies, crystallinity, microstructures, elemental composition, thermal stability, chemical surface oxidation states and particle size among others. Hence, characterisation techniques that can be used to assess the formation of nanowires include

Ultraviolet(UV)-visible spectroscopy, High Resolution Transmission Electron Microscopy (HRTEM), High Resolution Scanning Electron Microscopy (HRSEM), X-ray diffraction (XRD), Energy dispersive spectroscopy, (EDS), Brannuer Emmett Teller (BET) N_2-adsorption-desorption process among others and are explained as follows:

2.5.1 UV-visible Spectroscopy

UV-visible spectroscopy is a non-destructive analytical technique that uses near ultraviolet and visible light for analysis. The spectrum is usually used to study the composition and the structure of a sample material. The analyte in the material can absorb light from 200-400 nm range, which is the ultraviolet (UV) region, or in 400-800 nm region which corresponds to the visible region. This spectroscopy works on the principle of Beer-Lambert law which states that the absorbance of light by a sample is directly proportional to the concentration of absorbing species present in the sample and the path length of the sample. In other words, a molecule in a given sample material can absorb light in the UV-Visible region depending on the absorbing group present in the molecule. Hence, different molecule in a material absorbs light at different wavelength in the spectrum. A spectrophotometer is used in UV-visible spectroscopy. The major components of the spectrophotometer are source of light, monochromator, cuvette, detector and the display (Readout device). Other applications of UV-visible spectroscopy include detection of impurities, manufacture of drugs, study of kinetics of reaction, to determine the presence or absence of functional groups in a compound, quantify the amount of protein and DNA in a sample, quantify the number of bacterial cells in a cell structure.

2.5.2 High Resolution Scanning Electron Microscopy (HRSEM)

HRSEM is an imaging technique that utilizes a beam of electrons to form high magnification images and provide information on the morphological arrangement of the particles in a material. Tungsten and Lanthanum hexaboride filaments are mostly used as electron source with the cathode heated to produce electrons having energy of a few hundred to 40 keV. These electron sources (W and LB_6) have high melting points and relatively low work functions (Havancsak, 2017). The electron beam produced is accelerated by the applied voltage towards an anode, passes the anode via a magnetic lens system through an aperture into the vacuum chamber to the surface of the specimen. Image formation is dependent on the produced signals from the electron beam and electron interaction with the specimen. During HRSEM analysis, the sample is mounted on a sample holder and coated with a conductive metal such as gold, gold/palladium, alloy, platinum, osmium, iridium, tungsten, chromium or graphite using sputter coater (Patra and Back, 2014). The purpose of coating is to prevent charging which cause distortion during imaging. The size distribution and shape of nanomaterials can be directly acquired from HRSEM.

2.5.3 High Resolution Transmission Electron Microscopy (HRTEM)

HRTEM is commonly used for determination of the shape, size and microstructure of nanomaterials (nanoparticles, nanowires, nanofibers, nanotubes etc.) However, sample preparation for HRTEM is quite complex and takes a lot of time due to the fact that the samples must be ultrathin for electron transmittance measurement. Hence, before characterisation, thin films containing the samples are prepared on carbon-coated nickel or copper grids by dropping a very small amount of the sample in ethanol /methanol solution

onto the grid and then removing the extra solution with blotting paper. The grid containing the sample is exposed to photo light for complete evaporation of ethanol or methanol. This technique remains the most frequently used for the characterisation of nanomaterials at a spatial resolution down to the level of atomic dimension of at least <1nm. The principle basically involves transmission and the interaction between incident electron beam and the tiny foil specimen to produce the desired information about the specimen. The samples are exposed to a monochromatic beam of electrons for easy penetration and are projected into viewing screen to generate an image (Patra and Back, 2014).

2.5.4. Energy Dispersive Spectroscopy (EDS)

Energy-dispersive spectroscopy (EDS) is usually coupled with HRTEM or HRSEM for the determination of elemental compositions of a sample based on the interaction of some source of X-ray excitation with the sample. The ground state electrons in electron shells bound of the sample in the nucleus get excited upon interaction by the incident beam which then leads to ejection of electrons from the shell thus creating an electron hole. The number and energy of the X-rays emitted from a specimen can be measured using energy-dispersive spectrometer. The X-rays have characteristic difference in energy between the two shells, and also the atomic structure of the element from which they were emitted. The energy of the emitted X-ray is a characteristic feature of the element and the element is therefore analyzed qualitatively and quantitatively (Lin *et al.*, 2013*).*

2.5.5. Selected Area Electron Diffraction (SAED)

Selected Area Electron Diffraction (SAED) is a technique that is coupled with Transmission Electron Microscope (TEM) to gauge the crystallinity, crystal structure, orientation and

lattice parameters of a sample. This is carried out by assessing the electron diffraction pattern produced by the interaction of the electron beam with the sample's atoms. SAED can also be used to draw out information concerning the local texture in materials. (Sivakumar and Dasgupta, 2019). The objective lens of the machine takes electrons emanating from the specimen and produces a magnified image where all electrons created from a single point of the specimen are focused onto a particular spot irrespective of the angle at which they emanated from (Tivol, 2020).

2.5.6. X-Ray Diffraction

XRD is an analytical technique which produces diffraction patterns through the bombardment of a sample with X-rays to give a mineral phase and crystal structure of the sample. X-rays are produced when a fast-moving electron is slowed down rapidly in the wavelength range of 0.06 - 125 Å in the electromagnetic radiation spectrum. Hence, X-rays are good probes for determining atomic arrangements of crystallographic materials due to their short wavelength (Suwarnkar *et al*., 2014). X-rays that are diffracted during analysis provide information on the crystalline nature of the sample which may be single crystalline, polycrystalline, microcrystalline or amorphous. Diffraction occurs when a structure has a repeat distance similar to the incident wavelength when waves interfere with it. The interference can either be constructive or destructive depending on the scattering of the incoming wave fronts by the structure. This technique uses Bragg's law (eqn 2.1) to determine atomic spacing in the crystal:

$$n\lambda = 2dsin\,\Theta \tag{2.1}$$

where n is an integer, λ is wavelength of the X-ray, θ is the incident angle, and d is the spacing of the reflecting atomic planes.The particle size can be determined using the Scherer's equation (eqn 2.2)

$$D = \frac{k\lambda}{\beta cos\,\theta} \quad (2.2)$$

Where D is the crystallite size, k = constant 0.94, λ = wavelength of X-ray (1.54), β = Full width at half maximum (FWHM) in radians, θ = the incident angle.

2.5.7. Brunauer Emmett and Teller (BET)

BET involves the measurement of the specific surface area, pore size and volume distribution of a nanomaterial. BET analysis provide information on the specific surface area of materials using nitrogen multilayer adsorption-desorption as a function of relative pressure on an automated analyzer. The technique also gives information on the specific surface area in (m^2/g) which aids in predicting the porosity of the synthesized nanomaterials whether it is microporous, macro porous or mesoporous.Nitrogen gas is usually used during BET because of its availability in high purity and its strong interaction with most solids. Because the interaction between gaseous and solid phases is usually weak, the surface is cooled using liquid N_2 to obtain detectable amounts of adsorption. Known amounts of nitrogen gas are then released stepwise into the sample cell (Toston *et al.*, 2017).

2.6 Indigenous dyeing wastewater

The swift increase in population has brought about an increase in demand and supply of goods and services hence there is need for industrialization. Water is a principal component needed in the ecosystem as all living things and non-living things like plants depends on

water for their survival. However, good quality water is affected by some factors such as population growth, industrialization, urbanization and geological factors (Mohammed *et al*., 2020). Pollution of water bodies by industries has become a major challenge in developing countries like Nigeria. The dyeing industry is one industry that makes use on water than any other industry globally, and an average dyeing industry consumes 200 liters per kg of a fabric on a daily basis (Navin *et al*., 2018). The wastewater from this industry often contains colors, dyes, surfactants, high COD and BOD concentration, salts, many aerosols, acidic and alkaline contaminants, heavy metals, high pH, high turbidity, suspended solids (Durotoye *et al*., 2018; Kyrii *et al*., 2020; Navin *et al*., 2018)

2.6.1 Health and environmental impact of indigenous dyeing wastewater

The presence of these contaminants in wastewater can cause adverse effect on the balance of ecosystem when the water is being discharged. Dyes present in wastewater can distort photosynthetic process in plants, affect aquatic life due to low oxygen consumption and low light penetration hence causes choking of fish gills which leads to death of the fishes, decreases algae's capacity of making food and oxygen (Navin *et al*., 2018; Kyrii *et al*., 2020). Some of its effects on human health include skin irritations, constrained sperm motility, allergic reactions, respiratory troubles and cancer (Durotoye *et al*., 2018). The dyes can also increase chemical oxygen demand (COD), promote toxicity and mutagenicity and disrupt food chain (Lellis *et al*., 2019).

2.6.2 Reactive dyes

Reactive dyes are dyes that form a covalent bond with the substrate (fiber) to which it was attached to. They have a general structure of R-B-X where R = chromophore group

(Phthalocyanine, Anthaquinone, etc.), B= bridging group (oxide, ethyl or methyl group etc.), X = Reactive group such as –Cl. –Br, -SH etc. Reactive dyes are classified into:

a. Classification based on the chemical composition. Examples include vinyl sulphone dyes, chlorotriazene dyes and heterocyclic halogen.
b. Classification based on application methods of temperature. They include cold brand dyes applied at low temperatures, hot brand dyes applied at medium temperature of 60°C and high exhaust brand reactive dyes applied at 80-92°C.

Properties of reactive dyes include:

i. They are water soluble
ii. Anionic in nature
iii. Forms strong covalent bond with cellulosic fiber in alkaline medium
iv. Cost effective

2.6.3 Heavy metals in dyeing wastewater

Heavy metals are inorganic elements with high atomic weight and density higher than 5 g/cm^3 (Yalcin *et al*., 2020). They are toxic at part per billion level. They include As, Hg, Cd, Cr, Pd, Pb. These metals are being discharged into the environment by anthropogenic activities like automobiles exhaust, mining activities, and industrial activities. Heavy metals are also known to be non-biodegradable unlike organic pollutants. Heavy metals find their way into dyeing wastewater during dyeing process, through protective agents used during storage. Some colour pigments are produced using heavy metals such as Pb, Cd, Cr, and Zn (Turksoy *et al*., 2021).Exposure to such metals has effect on human health and agricultural products. For example, long term exposure to Cd may lead to premature death and cause cancer, Pb

exposure can affect the nervous, skeletal and immune system and may cause metal issues in children. It can also cause the damage of chlorophyll by fastening growth retardation (Turksoy *et al*., 2021) and Ni exposure can lead to kidney diseases, cardiovascular disease and epigenetic changes. (Genchi *et al*., 2020).

2.7 Chapter Summary and Research gaps

In this chapter, photocatalytic technology as a potential approach to wastewater remediation was reviewed. The mechanism of photocatalysis which simply involves the harvesting of light by semiconductor metal oxide followed by the excitation of electrons from the lower energy level (valence band) to the high energy level (conduction band) leading to the formation of electron/hole pair that participate in reduction/oxidation reaction and hence degradation of the contaminants present in the wastewater. This chapter also presents information on tungsten trioxide (WO_3) as good candidate for photodegradation of pollutant in wastewater under ultraviolet or visible irradiation compared to other metal oxides such as ZnO, CdS, SiO_2. However, its limitation includes low band energy and high recombination rate which is not good for a good photocatalytic performance, hence the need for doping which involves the introduction of impurities into the crystal lattice of WO_3 were also detailed in this chapter.

Furthermore, the doping of WO_3 nanowires with metals and non – metals which also improve its optical properties through band gap reduction or shift in adsorption band edges were also reviewed. Different methods that have been employed for the synthesis of WO_3 nanowires were listed however the hydrothermal method offer some advantages which includes one step synthetic procedure, environmental–benign, cost effectiveness, good dispersion in solution,

in other words due to the intense conditions in the autoclave, nearly all materials can be made soluble. It also offers the formation of well-crystallized nanostructures.

Overall, the chapter also provides an overview of indigenous dyeing wastewater and the contaminants present particularly dyes and their associated environmental effects. It was found that the treatment of such wastewater using conventional methods did not degrade the toxic dyes instead photocatalytic technology has been found suitable to achieve complete mineralization of organic dyes in wastewater. Previously, doping of WO_3 nanowires with metal and non-metal elements such as potassium and fluorine element respectively has been reported to improve its photocatalytic performance. However, doping of WO_3 nanowires with calcium and chlorine has not been reported yet. This study intends to prepare the nanocomposite of WO_3, Ca and Cl and evaluation of its performance on reactive dyes in dyeing wastewater.

CHAPTER THREE

MATERIALS AND METHODS

3.1. Materials

Table 3.1 and 3.2 represent the list of chemicals/reagents and characterisation tools used in this study. The chemicals/reagents obtained from Sigma Aldrich were analytical grade and used without further purification.

Table 3.1: Lists of chemicals/reagents

S/No	Reagents	Purity (%)	Supplier
1	Sodium tungsten oxide dihydrate ($Na_2WO_4.2H_2O$)	99	Sigma-Aldrich
2	Oxalic acid ($H_2C_2O_4$)	99	Sigma-Aldrich
3	Hydrochloric acid (HCl)	99.9	Sigma-Aldrich
4	Calcium nitrate ($Ca(NO_3)_2$)	99.9	Sigma-Aldrich
5	Sodium chloride (NaCl)	98.6	Sigma-Aldrich
6	Nitric acid (HNO_3)	99.9	Sigma-Aldrich
7	Magnesium sulphate ($MgSO_4$)	99.5	Sigma-Aldrich
8	Calcium chloride ($CaCl_2$)	97	Sigma-Aldrich
9	Ferric chloride ($FeCl_3$)	98	Sigma-Aldrich
10	Tetraoxosulphate(VI) acid (H_2SO_4)	98	Sigma-Aldrich
11	Sodium thiosulphate ($Na_2S_2O_3$)	98.6	Sigma-Aldrich
12	Mercuric sulfate ($HgSO_4$)	99.9	Sigma-Aldrich
13	Potassium dichromate ($K_2Cr_2O_7$)	99.8	Sigma-Aldrich
14	Ferrous ammonium sulphate (FAS)	99.7	Sigma-Aldrich

Table 3.2: List of Analytical Equipment

S/No	Analytical Technique	Model
1	HRSEM/EDS	Zeiss Auriga
2	HRTEM/SAED	Zeiss Auriga
3	XRD	Bruker D8 Cu-Kα radiation Themba
4	BET	NOVA 2400e
5	UV-Visible spectrophotometer	SHIMADZU UV-1800

3.1.1 Sampling and sample pre-treatment

The wastewater used in this study was collected from an indigenous dyeing industry in Minna, Niger State, Nigeria, and stored in a clean polyethylene (PET) bottle. Before collection of the sample, the bottles were washed with 10 % Nitric acid and thoroughly rinsed with de-ionized water. The sample was then transported to the laboratory and kept in the refrigerator at 4 ^{o}C before use (Nkansah *et al*., 2016).

3.2 Hydrothermal Synthesis of Nanowires

3.2.1 Hydrothermal synthesis of WO_3

WO_3 nanowires were prepared via hydrothermal method using sodium tungsten dihydrate ($Na_2WO_4.2H_2O$), oxalic acid ($C_2H_2O_4$), and sodium chloride (NaCl) as precursors, stabilizer and structural directing agent respectively. Firstly, a known amount of $Na_2WO_4.2H_2O$ according to the concentration required in the table below and 0.05 g of NaCl was dissolved in 50 cm^3 of distilled water and stirred for 30 minutes continuously on a magnetic stirrer at 500 rpm. The pH value of the solution was adjusted to 2 using 3 mol/dm^3 HCl acid solutions.

Afterwards, 6.3g of $(COOH)_{2.2H2O}$ was added and further stirred for another 1h. After stirring, the suspension was transferred to a 50 cm^3 capacity Teflon-lined stainless-steel autoclave and heated to 200 ^oC for 1 h 30 mins in an oven and later allowed to cool to room temperature. The product was washed thoroughly with distilled water and dried at 70 ^oC overnight (Han *et al*., 2016). The experimental design employed in the synthesis of WO_3 nanowires is presented in Table 3.3.

Table 3.3. Box-Behnken design employed in the synthesis of WO_3 nanowires

Run	Concentration of Tungsten salt (mol/dm^3)	Temperature (^oC)	Reaction Time (min)	Response Yield (%)
1	0.55	140	90	76
2	1	80	90	76
3	1	200	90	98
4	1	140	150	90
5	0.55	80	30	60

3.2.2. One-Pot Hydrothermal synthesis of chlorine-calcium co-doped WO_3 nanowires

The procedure employed for the preparation of WO_3 nanowires was repeated for the synthesis of the chlorine-calcium co-doped nanocomposite in 100 cm^3 beaker capacity except that two different dopants (NaCl and $Ca(NO_3)_2$) were used in the following mixing ratios (1:1, 1:2, 1:4, 2:1, 4:1) and then mixed with 20 cm^3 of 0.55 mol/dm^3 $Na_2WO_4.2H_2O$ in distilled water. For the one-pot synthesis, the tungsten salt precursor and the two dopants were mixed together in the same beaker and later transferred to a 50 cm^3 Teflon-lined stainless steel

autoclave capacity and maintained for 2 h 30 mins at a temperature of 200 °C to yield the Cl-Ca-co-doped nanocomposite denoted as 1c-1a,1c-2a,1c-4a,2c-1a,4c-1a (Han *et al*., 2016).

3.2.3 Characterisation of synthesized WO_3 and Cl-Ca/ Co- doped WO_3 nanowires

The prepared WO_3 nanowires and Cl-Ca co-doped WO_3 nanowires were characterised using the following analytical instruments; UV-Visible/spectroscopy, HRSEM/EDS, HRTEM/SAED, XRD, and BET.

3.2.3.1 *Identification of mineralogical phase*

The identification of mineralogical phases was done using X-ray diffractometer (XRD)-D8 Bruker AXS advance, fitted with Lynx eye detector containing Cu-Kα radiation. The measurement was done as follows: 2 g of WO_3 nanowires/composite was placed in a flat rectangular plate. The scanning was done at 2θ value of 10°-80° at a scanning rate of 0.5°/second. The crystalline particle size was then calculated using Debye Scherer equation (see equation 2.2)

3.2.3.2 *Morphological arrangement and elemental composition analysis*

The morphology of the prepared samples was obtained using Zeiss Auriga High Resolution Scanning Electron Microscope (HRSEM) fitted with secondary electron detector and the Energy Dispersive X-ray spectroscopy (EDS). The sample (0.05 mg) was first mounted on a metal sample holder called a stub using a double-sided tape. The sample was then sputtered coated with gold and palladium (ratio 4: 1) to prevent charging which distort imaging during analysis using a coating machine and thereafter it was ready for HRSEM/EDS observation at a voltage range of 10-15 kV. The EDS was done by adjusting the measurement angle to $150^{o}$and applied voltage to 20 kV.

3.2.3.3 *Microstructure and crystalline analysis*

High Resolution Transmission Electron Microscopy images model Zeiss Auriga operated at acceleration voltage of 20 kV was used to examine the microstructure and particle size. Ethanolic solution (0.05 g in 10 cm^3) was used followed by ultrasonization for 30 minutes. Thereafter, the mixture (10 uL) was then measured into a whole carbon grid and exposed to photo light for 3 minutes before analysis. The sample with the grids was then mounted on a single tilt holder.

3.2.3.4 *Absorption Band determination by UV-Visible spectroscopy*

UV-Visible Spectroscopy in this case, the **S**himadzu UV 1800 was used to determine the wavelength of absorption. The synthesized nanowire (1 cm^3) dissolved in distilled water was put in a cuvette and then scanned in the range of 200-800 nm at scanning speed rate of 50nm/minute.

3.2.3.5 *Surface area evaluation by BET*

The specific surface area (internal and external), pore size distribution of the synthesized undoped and doped WO_3 nanowires were determined using NOVA 2400e by applying N_2 as an absorbate on a micrometer ASAP 2020 chemisorption surface area analyzer. Prior to measurement, the samples were degassed at 200 ^oC under nitrogen for 3 hours to remove moisture and other impurities.

3.2.4 Physico-chemical assessment of the wastewater

Physico-chemical analysis was carried out on the wastewater before and after the photocatalytic experiment using standard methods. The procedure of each parameter analyzed is described as follows:

3.2.4.1 *Determination of pH*

The pH of the wastewater was determined by potentiometric method using a pH meter probe. The electrode of the pH meter was washed with distilled water and wiped dry using a filter paper. The electrode was immersed into a buffer solution with a pH of 7 for calibration. Furthermore, the electrode was washed with distilled water and wiped dry and further dipped into a known buffer of pH 4 to adjust the reading to 4. Afterwards, the electrode was washed with distilled water and the procedures repeated using pH 7 and pH 4 until correct readings were obtained. Thereafter, the electrode was inserted into a 25 cm^3 of the dyeing wastewater and the reading displayed on the pH meter was taken appropriately (Saritha and Chockalingam, 2019).

3.2.4.2 *Determination of biological oxygen demand (BOD)*

About 2 liters of distilled water in a five-liter flask was aerated for at least 3.5 hours and 1 cm^3 each of phosphate buffer, magnesium sulphate solution, calcium chloride solution and ferric chloride solution was added to the distilled water and further aerated for another 30 minutes. A 300 cm^3 BOD bottle was filled with the wastewater sample and further filled with the aerated water and covered tightly with the lid of the bottle to avoid air bubbles. The bottle was then kept in a BOD incubator at 20 ^oC for 5 days. After 5 days, 2 cm^3 of $MnSO_4$, 2cm^3 of alkali azide solution and 2 cm^3 of conc. H_2SO_4 were added and the mixture was properly shaken for 10 minutes. At this point, a yellow color was obtained, then 200 cm^3 of the mixture was taken and a starch solution was added as an indicator to obtain a purple color. The mixture was titrated with 0.025N sodium thiosulphate until a color change from purple to colorless indicating the end point. In another BOD bottle filled with blank, aerated distilled

water without the wastewater sample was added (Saritha and Chockalingam, 2019). The BOD was calculated using equation 3.1:

BOD_5

$$= \frac{(\text{blank value} - \text{titrated value}) \text{x } 300}{volume\ of\ sample} \quad (3.1)$$

3.2.4.3 *Determination of chemical oxygen demand (COD)*

The culture tubes and caps were washed with 20 % H_2SO_4 to prevent contamination prior to use. 2.5 cm^3 of dyeing wastewater sample was measured into the culture tubes and digestion solution comprising 0.25N (1 cm^3) of K_2CrO_7, and a spatula of mercuric sulphate ($HgSO_4$) and 3.5 cm^3 of sulfuric acid known as COD acid was added to form an acid layer and the cap of the tubes were tightened strongly. The mixture was then inverted several times to obtain homogeneous solution. The tube was then placed in a block digester already pre heated at a temperature of 150 ^oC and refluxed for 2 hours behind a protective shield. Afterwards, the culture tubes caps were then removed and 1-2 drops of ferroin indicator was added and the solution stirred rapidly on a magnetic stirrer. The solution was titrated with standardized 0.10 mol/dm^3 ferrous ammonium sulphate (FAS). A sharp color change from blue-green to reddish brown which indicates the end point of the titration was observed. The same procedure was repeated for blank (Saritha and Chockalingam, 2019) and the COD value calculated using equation 3.2:

$$\text{COD(mg/l)} = \frac{(\text{blank value} - \text{titrated value}) \text{x molarity of FAS x } 8000}{volume\ of\ sample} \quad (3.2)$$

Where 8000 = mill equivalent weight of O_2 x 1000 cm^3

3.2.4.4 Determination *of total organic carbon* (TOC)

The TOC of the wastewater was determined using a Total Organic Carbon Analyzer TOC – Apollo 9000 manufactured by Tekmar Instruments. 50 cm^3 of the wastewater was acidified in order to bring the pH to 2-3, and then a purging gas was bubbled through the sample in order to eliminate the inorganic carbon in the sample by converting it to CO_2. The concentration of inorganic carbon (IC) was obtained using an infrared analyzer known as a non-dispersive infrared (NDIR) detector. The total carbon (TC) was determined by passing the sample into a combustion furnace which was then supplied with a purified air where it undergoes combustion through heating to a temperature up to 680 ^oC in the presence of platinum catalyst. It was then decomposed and converted to CO_2. The CO_2 generated was cooled and further dehumidified and then detected by NDIR. The concentration of the total carbon (TC) in the sample was determined through comparison with a calibration curve formula. The TOC concentration was then calculated using equation 3.3

$$TOC = TC - IC. \quad (3.3)$$

Where TC = total carbon, IC = inorganic carbon (Florescu *et al*., 2013)

3.2.4.5 *Identification of reactive dye in indigenous dyeing wastewater*

To detect the presence of reactive dyes in the wastewater sample, ultra violet (UV) analysis of the wastewater sample was carried out. UV spectrophotometer with model number SHIMADZU UV-1800 was used with 2 cm^3 sample placed in a standard quartz glass cuvette of 10mm optical path length and the absorbance scanning was done in the range of 200 – 800 nm.

3.2.4.6 *Determination of heavy metals in the indigenous dyeing wastewater*

Prior to digestion, 2 cm^3 and 5 cm^3 of concentrated HNO_3 and HCl to 100 $cm^3$of wastewater sample and mixed very well and further transferred to 100 cm^3 beaker. Another 2 cm^3 of concentrated HNO_3 and 5 cm^3 of concentrated HCl were further added. The sample was then covered with a watch glass and heated on a steam bath, hot plate at 90 to 95 ^oC until the volume was reduced and then allowed to cool. The sample was filtered in order to remove insoluble material that could clog the nebulizer. The filter paper and filtering apparatus were thoroughly washed and pre-rinsed with dilute HCl. The final volume was adjusted to 100 cm^3 with deionized water and analyzed using Atomic Absorption Spectrophotometer with model number MY17380004 (Dande *et al*., 2019).

3.2.5 Blank and control experiment

3.2.5.1 *Adsorption process*

Before the photocatalytic activity experiment, control (blank) experiment was carried out by exposing wastewater alone to sunlight irradiation. For adsorption experiment, 0.05 g of each prepared catalyst was added into 100 cm^3 of the dyeing wastewater in a 250 cm^3 beaker and stirred on a magnetic stirrer at 200 rpm for 1h in the dark to allow for sample homogeneity. Then 10 cm^3 of the solution was sampled periodically at regular interval of 20 minutes and immediately analyzed for reactive dye removal and COD. This was done to establish that the percentage degradation or removal of pollutants in the wastewater was due to adsorption only.

3.2.5.2 *Photocatalytic activity of the synthesized WO_3, Cl / Ca co-doped nanowires*

The photocatalytic activity of the synthesized samples (catalyst) was evaluated through degradation of reactive dye in dyeing wastewater under sunlight irradiation. Solar energy was

used as light source. For each experiment, a known amount (0.02g) of the undoped WO_3 and the doped WO_3 nanowires was added separately into 250 cm^3 beaker containing different 100 cm^3 of the wastewater and stirred at 200 rpm for 1h in the presence of sunlight irradiation with intensity of 252.92 w/m^2 at 36 ^oC. Thereafter, the mixture was agitated on a magnetic stirrer for 6h. 20 cm^3 of the solution was sampled simultaneously at regular interval of 1 h and immediately analyzed for reactive dye and COD. The pH and heavy metals such as Cd, Cr, Zn, Pb was also checked after the treatment. This was done to establish that percentage degradation of reactive dye in the dyeing wastewater was due to photocatalysis (Sunlight + photocatalyst) and removal of selected heavy metals due to adsorption.

3.2.6 Data analysis

The percentage COD removal inthe wastewater was calculated using equation 3.4 (Shewa *et al.,* 2016).

$$\text{COD removal (\%)} = \frac{(\text{COD})0-(\text{COD})t}{(\text{COD})0} \times 100 \quad (3.4)$$

Where (COD_0) the initial concentration of the COD in the wastewater

(COD_t) is the concentration of the COD in the wastewater at different time. The degradation or mineralization of the reactive dye is expressed in terms of removal efficiency was calculated using the equation 3.5 (Shewa *et al.,* 2016).

Photodegradation efficiency of reactive dye

$$= \frac{\text{Initial -final concentration of reactive dye}}{\text{initial concentration}} \text{ x } 100 \quad (3.5)$$

Where ($Initial_0$) is the initial concentration of the dye in the dyeing wastewater, ($final_t$) is the concentration of the reactive dye in the wastewater after photocatalytic treatment at different irradiation time.

The % heavy metal removal was calculated using equation 3.6

$$\%removal=\frac{Co-Ct}{Ct}\times 100 \quad (3.6)$$

Where C_o and C_t are the initial concentration and final concentration after photocatalysis in ppm respectively. The experimental data was treated with three kinetic models namely; Zero-order, First order, second order. The three kinetic models for this study listed are estimated using equations 3.7 to 3.9 and listed as follows:

3.2.6.1 ***Zero-order reaction kinetic****s*:

$$\frac{dc}{dt} = -k_0 \quad (3.7)$$

3.2.6.2 ***First-order reaction kinetics:***

$$\frac{dc}{dt} = -k_1 C \quad (3.8)$$

3.2.6.3 ***Second-order reaction kinetics:***

$$\frac{dc}{dt} = -k_2 C^2 \quad (3.9)$$

where C is the concentration of indicator parameters such as COD or TOC; k_0, k_1 and k_2 represent the apparent kinetic rate constants of zero-, first- and second-order reaction kinetics, respectively; t is the reaction time.

3.2.7 Regeneration and reusability studies

For the reusability study, 0.1 mol/dm^3 of NaOH solution was used as a desorption medium followed by addition of 10 mg nanoparticles to 100 cm^3 of 0.1 mol/dm^3 of NaOH. The mixtures were stirred continuously for 6 hours at ambient temperature and when each recycling experiment finished, the mixture was filtered and the residue (catalyst) was washed with deionized water for 30 mins and calcined at 550 ^{o}C for 2 h and then examined using XRD to check for the mineralogical phase (Amigun *et al*., 2022). Thereafter, the regenerated Cl-Ca-WO_3 nanowires, were reutilized for five cycles to determine the effectiveness of the nanowires.

CHAPTER FOUR

RESULTS AND DISCUSSION

4.1. Characterisation of undoped WO_3 nanowires

4.1.1 UV-visible absorption and band gap energy determination

The absorption bands of the synthesized nanocatalyst were determined using UV-visible spectrophotometer and the UV – visible absorption spectra of WO_3 nanowires are displayed in Figure 4.1.

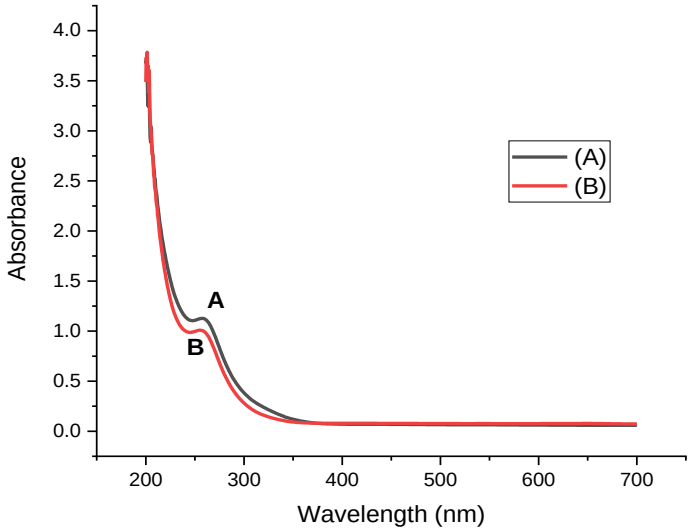

Figure 4.1: UV spectrum of the undoped WO_3 nanowires prepared at different synthesis conditions (Where A = 1 mol/dm^3, 200 ^{o}C 1 hour 30 min; B = 1 mol/dm^3, 140 ^{o}C and 2 hours 30 min)

The spectrum for the undoped WO_3 nanowires prepared at different synthesis conditions revealed absorption band at approximately 280 nm in UV region of the spectrum, however, the absorption of the various Cl – Ca co-doped WO_3 nanowires shown in Figures 4.2 to

Figure 4.5 demonstrated shifting of absorption bands towards the visible region of the

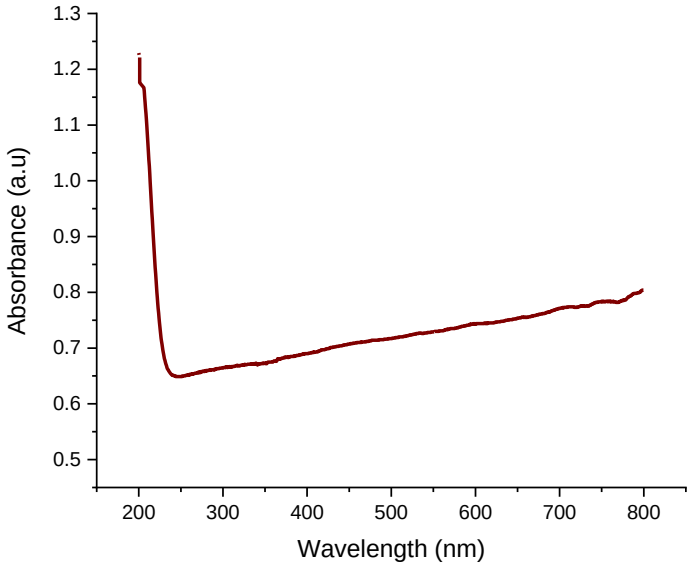

Figure 4.2: UV spectrum of doped sample at 1c:1a of the dopants

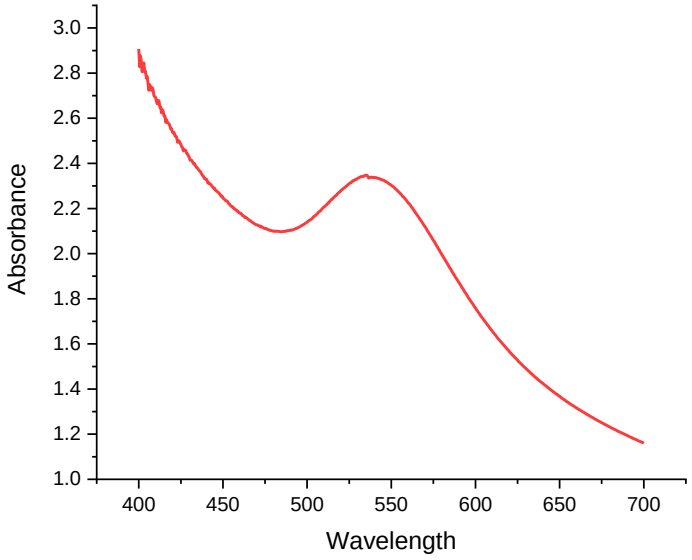

Figure 4.3: UV spectrum of doped sample at 1c:2a of the dopants

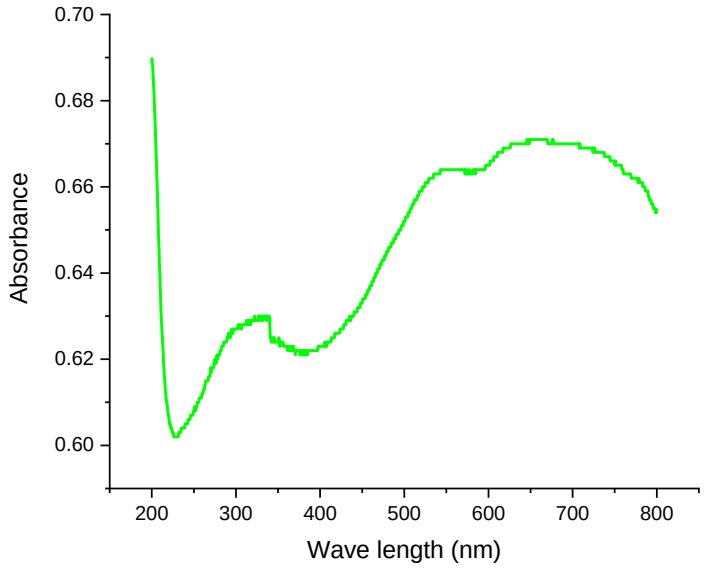

Figure 4.4: UV spectrum of doped sample at 2c:1a of the dopants

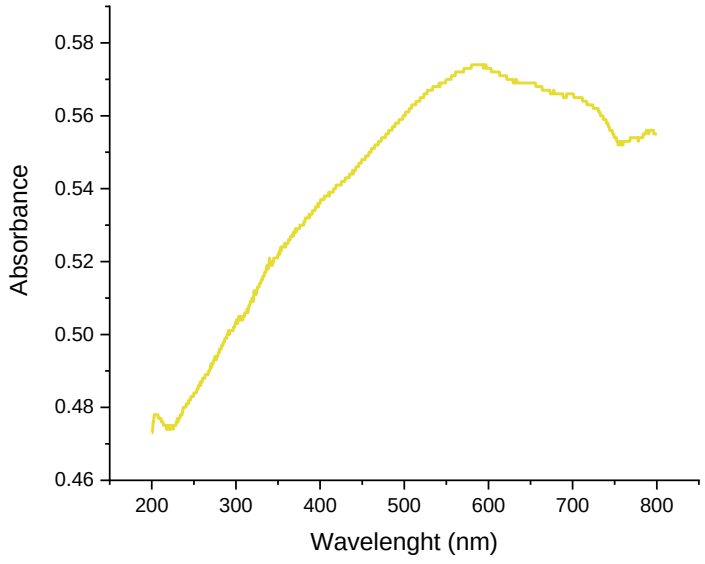

Figure 4.5: UV spectrum of doped sample at 4c:1a of the dopants

spectrum except for equal amount of the dopants (1c:1a).This shows that equal amount of dopants has no effect in shifting the nanowires towards the visible region. On the other hand, tungsten trioxide nanowires co-doped with chlorine and calcium with mixing ratio (1:2), a sharp increase in absorption threshold at around wavelength of 600 nm, which suggest excitation of electrons from the valence band to the conduction band.

In Figure 4.3, when the amount of chlorine was twice that of calcium in the composite matrix (2:1) the absorption peak increased from the UV region (230 nm) to visible region (420 nm). When the amount of chlorine was then doubled (4:1), a shift in the absorption thresholds towards the visible region (400 – 700 nm) was observed (Figure 4.4). This extension from the UV region to the visible region indicates reduction of the band gap facilitated by the introduction of the doping ions (Sivakarthik *et al*., 2016). Furthermore, the reduction in the band gap could also be linked to an s-p (4s orbital in Ca and 3p orbital in chlorine) interaction that occurs between the dopants and oxygen (2p orbital) in the crystal lattice of WO_3. However, large ionic radii of calcium caused more polarization of the dopants and the displacement of oxygen in the lattice framework of WO_3 thus responsible for a shift in the absorption band from the UV region to the visible region. Figure 4.6 and Table 4.1 show the Tauc plot and calculated band gap of the undoped and co-doped samples of the undoped and co-doped samples.

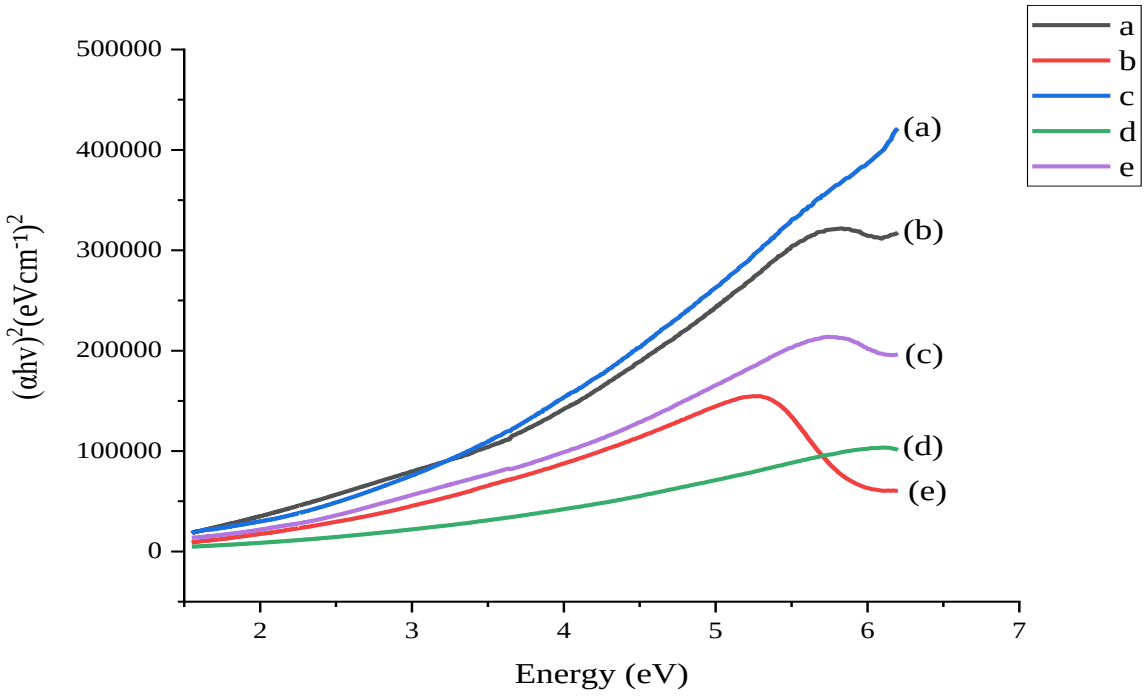

Figure 4.6: Band gap plot of the undoped and doped samples. Where a = WO_3, b = 1c:1a, c = 1c:2a, d = 2c:1a, e = 4c:1a

Table 4.1: Calculated band gap of the undoped and co-doped WO_3 nanowires.

Sample	**Undoped WO_3**	**1c :1a**	**1c:2a**	**2c:1a**	**4c:1a**
Band gap (eV)	2.7	2.6	2.4	2.3	2.2

It was observed that increase in the amount of chlorine dopant in the composite matrix (as seen in 2c:1a and 4c:1a) resulted to significant reduction of the band gap because Cl doping enables the creation of energy levels between the valence band and the conduction band of

WO_3 thus promoting the transition of electrons and narrowing the band gap (Wang *et al*., 2017).

In addition, the presence of chloride dopant tends to increase surface acidity and cause the formation of reduced ions of W^{5+} due to charge compensation between W^{6+} and Cl^-. Hence, the charge separation and enhancement of the photo induced processes can be achieved and subsequently preventing enlargement of the band gap (Bayan *et al*., 2017). Doping with calcium has been suggested to induce ionic bonding between the dopant (calcium) and the host (WO_3) by the substitution of O atoms with Ca atoms on WO_3 thus enhancing polarization which may favor adsorption of pollutants from aqueous matrix.

4.1.2. XRD analysis of undoped WO_3 based nanowires

The mineralogical phase of the synthesized nanomaterials was examined using X-ray Diffraction technique and the diffractogram of the various WO_3 samples prepared at different conditions is displayed in Figure 4.7.

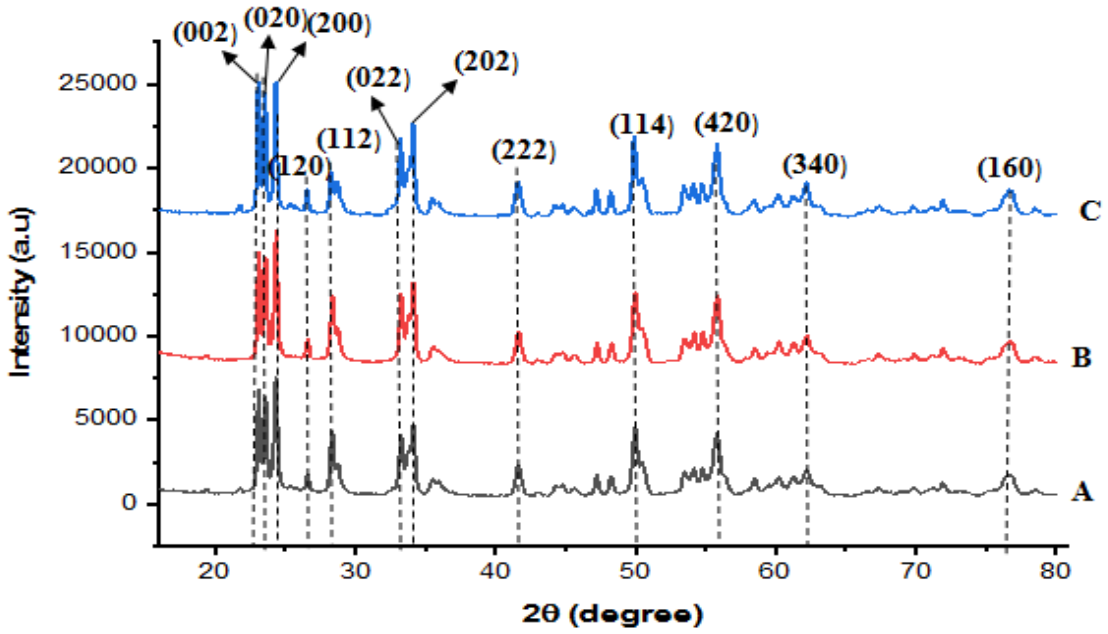

Figure 4.7: XRD pattern of WO_3 prepared at different conditions

Where A = 1 mol/dm^3, 200 ^{o}C 1 hour 30 min; B = 1 mol/dm^3, 140 ^{o}C and 2 hours 30 min and C = 0.55 mol/dm^3, 200 ^{o}C and 2 hours 30 mins

The following conditions were used for the synthesis of WO_3 nanowires: (a) concentration of the tungsten salt precursor (1 mol/dm^3), hydrothermal temperature (200°C) and hydrothermal time (1h 30 min), (b) 1 mol/dm^3, 140°C and 2h 30 min, and (c) 0.55 mol/dm^3, 200 ^{o}C and 2 h 30 min represented as condition A, B and C respectively. XRD pattern showed different diffraction peaks at Bragg angle (2θ) values of 23.12°, 23.58°, 24.59°, 33.26°, 34.17°, 36.29°, 50.73°, 55.93°, 62.42°, and 76.94° corresponding to the miller indices: (002), (020), (200), (120), (112), (022), (202), (222), (114), (420), (340), and (160). These peaks can be indexed to the WO_3 monoclinic structure using conditions A and B. These correspond to Joint Committee on Powder Diffraction Standards (JCPDS) file number (JCPDS-01-072-0677). The diffraction peak for condition C at Bragg angle(2θ) values of 24.13^o, 24.49^o,

25.89^{o}, 34.62^{o}, 36.18^{o},40.39^{o}, 52.37^{o}, 54.37^{o}, 61.24^{o}, 73.49^{o} and 77.89^{o} corresponding to the miller indices: (002), (020), (200), (112), (114), (022), (202), (040), (114), (241), and (420). These peaks can be indexed to the WO_3 triclinic structure for condition C. These correspond to Joint Committee on Powder Diffraction Standards (JCPDS) file numbers: 01-072-0677. No additional peaks were observed, hence confirming the high purity of the synthesized nanowires. The phase difference observed in condition C could be attributed to the difference in concentration of the precursor salt used during the synthesis. The mean crystalline size was calculated from the full width at half maximum (FWHM) of the XRD lines using equation 2.2 from page 26. The average crystalline sizes were found to be 14.39 nm, 14.83 nm and 14.93 nm for undoped WO_3 nanowires prepared using conditions A, B and C respectively. This shows that crystalline size increases as the reaction time increases. Nagyne-kovacs *et al*. (2019) and Fu *et al*., (2014) independently reported the formation of well crystallized monoclinic WO_3 nanowires prepared hydrothermally at reaction temperature closer to the one in this study.

4.1.3. XRD pattern of chlorine and calcium co-doped WO_3 nanowires composites

The XRD pattern of the doped WO_3 prepared by hydrothermal approach using different mixing ratios of chlorine and calcium dopants is presented in Figure 4.8.

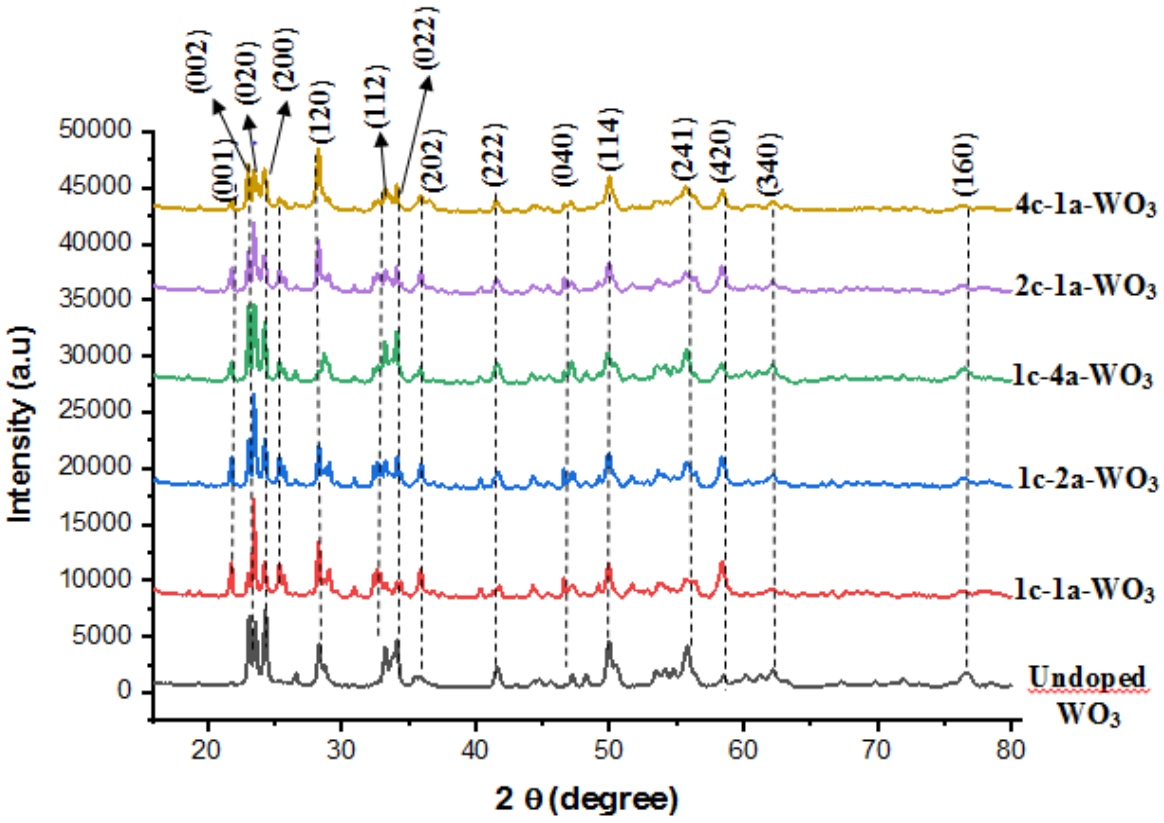

Figure 4.8: XRD patterns of Cl and-Ca doped WO_3 nanowires at different mixing ratios

The XRD patterns of undoped WO_3 nanowires alone as displayed in Figure 4.8 belongs to monoclinic phase with (JCPDS Card No: 01-72–0677, space group P21/n (14), a = 7.306 Å, b = 7.540 Å, c = 7.6892 Å) with large diffraction intensities for (020) and (120) peaks positioned at 2θ values of 23.58°, 24.59° respectively. In addition, the following characteristics planes (002), (200), (112), (022), (040), (202), (222), (114), (241), (420), (340), and (160) were positioned at 2θ values of 23.12°, 23.58°, 33.26°, 34.17, 36.29°, 48.24°, 50.73°, 55.93°, 56.24°, 62.42°, and 76.94° respectively. The presence of sharp peaks and intense diffraction peaks suggests the formation of crystalline nature of the synthesized WO_3 nanowires. For the co-doped nanocomposites coded (1c-1a-WO_3, 1c-2a-WO_3, 1c-4a-

WO_3, 2c-1a-WO_3 and 1c-4a-WO_3), the diffraction peaks belonging to Ca and Cl along with monoclinic WO_3 were identified. It was noticed that the pure WO_3 and co-doped nanocomposites coded (1c-1a-WO_3, 1c-2a-WO_3, 1c-4a-WO_3, 2c-1a-WO_3 and 4c-1a-WO_3) all belong to the same monoclinic phase of WO_3 with JCPDS card no: 01-72–0677. This suggests that the incorporation of Cl^- and Ca^{2+} onto the lattice framework of WO_3 did not distort the phases however influenced the morphology, and their crystallite sizes. Doped samples with high amount of Ca, low Cl and equal amount of Ca and Cl (1c-4a-WO_3, 1c-2a-WO_3, and 1c-1a-WO_3, respectively) caused overlapping with the introduction of a new peak assigned to (100) plane while the plane at (120) was shifted from 26.55° to 25.33°. This shift to a lower angle may be attributed to the expansion of the lattice of WO_3 as a result of the difference in ionic radii of Ca and O and thus stabilizing the lattice of WO_3 by increasing its ionicity for chemical reaction. For low Ca and high Cl-concentration (2c-1a-WO_3 and 4c-1a-WO_3), the structure of the sample remained as the crystalline feature of the as-prepared WO_3 was not affected however an extra peak assigned to planes (100) become more visible whereas the plane (112) increased in intensity as compared to the other crystallographic peaks.

Generally, a closer look at the XRD pattern of the doped-WO_3 suggests that all the diffraction peaks positions were shifted to a lower diffraction angle for the calcium and chlorine doped samples. Based on Bragg's law, the observed peak shift can be related to the increase in lattice parameters, which confirms the intercalation of different Ca and Cl contents into the WO_3 layers of the nanowires. Crystallographic growth direction of these products has been confirmed by HRTEM analysis. Similar deductions were made by Kong *et al*., (2020) who synthesized WO_3 nanoplate film was prepared by nitric acid corrosion of W foil using oxalic

acid following hydrothermal method and obtained monoclinic phase. The mean crystalline size was also calculated from the full width at half maximum (FWHM) of the XRD lines using the same equation 3.1 in page 34. The average crystalline size was found to be 28.48 nm, 22.64 nm, 17.18 nm, 11.42 nm, and 10.51 nm for 1c:1a, 1c:2a, 2c:1a, 4c:1a and 1c:4a respectively. The decrease in size may be attributed to the formation of new defects on the surface of WO_3 as reported by Gurkan *et al*., (2017). Also, it may be due to the penetration of Ca^{2+} into WO_3 lattice or bonding with oxygen on the surface of WO_3 to form metal oxide which limited the growth of WO_3 nanowires as reported by Li *et al*., (2020). However, this report is quite different from the deductions of Han *et al*., (2016) who reported an increase in the crystal growth of WO_3 with the incorporation of Sulphur (a non-metal dopant) alone. The difference in the crystal growth of this study with the findings of Han *et al*., (2016) may be attributed to the nature of the dopant. However, Silveira *et al*., (2020) observed that with increasing amount of Mo- there was a reduction in crystalline size.

4.1.4. HRSEM analysis of the undoped WO_3 nanowires synthesized at different conditions

HRSEM was used to determine the morphology of the samples. Plate I show the HRSEM images of the undoped WO_3 nanowires prepared at the following conditions: (a) concentration of the tungsten salt precursor (1 mol/dm^3), hydrothermal temperature (200 ^{o}C) and hydrothermal time (1h 30 min), (b) 1 mol/dm^3, 200 ^{o}C and 1 h 30 min; 1 mol/dm^3, 140 ^{o}C and 2 h 30 min, and (c) 0.55 mol/dm^3, 200 ^{o}C and 2 h 30 min.

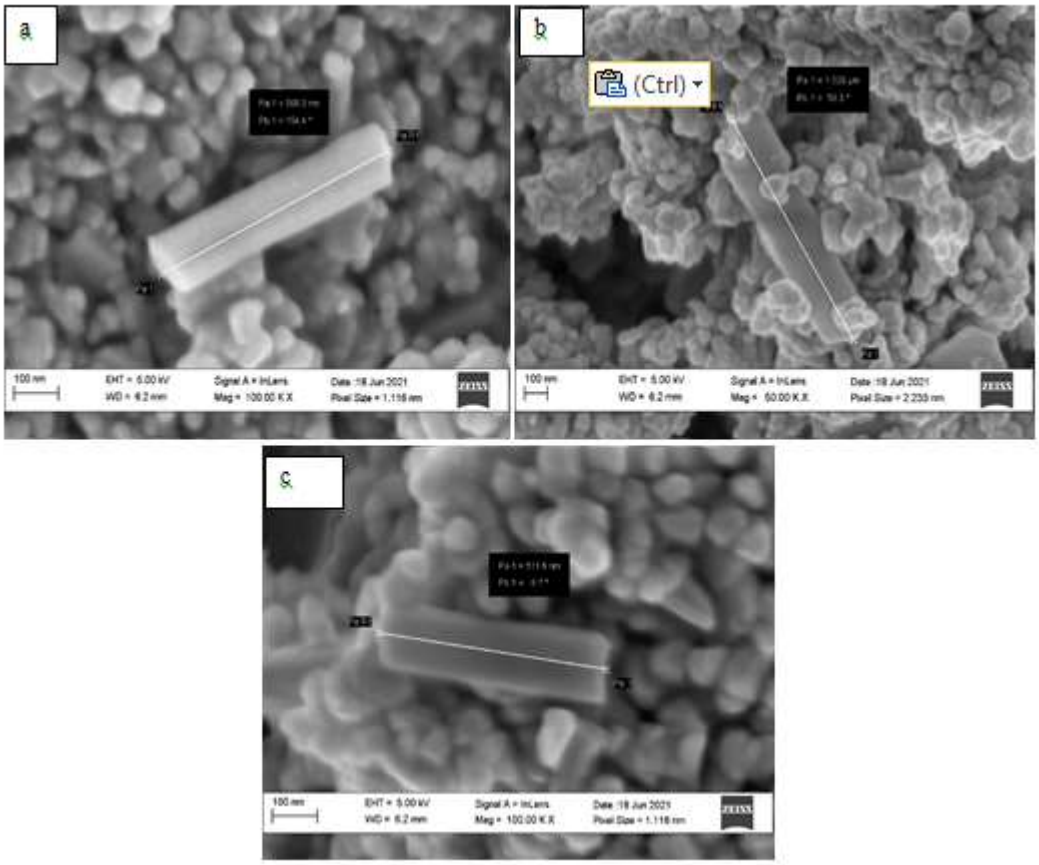

PLATE I: HRSEM Micrographs of WO_3 nanowires prepared at: (a) 1 mol/dm^3, 200 ^oC 1 h 30 min, (b) 1 mol/dm^3, 140 ^oC and 2 h 30 min, and (c) 0.55 mol/dm^3, 200 ^oC and 2 h 30 min

These images clearly indicate that the samples consist of a mixture of agglomerated spherical nanoparticles and bamboo like- nanowires of different sizes and aspect ratios. WO_3 nanowires synthesized at 1 mol/dm^3, 200 ^oC and 1h 30 min had a length of 568.3 nm and a diameter of 125.1 nm and an aspect ratio of 4.54, while the WO_3 nanowires synthesized using the following conditions: 1 mol/dm^3, 140 ^oC and 2 h 30 min, had a length of 1029 nm and a diameter 247.1 nm with an aspect ratio of 4.16, and the nanowires produced using 0.55

mol/dm^3, 200 ^{o}C and 2 h 30 min were 104.5 nm in diameter and 1089 nm in length with an aspect ratio of 10.42, showing well-developed nanowires. However, it can be observed that as the reaction time increased, the length of the nanowires increased indicating that reaction time has effect on the morphology of nanowires (Tehrani *et al*., 2020).

The aspect ratio with respect to its relevance on the photocatalytic performance of the synthesized nanowires was also determined and it was observed that as the growth duration time increased the aspect ratio and length also increased significantly. This also suggests that duration time has effect on the growth length of the nanowires. Furthermore, the higher the aspect ratio, the higher the photocatalytic performance because great level of surface defect would be available leading to a much better charge separation and high surface area (Das *et al.*, 2019).

Phuruangrat *et al*. (2010) had reported that WO_3 nanowires produced by conventional hydrothermal method had lengths of 200-300 nm and a diameter of 10–15 nm (aspect ratio of 13-30), whereas hexagonal WO_3 nanowires produced from microwave assisted hydrothermal method were more than 5 mm long a ..nd less than 10 nm in diameter, with an average aspect ratio of >625.The aspect ratio of hexagonal WO_3 produced by the microwave assisted hydrothermal synthesis is higher than the value reported in this study and this can be attributed to difference in the nature of tungsten salt precursor and the presence of surfactants such as oxalic acid in the present study.

4.1.5. HRSEM analysis of chlorine and calcium co-doped WO_3 nanowires

The HRSEM images of WO_3 samples co-doped with different chlorine and calcium contents are presented on Plate II (a-e)

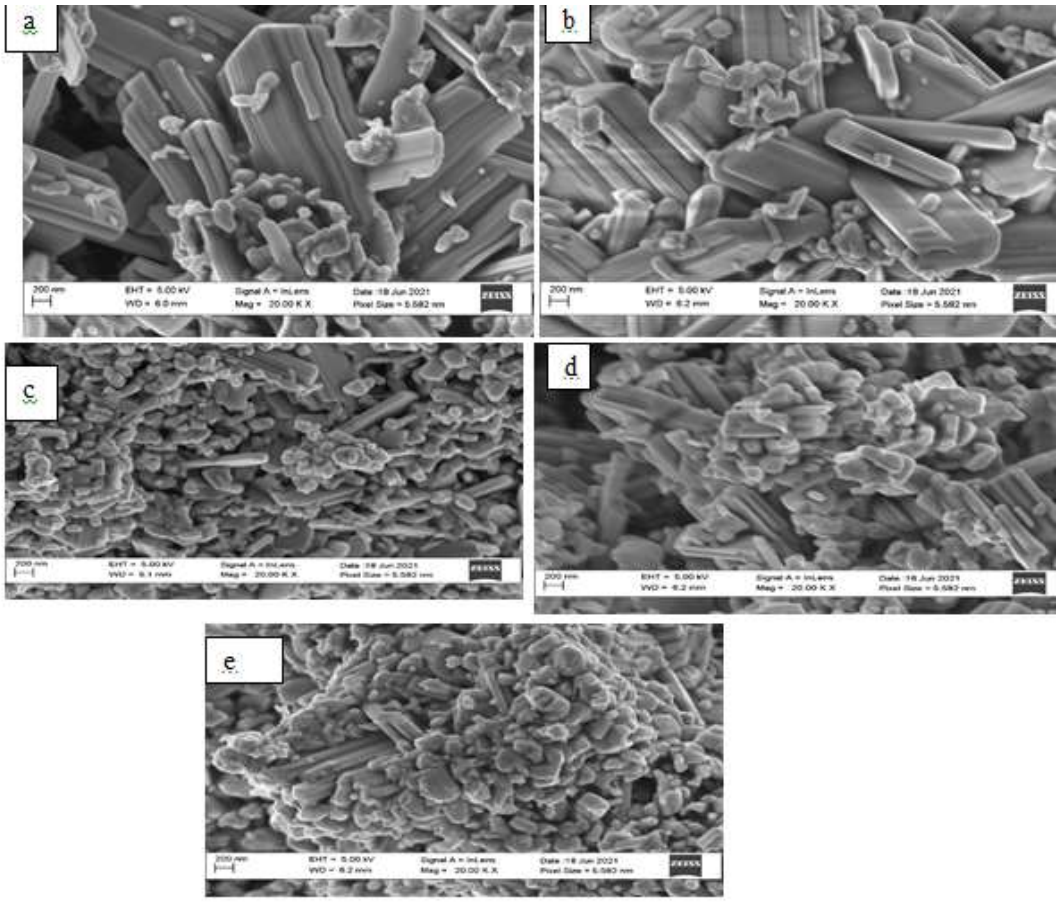

PLATE II: HRSEM Micrographs of doped WO_3 nanowires (a) 1c-1a doped WO_3 (b) 1c-2a doped WO_3 (c) 1c-4a doped WO_3 (d) 2c-1a doped WO_3 (e) 4c-1a doped WO_3

The morphology of Plate II (a) reveals the formation of closely packed and block bundles of nanowires with varying lengths, ranging from 645.85 nm to 1.440 μm and average bundle diameters ranging from 100 to 250 nm. In Plate II (b) with mixing ratio of chlorine to calcium (1:2), the average diameter was found to be 386.18 nm, while the average length was around 992.88 nm., In the case of Plate II(c), where the mixing ratios twice that of Plate II (b), the bundle-like nanowires had an average diameter of about 392.81 nm and a length up to 999.88 nm. Plate II (d) twice amount of chlorine over calcium (2:1), WO_3 nanowires had an average

diameter of 367.84 nm with a length measured to be about 1.527 μm and finally plate II (e) exhibited a diameter of 346.01 nm and a length of 1.33 μm.

In general, the produced block bundles of Cl-Ca-WO_3 nanocomposite samples were longer and wider in diameter than those of the pure WO_3 nanowires due to the addition of the two dopants. However, when the Cl and Ca-content was increased on the lattice layer of WO_3, as seen in Plate II (c) and (e), there was agglomeration of the nanowires linked to the formation of oxygen defects in the crystal lattice of WO_3 which act as charge trapping centers, thus enhancing its photoactivity (Pauekphong *et al*., 2019). Furthermore, the increase in length and diameter observed in the doped samples could be attributed to the large ionic radius of Ca^{2+} (1.80Å) and Cl^- (1.00 Å) and ease replacement of O^{2-} which have smaller ionic radius (0.60 Å) in the lattice of WO_3 and hence causing a distortion. Thus, both Ca^{2+} and Cl^- were deposited on the surface of WO_3 monoclinic framework, leading to an expansion of the crystal lattice as confirmed by the XRD result. Furthermore, the presence of either chloride or calcium ions in the composite could accelerate its photocatalytic activities facilitating electron transfer and oxygen mobility in the doped samples. Similar deductions have been made by Thummavichai *et al*. (2021) that synthesized Na_yWO_x bronze nanowires and found that by increasing the Na-dopant amounts to 1:12, 1:8 and 1:4, mixtures of nanorods, nanoplates and agglomerated bundled structures were observed, and the size of nanowires increased with Na-contents inside the framework.

4.1.6 EDS analysis of the undoped WO_3 nanowires

The energy dispersive spectrometric (EDS) analysis was employed to analyze the composition of the WO_3 nanowires. As shown in figures 4.9 - 4.11 below, only oxygen,

tungsten elements were present in the nanowires. Tungsten and oxygen having 3.78 KeV and 2.96 KeV respectively. However, no other impurity was present as similarly reported by Wanjun *et al*., (2016) in the fabrication of WO_3 nanowires via the hydrothermal method the presence of guanidine sulfate as a dispersant and Na_2WO_4 as a precursor salt. None detection of other element confirmed high purity of the synthesized WO_3 nanowires**.** Table 4.2 also show the percentage by weight of the elements present in the undoped nanowires

Table 4.2: Elemental composition of the undoped nanowires

Sample	A	B	C
Element	Wt (%)	Wt (%)	Wt (%)
O	17.25	12.90	14.25
W	82.75	87.10	85.75
Total	100	100	100

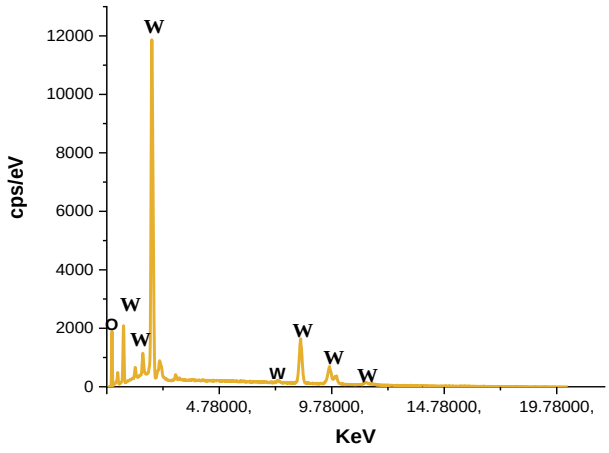

Figure 4.9: Elemental composition of undoped nanowires prepared at 1 mol/dm^3, 200 ^{o}C 1h 30 min

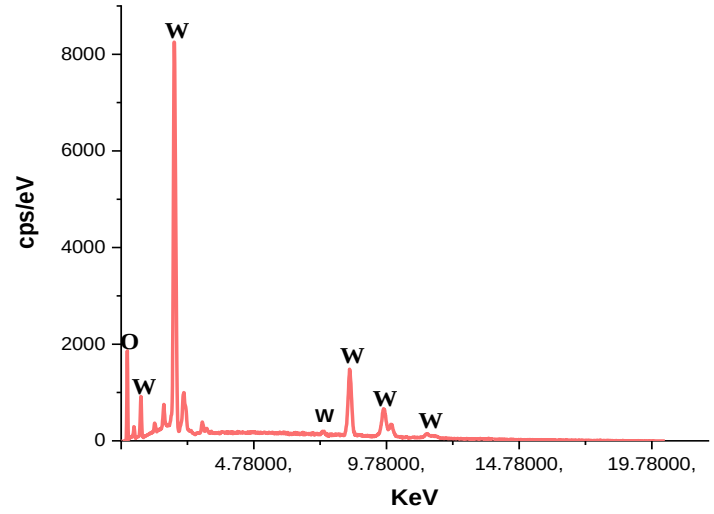

Figure 4.10: Elemental composition of undoped nanowires prepared at 1 mol/dm^3, 140 ^{o}C and 2 h 30 min

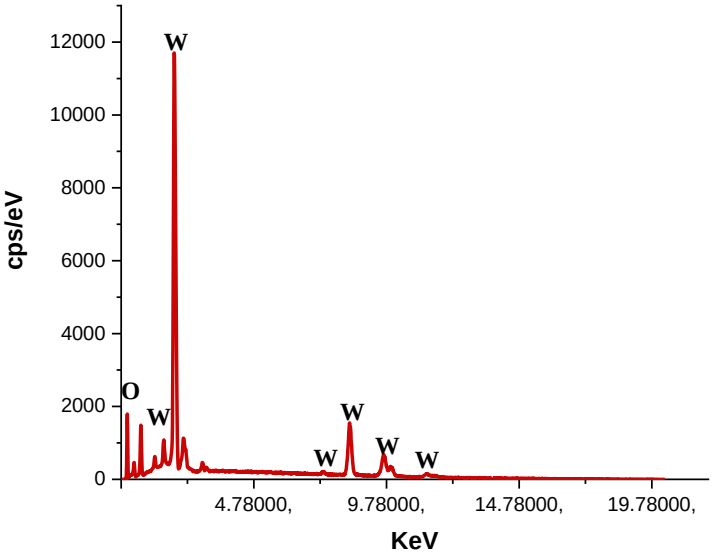

Figure 4.11: Elemental composition of undoped nanowires prepared at 0.55 mol/dm^3, 200 ^{o}C and 2 h 30 min

4.1.7 EDS analysis of the Cl and Ca doped WO_3 nanowires

Energy dispersive spectrometric (EDS) analysis for the doped samples is presented in Figure 4.12.

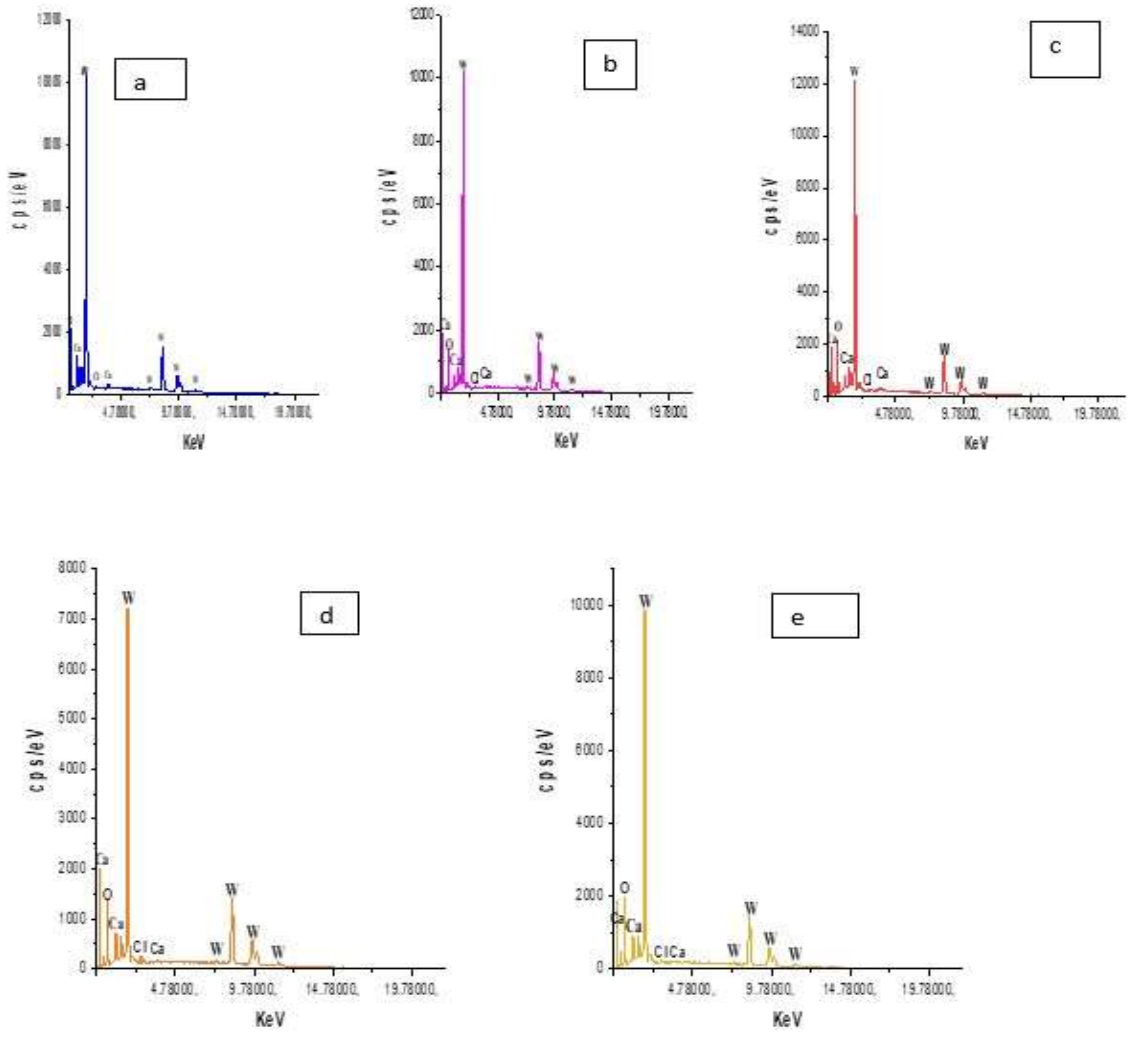

Figure 4.12: **EDS analysis of the Cl and Ca doped WO_3 nanowires (a) 1c-1a doped WO_3 (b) 1c-2a doped WO_3 (c) 1c-4a doped WO_3 (d) 2c-1a doped WO_3 (e)4c-1a doped WO_3**

As expected, all the nanowires consisted of W, O while 1c-1a-WO_3 nanowires included Ca and Cl in stoichiometric proportion. Samples 1c-2a-WO_3 and 1c-4a-WO_3 revealed that the ratio of Ca increased from 1.83 % to 3.66 %, while Cl remained fairly constant at 0.64 %.

Furthermore, in samples 2c-1a-WO_3 and 4c-1a-WO_3, Cl also increased from 1.30 to 2.58 % indicating a proportionate increase when the ratio of Cl in the sample was increased from 2 to 4.Table 4.3 also show the percentage by weight of the elements present in the Cl-Ca codoped nanowires

Table 4.3: Elemental Composition of the Doped Nanowires

Sample	**1c-1a-WO_3**	**1c-2a-WO_3**	**1c-4a-WO_3**	**2c-1a-WO_3**	**4c-1a-WO_3**
Element	**Wt (%)**	**Wt (%)**	**Wt (%)**	**Wt (%)**	**Wt (%)**
O	18.17	14.01	14.87	17.36	16.20
Cl	0.76	0.76	0.74	1.40	2.68
Ca	0.92	1.83	3.66	0.91	0.91
W	80.15	83.40	80.73	80.33	80.21
Total	100	100	100	100	100

4.1.8 HRTEM analysis of undoped WO_3 and Cl-Ca doped WO_3 nanowires and SAED pattern of the WO_3 based nanowires

Plate III (a-l) shows the low and high magnification HRTEM images of the undoped and Ca-Cl doped nanowires.

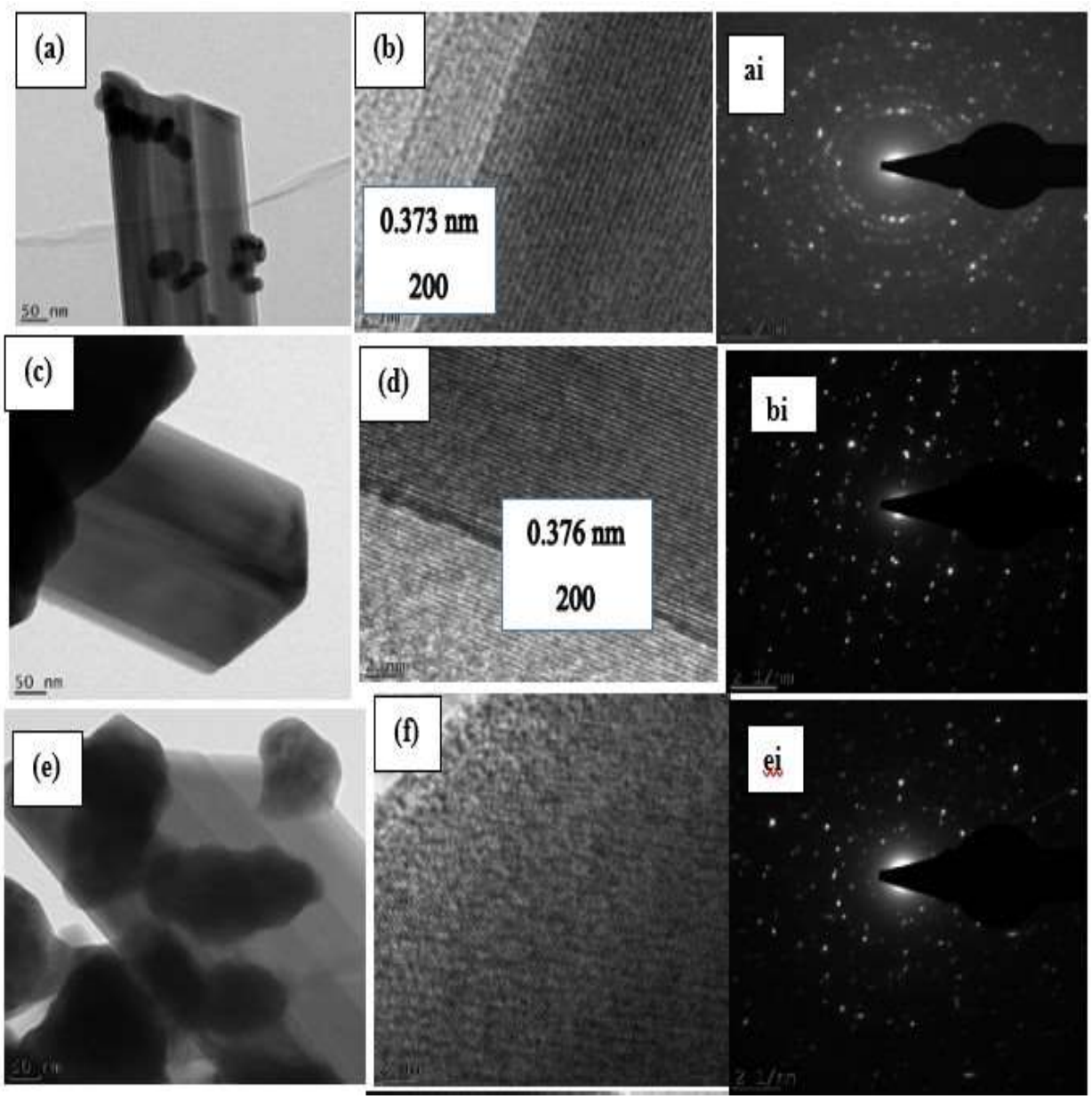

Plate III: HRTEM Micrographs of WO_3 nanowires of (a) undoped WO_3 (c) 1c-1a doped WO_3 (e) 1c-2a doped WO_3 (g) 1c-4a doped WO_3 (i) 2c-1a doped WO_3 (k)4c-1a doped WO_3

According to the HRTEM at low and high magnification, the undoped nanowires in Plate III (a) composed of several stacked wires approximately 1.0 ± 0.5 μm in length and 100 ± 60 nm in diameter. The TEM images also show the capping of oxalic acid on the surface of W

assisting the growth of the nanowires. The high magnification micrograph in Plate III (b) revealed that the fringe interval of 0.373 nm for the undoped WO_3 agrees well with the d-spacing of (200) lattice planes perpendicular along the axis of the nanowires. The left – hand side represent low-resolution images (c, e, g, i, k) while the right-hand side represent high resolution images (d, f, h, j, l). Low-resolution images reveal that each nanowire was 1.44 ± 0.5 μm long and 340 ± 87 nm wide. Some secondary branches with random length and diameter (c, e, g, i and k) were also observed on the surface of the nanowires. These branches also increased as the amount of each of the dopants is doubled (e, g, i, k) which is supported by the HRSEM result. The increment in length and diameter of the doped nanowires could be attributed to the expansion of the crystal lattice during the incorporation of Ca and Cl as supported by the XRD result. It was observed that the interplanar distance of the doped samples varied from (0.367 - 0.377 nm), indicating that they all grew along the [200] plane. The HRTEM images also revealed a non-homogeneous distribution of nanowires of different thickness, suggesting that the diameter of the nanowires strongly depended on the number of packed wire units. This could be attributed to the effect of growth duration time during synthesis (Zhang *et al*., 2012).

Plate III (ai-ki) reveals the selected area electron diffraction (SAED) pattern of the undoped and Cl-Ca doped WO_3 nanowires. It was found that all the samples exhibited diffraction rings, corresponding to the (002), (020), (200), (120), (112), (022), and (202) planes of monoclinic WO_3 which matches the XRD results. Also, it was observed that increase in the dopants influenced the growing patterns of the nanowires based on the interaction between the dopants and thus making the samples to have diffraction rings. Previous report by Navarro

et al. (2014), established that (020) and (002) crystal planes of WO_3 exhibited a single crystal pattern of monoclinic phase of WO_3.

Thummavichai *et al*. (2021) confirmed the lattice spacing of 0.379 nm from HR-TEM and SAED pattern of pure $W_{18}O_{49}$ and the 1:16 of Na: W doped sample. This matched well with the d value obtained in this study. While the SAED patterns of higher Na-doped WO_3 samples had crystal planes (002) and (200) and the d spacing matched well with the WO_3 monoclinic nanowires.

4.1.9 BET results of synthesized undoped WO_3, and doped 4c:1a, 2c:1a nanowires

The N_2 adsorption – desorption curve of the synthesized undoped and co-doped WO_3 nanowires is shown in Figure 4.13 – 4.15.

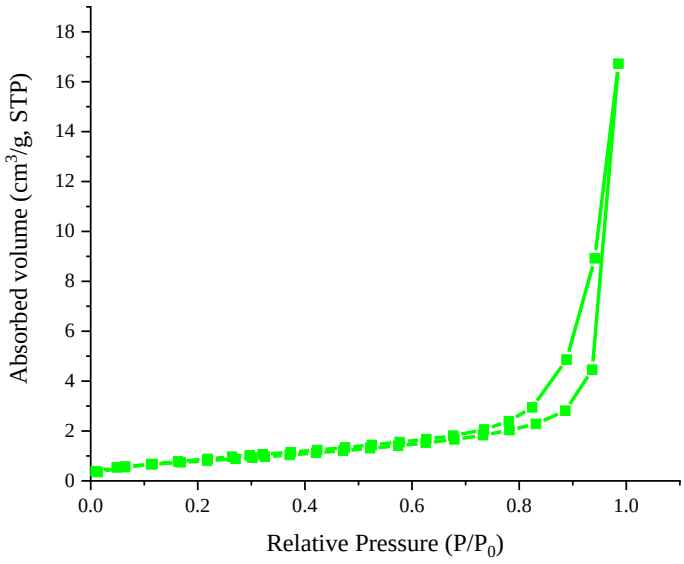

Figure 4.13: BET plot of undoped WO_3

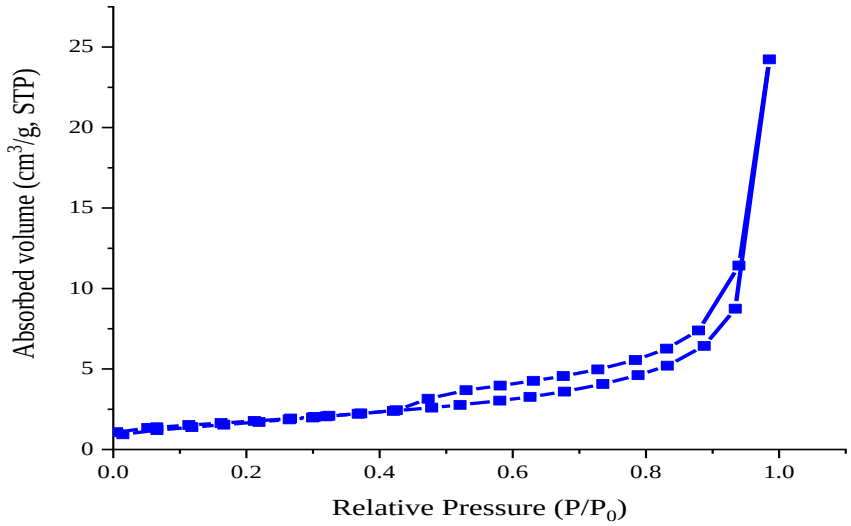

Figure 4.14: BET plot of doped sample (2c:1a)

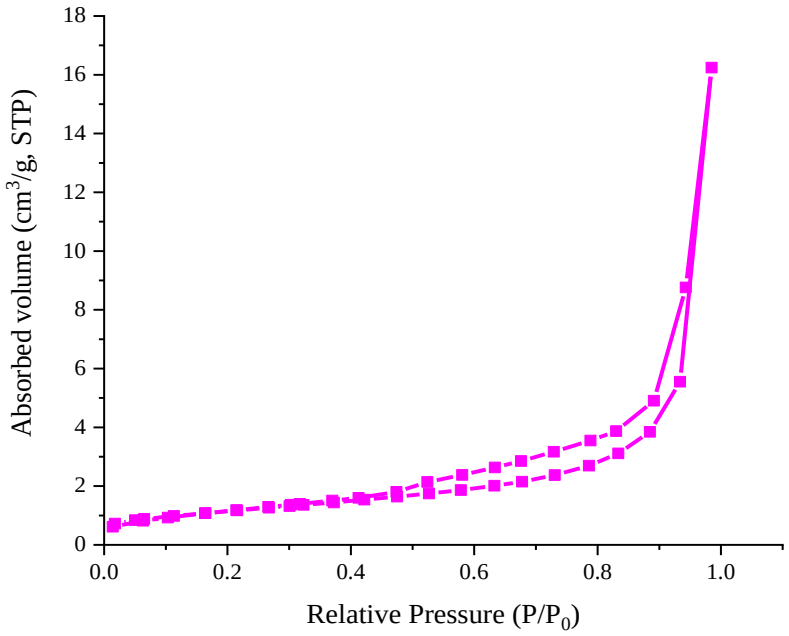

Figure 4.15: BET plot of doped sample (4c:1a)

According to IUPAC, the isotherms curves in Figures 4.13 - 4.15 can be classified as type II representative of a mesoporous material (Sotomayor *et al*., 2018). The BET surface area, pore volume and pore diameter of the samples are shown in Table 4.4.

Table 4.4: BET surface area, pore size and pore volume of doped and undoped samples

Samples	**Surface area (m^2/g)**	**Pore diameter (nm)**	**Pore volume (cc/g)**
4c:1a	24.602	3.601	0.109
2c : 1a	16.031	4.048	0.082
Pure WO_3	4.216	15.389	0.030

For the undoped WO_3 nanowires, the BET surface area was 4.216 $m^2\ g^{-1}$ which is quite lower than what was obtained by Thummavichai *et al*. (2021). This could be attributed to the method of preparation, precursor salt and the dopants used. For the doped samples, there was a significant increase in the surface areas to 16.031 and 24.602 m^2g^{-1} respectively for the co-doped samples. It can be observed that the doped samples had higher surface area than the undoped WO_3 nanowires. This can be attributed to the synergistic effect of the co-dopants as result of the insertion of Ca^{2+} and the substitution of Cl^- for oxygen in the lattice framework of WO_3. Furthermore, as seen in 4c:1a, whose surface area is the highest; the increase could be attributed to increase in concentration of Cl^- ions compared to calcium ions.

Increase in surface area is beneficial for photocatalytic activity because it improves incident light absorption by the photocatalyst, and provides more active sites on the surface of the

photocatalyst, thus improving photo degradation. Similar trend was observed for the pore volume, as there was significant increase in the pore volume of the doped samples (0.082 cm^3/g and 0.109 cm^3/g respectively) compared to the undoped WO_3 with a pore volume of 0.030 cm^3/g. The pore diameter which falls within 2 – 50 nm further confirmed that the synthesized undoped and co-doped nanowires were mesoporous in nature. Silveira *et al*., (2020) reported mesoporous nature for all the doped samples of Mo-doped WO_3 nanowires that were synthesized for the adsorption of methylene blue dye from wastewater.

4.1.10. Physico-chemical characterisation of indigenous dyeing wastewater

The results of the physicochemical assessment of the Indigenous dyeing water determined using the established standard procedure described in chapter three is presented in Table 4.5.

Table 4.5: Physico-chemical characterisation of the Indigenous dyeing wastewater

Parameters	Before degradation	After degradation			WHO limit
		WO_3	2c:1a	4c:1a	
Color	Deep brown	Colorless	Colorless	Colorless	Colorless
Odour	Pungent	Odourless	Odourless	Odourless	Odourless
Appearance	Cloudy	Clear	Clear	Clear	Clear
Temperature	29 ± 0.01	27 ± 0.02	27 ± 0.02	27 ± 0.02	40
pH	12.28 ± 0.01	10 ± 0.03	10 ± 0.03	10 ± 0.03	7.5 – 10
Electrical conductivity (µS/cm)	42.4 ± 0.01	41.96 ± 0.01	41.84 ± 0.01	39.60 ± 0.01	< 500
Total alkalinity (mg/l)	6240 ± 0.03	5920 ± 0.03	5600 ± 0.03	4400 ± 0.05	500
Total Hardness (mg/l)	512 ± 0.10	496 ± 0.10	480 ± 0.10	410 ± 0.10	25
COD (mg/l)	1073 ± 0.10	144 ± 0.10	96 ± 0.10	80 ± 0.10	< 120
BOD (mg/l)	245 ± 0.05	18.50 ± 0.05	14.70 ± 0.05	10.20 ± 0.05	50
TOC (mg/l)	150 ± 0.01	0.15 ± 0.01	0.08 ± 0.02	0.05 ± 0.02	10
CO_3 (mg/l)	3021.08 ± 0.05	2866.03 ± 0.05	2710.97 ± 0.05	2131.64 ± 0.05	NS
Cl (mg/l)	541 ± 0.01	392 ± 0.01	313.60 ± 0.01	784.00 ± 0.01	NS
Ca (mg/l)	33.90 ± 0.01	27.39 ± 0.01	110.84 ± 0.01	114.68 ± 0.01	NS
Mg (mg/l)	319 ± 0.09	360.19 ± 0.09	471.29± 0.09	394.24 ± 0.09	NS

NS = Not stated
WHO = World Health Organization (2017).

The raw indigenous wastewater collected was subjected to UV-visible spectroscopic analysis and the result shown in the Figure 4.16.

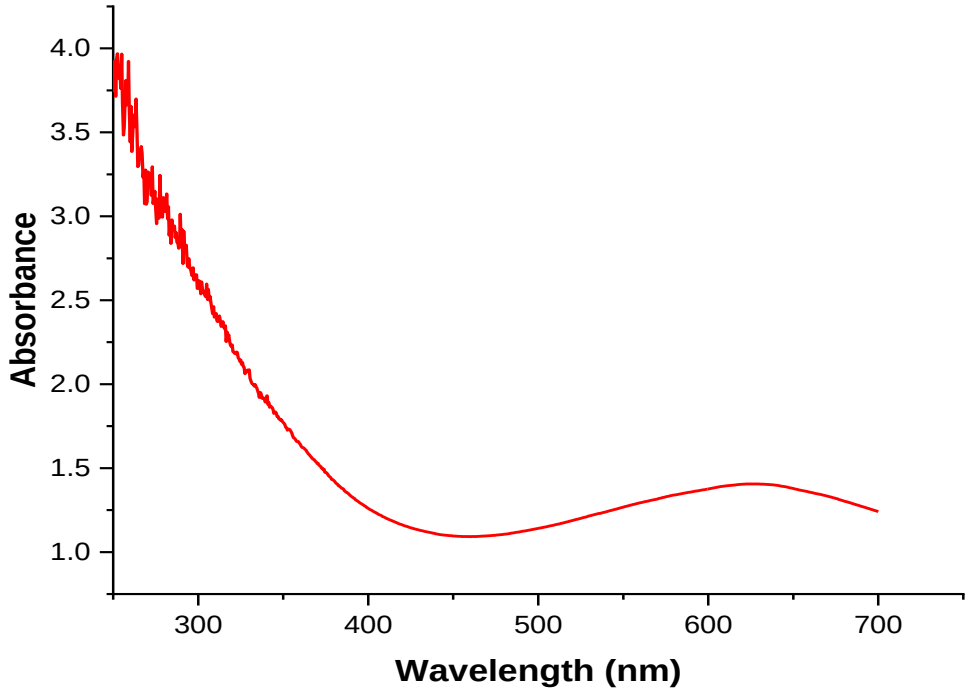

Figure 4.16: UV-Visible spectrum of the raw wastewater.

The result revealed absorption at the visible region at a wavelength of around 620 nm suggesting that the dye is Blue Benzactive SGLD reactive dyes. Overall, Table 4.35 represents the results of physico-chemical parameters of the raw wastewater before and after the photocatalytic activity. pH is an indicator parameter for acid-base level in water and it can be noticed the pH level of the raw wastewater is highly basic and far above the standard level before photocatalytic activity. This indicates the presence of highly basic dyes in the wastewater. Too high pH level of water could affect aquatic species and may alter the solubility of other important elements present in the water if the wastewater is being

discharged into water bodies without treatment. However, after photocatalytic activity it was observed that the pH level fall within the recommended limit and hence indicating the effectiveness of the catalyst produced.

Electrical conductivity (EC) is indicative of the degree of salinity in wastewater (Durotoye *et al*., 2018). It is also the ability of a solution to conduct electricity due to the presence of ionic species. Thus, high value of electrical conductivity indicates the abundance of ionic species in water. The results obtained shows that the electrical conductivity of the wastewater is above the standard limit and this could be attributed to the presence of high level of dissolved ions. High value of EC could alter the level of other indicative parameter of the water, e.g., high EC could increase the salinity of the water, affects the temperature of the water by increasing the warmness of water and hence may affect aquatic species if disposed into water bodies. Total alkalinity is a measure of the buffering capacity of water (Mohammed *et al*., 2020). High levels of alkalinity could be due to the presence of carbonates materials used at different stages (Scouring and fixing) of the dyeing process which can thus increase the pH level, turbidity and unsafe (Yassen and Scholz, 2018).

Biochemical oxygen demand is the amount of oxygen used when the organic matter present in a given volume of water is biologically degraded. High levels of BOD in water leads to a decrease in Dissolved oxygen and this could affect the survival of fishes and other aquatic organisms present in the water bodies to which this wastewater is discharged to. Dufantanye *et al*., (2022) also recorded high levels of BOD above the permissible limit as seen in this study as well when industrial wastewater discharge was analyzed.

Chemical oxygen demand (COD) is amount of oxygen required to chemically breakdown organic matters in a given water sample. High amount of COD in industrial wastewater indicates the presence of high organic matter which also leads to increased consumption of oxygen by organic matter decomposers causing the depletion of oxygen in the receiving water bodies and hence pollute the water. High value of COD could also be ascribed to the presence of softeners, detergents used during the dyeing process (Pensupa *et al*., 2017). The TOC value in this study is quite higher than the limit required. It can clearly be seen that the TOC level is considerably high due to the presence of oxidizable organic and inorganic substances such as dyes, heavy metals, resins, starch, solvents and other complex mixture of chemicals in the wastewater. However, Tijani *et al*., (2021) and Tijani *et al*., (2022) recorded higher TOC values and Uko *et al*., (2022) recorded lower TOC value than the one in this study, this could be as a result of different quantity of dyes used during the dyeing process.

4.1.11 Photocatalytic degradation

In order to study the effect of contact time on the photocatalytic activity of the synthesized nanomaterials, two indicator parameters (dye and COD) were studied with the following experimental conditions: volume of wastewater (50 cm^3) and photocatalyst dosage (0.02 g) were kept constant throughout the experiments. Control experiments were carried out in the dark with 4c:1a and under light without any photocatalyst. The photocatalytic experiments for the removal of dye and COD were investigated for 240 min and the results are shown in Figure 4.17 and 4.18 respectively.

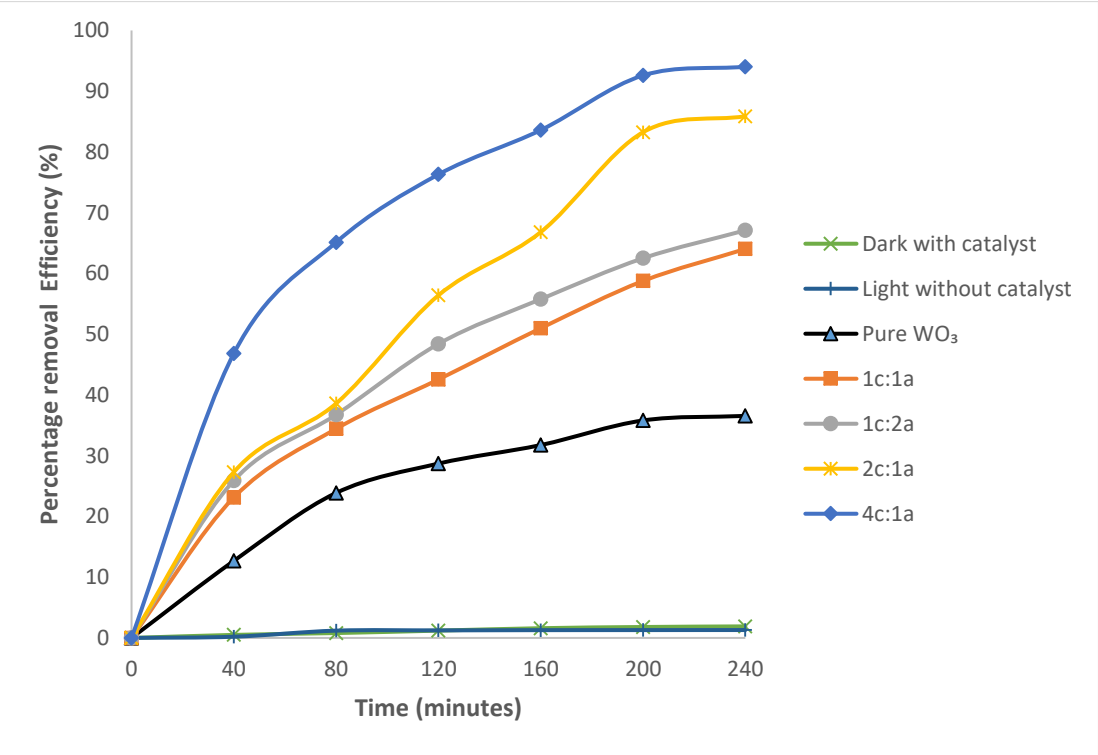

Figure 4.17: Comparison of the reactive dye degradation efficiency in the (a) dark with photocataylst, (b) in presence of light without photocatalyst, (c) pure WO_3, (d) 1c:1a, (e) 1c:2a, (f) 2c:1a and (g) 4c:1a in 50 cm^3 of the wastewater at room temperature with 0.02 g of each photocatalyst.

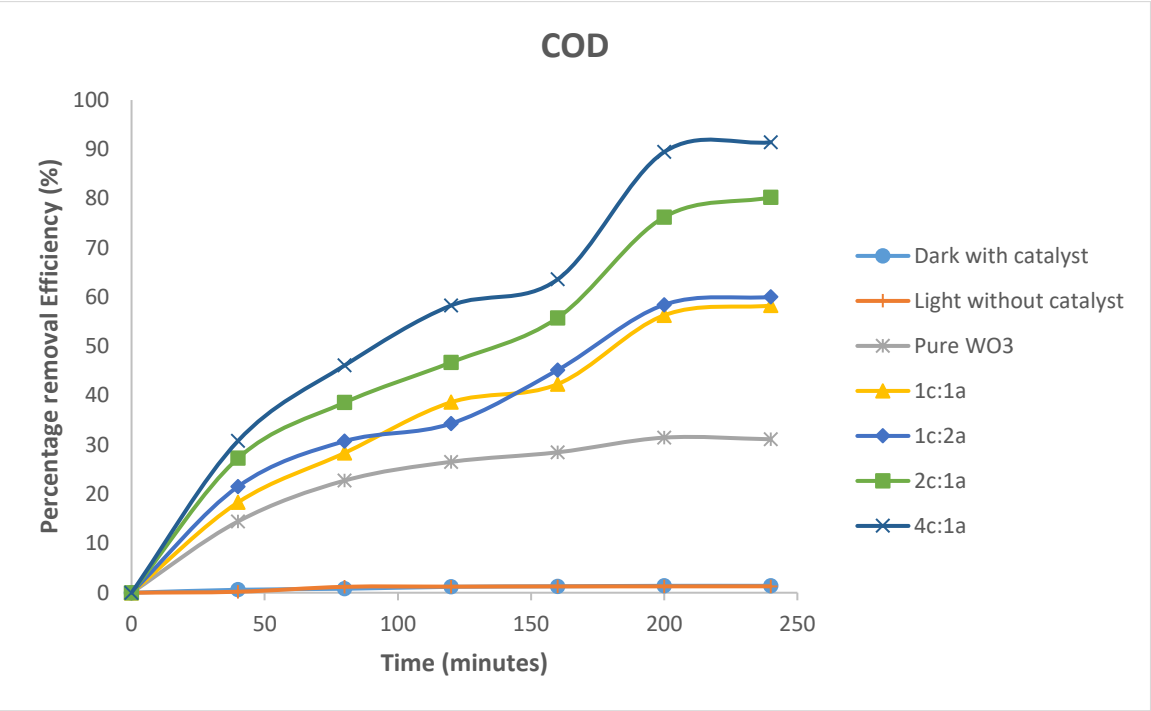

Figure 4.18: Comparison of the COD degradation efficiency in the (a) dark with photocataylst,(b)in presence of light without photocatalyst, (c) pure WO_3, (d) 1c:1a, (e) 1c:2a, (f) 2c:1a and (g) 4c:1a in 50 cm^3 of the wastewater at room temperature with 0.02 g of each photocatalyst.

The linear curve for both reactive dye and COD removal represent the control samples in the dark (adsorption process) and under sunlight without the photocatalyst (photolysis treatment). None reductions of reactive dye and COD indicates that the degradation of the dye molecules in the dyeing wastewater did not follow adsorption and photolysis process. Also, it was revealed that the percentage removal of both indicator parameters (reactive dye and COD) increased as the reaction time increased for all the nanocatalyst. This can be ascribed to their differences in band gap energy, morphology and surface area. This agrees with the findings of Tijani *et al.* (2022).

For reactive dye, at 40 mins, the order of removal is as follows: 10, 15, 20, 23 and 45 for pure WO_3, 1c:1a, 1c:2a, 2c:1a and 4c:1a respectively while at the maximum time of 240 mins the removal efficiency is 35, 55, 60, 90 and 94 respectively. Meanwhile, for COD, at 40 mins, the order of removal is as follows: 12, 15, 18, 25 and 30 WO_3, 1c:1a, 1c:2a, 2c:1a and 4c:1a respectively while at maximum time of 240 mins the removal efficiency is 28, 47, 50, 80 and 90 % respectively. Hence, the overall removal efficiency of the photocatalyst clearly increased in the order of pure WO_3< 1c:1a < 1c:2a < 2c:1a < 4c:1a for both reactive dye and COD.As expected 4c:1a showed the best percentage removal while pure WO_3 showed the lowest percentage removal. This could be attributed to 4c:1a having the highest surface area as indicated in the BET plot above and also having the lowest band gap suppressed electron-hole recombination rate than others and hence enhanced higher photocatalysis. Similar findings were observed by Silveira *et al*., (2020) in which 15 % Mo doped WO_3 nanowires had the highest removal efficiency (38 %) compared to undoped WO_3 nanowires at 28 % efficiency. From table 4.6 below, it can be observed that the photocatalytic performance of the nanomaterials depends on the surface area, pore size, dopants used, reaction time, catalyst dosage and also the nature of pollutants. Thummavichai *et al*., (2021) did not co-dope the nanowires with non-metals like this study did; hence, the co-doped nanowires in this study performed a bit better. The high removal rate at a shorter time seen in Khanam and Rout (2022) could be as a result of the simulated solution used. Simulated solutions do not contain radical scavengers or suspended solids like the original environmental sample hence competition for active sites by the organic compounds will be limited. Comparison of the photocatalytic performance with previous studies and this study is shown in table 4.6 below.

Table 4.6: Comparison of the photocatalytic performance with previous studies and this study

Nanomaterials	Synthetic method	Photocatalytic conditions	Characterisation	Percentage degradation	Reference
Zn –WO_3 nanoparticles	Precipitation method	-UV/visible light -Reaction time :120 min -Dosage: 15mg	Zn-WO_3 was spherical, rod-shaped triclinic nanoparticles	92% removal	Arshad *et al*., (2019)
Gd-WO_3 nanorods	Hydrother-mal method	-Visible light -Dosage: 5mg -Reaction time: 120 min	- Rod like shaped nanorods -Crystallite size of 36-39nm	94% removal at 100 mins	Govindaraj *et al*., (2020)
P-WO_3 nanoparticles	Hydrotherma l method	-Visible light -Reaction time: 120 mins	Pure orthorhombic nanoparticles	96% removal of methylene blue	Sun *et al*., (2020)
Na-WO_3 Bronze nanowires	Solvother-mal method	-UV light/visible Dosage:0.01 mg	Block bundles of nanowires with varying lengths	90% removal	Thummavic hai *et al*., (2021)
Al/B-WO_3 nanoparticles	Wet impregnation method	-10mg/100cm^3 -Reaction time: 120 mins	-Agglomerated shaped of WO_3 nanoparticles -Band gap: 1.7eV -Surface area: 66.94 m^2/g	94% and 90% reduction of COD and TOC level	Tijani *et al*., (2021)
Ag/Mo_x-$W_{1-x}O_{3-y}$ heterostructures	Solvothermal -mal method	-Visible light -Dosage:10mg -Reaction time:100 mins	-Surface area: 20-26m^2/g -Pore size: 8-15nm	Degrading 90% Rhodamine blue and 98% Methylene blue at 40mins	Khanam and Rout (2022)
WO_3	Hydrotherma l method	-Natural sunlight -Dosage:0.2g -reaction time: 240mins	Monoclinic (2.7eV, 4.2m^2/g) Pore size: 15.4nm	60% removal	This study
2c:1a	Hydrotherma l method	-Natural sunlight -Dosage:0.2g -reaction time: 240mins	Monoclinic (2.3 eV, 16.03m^2/g) Pore size: 4.05nm	86% removal	This study
4c:1a	Hydrotherma l method	-Natural sunlight -Dosage:0.2g -reaction time: 240mins	Monoclinic (2.2 eV, 24.60m^2/g) Pore size: 3.60nm	93% removal	This study

4.2 Heavy Metal analysis in the Treated Wastewater

The heavy metal ion analysis of the wastewater revealed high amount of chromium, copper, nickel, lead, which were all above the permissible standard concentrations recommended by Nigerian Industrial Standard (NIS) and World Health Organization (NIS, 2015; WHO, 2017). The presence of these metals has been reported to cause various health issues such as respiratory issues, skin rashes, weak immune systems, chest pain and renal failure amongst others (Mood-Balali *et al*., 2021). As seen in the Table 4.7 below, the order of abundance of the metals is Cu > Cr > Pb > Ni.

Table 4.7: **Heavy Metal Concentration in Raw and Treated Wastewater Samples**

SAMPLE ID	Cr (ppm)	Cu (ppm)	Ni (ppm)	Pb (ppm)
Raw wastewater	1.64	1.76	1.15	1.26
WO_3	1.56	1.62	0.13	0.08
2c:1a	0.05	0.05	0.03	0.01
4c:1a	0.01	0.05	0.03	0.01
NIS(2015)	0.05	1.00	0.02	0.01
WHO(2017)	0.10	0.05	3.00	0.015

NIS: Nigerian Industrial Standard

WHO: World Health Organization

The concentration of Cu was seen to be the most abundant in the wastewater and was seen to be above the permissible limit. High concentration of Cu has been reported to impede the uptake of iron and germination of seed (Yaseen and Scholz, 2019). The concentration of Cr was seen to be greater than the WHO standard and that reported by both Tijani *et al*. (2021)

and Ajala *et al*. (2022) but lesser than that recorded by Uko *et al*. (2022). High concentration of metals like Cr, Pb and Ni are very harmful and toxic to man, aquatic lives because they can easily damage vital organs of humans and cause cancer (Ajiboye *et al*., 2021). The effect of contact time on the adsorption behavior of WO_3, 2c:1a and 4c:1a nanowires for the removal of the heavy metals from the dyeing wastewater was also investigated and varied between 0 and 120 min. The result obtained is shown in figure 4.19 (A-C).

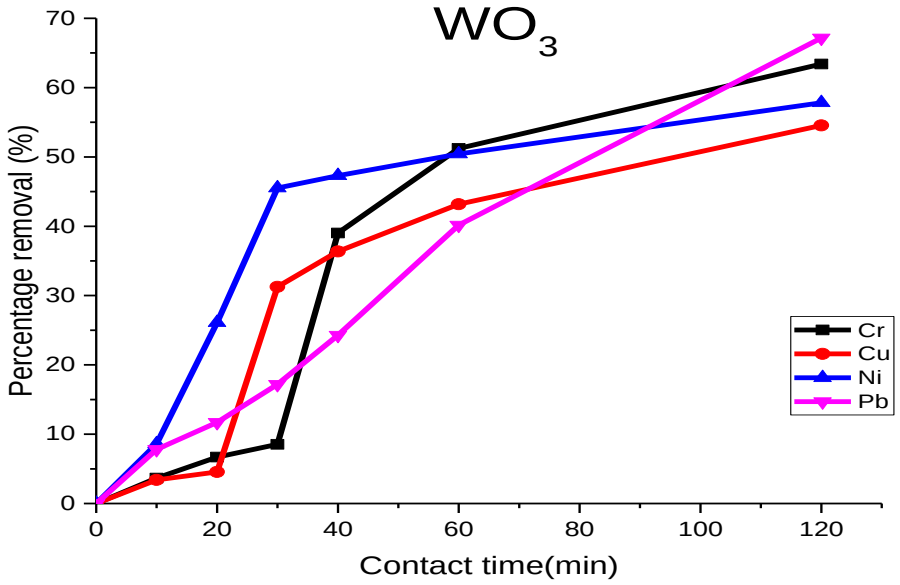

Figure 4.19A: Effect of contact time on the adsorption of metal ions by using undoped WO_3

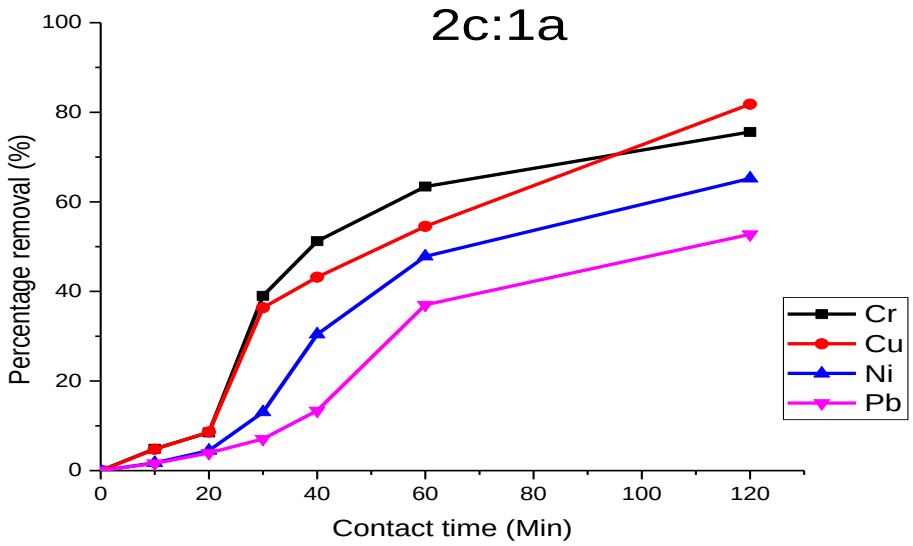

Figure 4.19B: Effect of contact time on the adsorption of metal ions using 2c:1a nanocatalyst

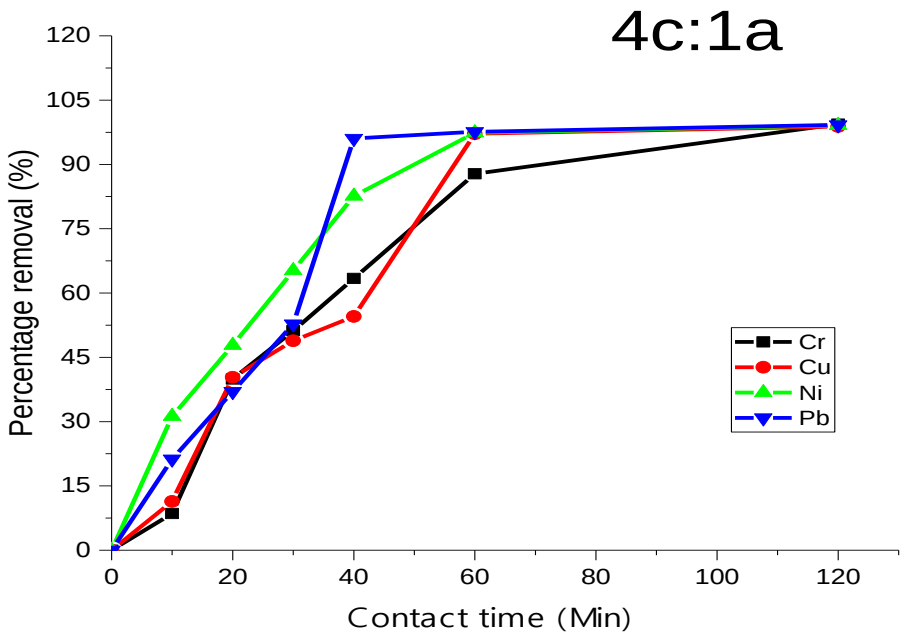

Figure 4.19C: Effect of contact time on the adsorption of metal ions using 4c:1a nanocatalyst.

It was observed that the removal efficiencies of the metals increased as the time increased for all three samples. The percentage removal of chromium onto WO_3, 2c; 1a and 4c:1a was `63.4, 75.6 and 99.4 % respectively at maximum time of 120 mins. The percentage removal of Cu onto WO_3, 2c;1a and 4c:1a was 54.55, 81.8 and 98.86 % respectively. Similar trend was also observed for Ni and Pb with the highest removal efficiency obtained with the use of 4c:1a. This variation could be attributed to the surface charge on the nano- catalyst (Ajala *et al*., 2022) and availability of vacant active sites on the surface of the nano-catalyst (Uko *et al*., 2022).

Furthermore, it was also noticed that the first 10-20 mins the removal efficiency was lower for WO_3 and 2c:1a compared to 4c:1a. This can be attributed to higher surface area of 4c:1a leading to more vacant sites for adsorption of the metal ions. In other words, more surface adsorption sites were present on 4c:1a at the first 10-20 min compared to 2c:1a and WO_3. The order of abundance of metals in the dyeing wastewater is Cu > Cr > Pb > Ni and the order of removal by each nanocatalyst at maximum time of 120 mins is as follows; WO_3: Cr > Ni > Cu > Pb, 2c:1a: Cu> Cr > Ni > Pb, 4c:1a: Cr > Cu > Ni >Pb. These variations may be attributed to the nature of ions in the aqueous media (Bankole *et al*., 2019) and the ionic radii of the metals (Ajala *et al*., 2022). This is because metals with smaller ionic radius tend to diffuse faster than those with large ionic radius. The degradation of the wastewater by photocatalyst (WO_3, 2c:1a and 4c:1a) significantly reduced the pollution parameters to fall within the threshold concentrations of the standards.

4.3 Kinetics Study

In the present study, zero, first- and second-order reaction kinetics were used to study the degradation kinetics of COD and reactive dye by the photocatalyst which could also help in gaining insight into the mechanism of the degradation process (Tomul *et al*., 2020). Using each photocatalyst namely; pure WO_3, 2c:1a and 4c:1a, the TOC kinetic data were fitted to the following kinetics and mechanism models: zero order, first-order and second-order kinetics and presented in Table 4.8 below.

Table 4.8: Kinetic Parameters for Reactive Dye Degradation as an Indicator Parameter from Dye Wastewater

Models	**Parameter**	**Photocatalysts**		
		WO_3	2c:1a	4c:1a
	$K_0(min^{-1})$	0.00574	0.00689	0.00646
Zeroth order	R^2	0.95515	0.85841	0.74320
	SSE	0.03903	0.19745	0.36319
	χ^2	0.00781	0.03949	0.07264
First order	K_1 (min^{-1})	0.00583	0.00998	0.01063
	R^2	0.98826	0.97079	0.93390
	SSE	0.01019	0.07547	0.20163
	χ^2	0.00204	0.01509	0.04033
Second order	$K_2(min^{-1})$	0.00633	0.01774	0.02297
	R^2	0.99170	0.99286	0.99920
	SSE	0.00845	0.05707	0.01066
	χ^2	0.00169	0.01141	0.00213

Based on the evaluated data presented in Table 4.7, correlation coefficient R^2 of second-order (> 0.99) and the rate constant (K_2) is highest among all the kinetics models explored. Error functions such as SSE and χ^2 were also used to adjudge the best suited model to kinetic data, and values closer to zero indicates a significant agreement between the experimental and theoretical values. The fitness follows the order of 4c:1a > 2c:1a > WO_3. This performance may be as a result of the difference in band gap and surface area of the photocatalyst. This suggests that the degradation process of reactive dye in the indigenous wastewater is based on the reactive species ($OH^{\cdot}$ and O_2). Looking at the rate constants, 4c:1a has the highest value, simply put the rate of degradation for 4c:1a is twice faster than WO_3 and approximately 1.5 times faster than 2c:1a while the rate of degradation for 2c:1a is approximately 1.4 times faster than WO_3.The difference in rate constant may be attributed to the abundance of the dopants, band gap energy and also the surface area of 4c:1a than other catalysts.

Generally, comparing the correlation coefficients (R^2), (SSE) and χ^2 obtained from Analysis. It can be seen that (R^2), (SSE) and (χ^2) based on the second- order reaction kinetics were 0.99920, 0.01066, and 0.00213 which were obviously much better than that of the zero-order (R^2 = 0.74320, SSE = 0.36319, and χ^2 = 0.07264) and the first-order (R^2 = 0.93390, SSE = 0.20163, and χ^2 = 0.04033) reaction kinetics for the 4c:1a photocatalyst. For the COD parameters, based on the R^2 and k values, the photodegradation of the dyeing wastewater by the photocatalyst also follow the second order kinetics than others. The kinetic parameter for COD is shown in table 4.9 below.

Table 4.9: Kinetic Parameters for (Chemical Oxygen Demand) COD Degradation as an Indicator Parameter from Dye Wastewater

Models	Parameter	Photocatalysts		
		WO_3	2c:1a	4c:1a
	$K_0(min^{-1})$	0.01072	0.01014	0.01000
Zeroth order	R^2	0.66800	0.55400	0.35640
	SSE	2.16157	2.75264	3.06301
	χ^2	0.43231	0.55053	0.61260
Pseudo-first order	K_1 (min^{-1})	0.01543	0.01601	0.01754
	R^2	0.88245	0.80441	0.76724
	SSE	0.79908	1.57114	2.35081
	χ^2	0.15982	0.31423	0.47016
Pseudo-second order	$K_2(min^{-1})$	0.04191	0.05742	0.08599
	R^2	0.99641	0.99716	0.99801
	SSE	0.15971	0.16568	0.53092
	χ^2	0.03194	0.03314	0.10618

The order of fitness of the kinetic models was as follows: Second order >first order> zero order. This suggests that the degradation of the reactive dye in the wastewater depends on one factor only. This could be either the catalyst dosage, intensity of the sunlight irradiation or the concentration of the reactive dyes. Similarly, like the reactive dye analysis, the rate of degradation for 4c:1a is 3 times faster than WO_3 and 1.3 times faster than 2c:1a, while the rate of degradation of 2c:1a is 2 times faster than WO_3.Similar trend was also observed for first order kinetics. Difference in rate constant was also observed, 4c:1a has the highest rate

constant. The high-rate constant suggests the formation of more oxygen vacancies which will further enhance high degradation efficiency. On the other hand, the R^2 values for first-order and zero order for all the photocatalysts (WO_3, 2c:1a and 4c:1a) showed that the kinetic data were not properly represented. The higher value of correlation coefficient from second order was an indication of a fast photodegradation process (Dada *et al*., 2019).

The choice of the best fit kinetic model was adjudged not only with correlation coefficient but also with the statistical error validity functions. It has been established that the model with a higher R^2 value, and lower data of statistical error function, would be chosen as the best descriptive model (Ojediran *et al.,* 2021). Hence, second-order fit perfectly well into this condition and thus the best kinetic model to describe the degradation of TOC and COD by the photocatalyst (WO_3, 2c:1a and 4c:1a), this claim is supported by the findings of Nekouei and Nekouei (2017).

4.4 Reaction Mechanism of the Enhanced WO_3 Photocatalyst

The enhanced photocatalytic behavior of Cl/Ca-WO_3 nanowires for the degradation of reactive dyes in the indigenous wastewater can be linked to the formation of the four reactive species that take part in the process. These species are O_2^-, $\cdot OH$, e^- and h^+. During photocatalytic reaction, the dyes in the wastewater is been adsorbed onto the surface of doped nanowires then excitation of the dye molecules follows. The electrons in the valence band of the pure WO_3 nanowires moved to the conduction band which leads to the creation of holes at the valence band. In the doped nanowires, the W^{6+} in the WO_3 lattice is been replaced by Ca^{2+} and then Cl^- creates some energy levels within the band thus lowering the band gap. In reduction of COD, the dopants promoted charge carrier separation efficiency and causing the

movement of Ca^{2+} to the surface of WO_3 leading to photoadsorption of O_2. Cl^- also improved the surface acidity of WO_3 and creation of more surface-active sites. The photogenerated electrons is been oxidized to form O_2^- while holes react with water molecules to form $\cdot OH$ radicals. Because of the oxidizing ability of both O_2^- and $\cdot OH$ radicals, they react with the dye molecules and degrade it to produce CO_2 and H_2O as intermediates. Overall, the band gap of WO_3 is reduced by the introduction of the dopants Ca^{2+} and Cl^- by capturing electrons during photocatalysis and suppressing the recombination of e^-/h^+ pair. The reaction mechanism for the degradation of the dye by the doped WO_3 nanowires is presented as follows:

$$Cl\text{-}Ca\text{-}WO_3 + hv \longrightarrow eCB^- + hVB^+ \quad (4.1)$$

$$hVB^+ + H_2O \longrightarrow OH + H^+ \quad (4.2)$$

$$eCB^- + O_2O_2^- \longrightarrow O_2^{\cdot -} \quad (4.3)$$

$$\cdot OH + dyes \longrightarrow H_2O + CO_2 \quad (4.4)$$

$$O_2^- + dyes \longrightarrow H_2O + CO_2 \quad (4.5)$$

4.5 Reusability/Stability Studies

4.5.1. XRD analysis after photo-degradation

The stability or reusability of a photocatalyst is very important in their application for environmental remediation. Therefore, the XRD crystallographic pattern of 4c-1a before and

after the photocatalytic experiment was carried out to evaluate its reusability after five cycles for TOC removal. When each recycling experiment finished, the mixture was filtered and the residue (catalyst) was washed with deionized water for 30 mins and calcined at 550°C for 2h and then examined using XRD to check for the mineralogical phase. The XRD pattern of the used nanocatalyst is shown in Figure 4.20.

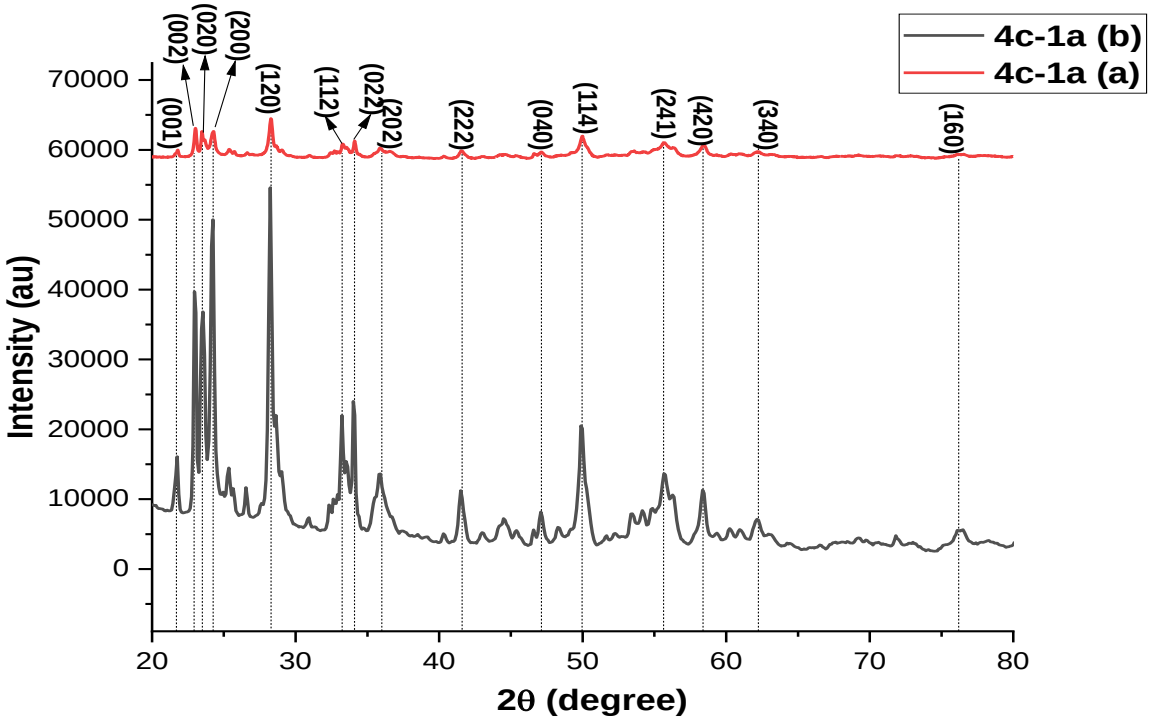

Figure 4.20: XRD pattern of the 4c-1a (a) before and 4c-1a (b) after the photocatalytic degradation of wastewater.

It is obvious that there were neither clearly no remarkable changes nor presence of additional crystallographic peaks. The morphology and mineralogical phase did not also change, however improved peak intensity in the 4c-1a after the photocatalytic experiment could be attributed to additional calcination for two hours after the reaction. This demonstrated that the original crystalline structure of 4c-1a was preserved and could be responsible for its

photocatalytic performance. Figure 4.21 also show the re-usability cycle of 4c:1a for dyeing waste water treatment for five cycles.

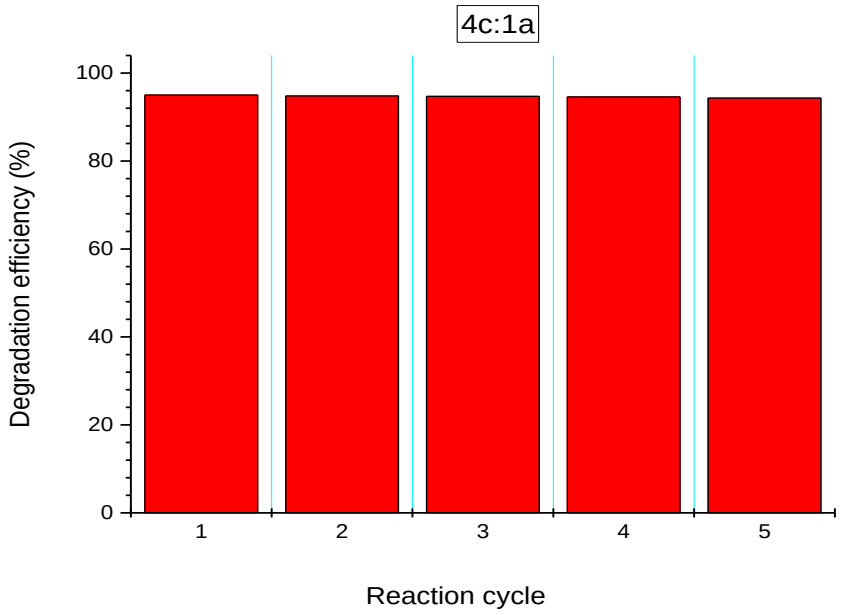

Figure 4.21: Reusability tests of 4c:1a nanowires after five cycles

It was observed that the degradation efficiency of reactive dye was 95%, 94% and 93% for the 1st, 2nd and 3rd cycles respectively. However, as the number of cycles increases to the fifth, the degradation efficiency also reduced but did not fall below 90%, this suggests thenumber of active sites for adsorption of the pollutants were still intact.

CHAPTER FIVE

Conclusion and Recommendations

5.1 Conclusion

This chapter provides the summary of the important findings and conclusions of the various results presented in chapter four. Recommendations on areas for future research are equally provided. Undoped WO_3 and Cl-Ca co-doped nanowires were successfully prepared via hydrothermal method at different conditions. The UV spectrum for the undoped nanowires showed that they were all in the UV region whilst that of the co-doped nanowires indicated a shift to the visible region as a result of the introduction of dopants into the lattice of WO_3. As the amounts of dopants increased, the band gap energy also decreased from 2.7 eV for undoped WO_3 to 2.2eV for 4c:1a.

XRD pattern of the undoped nanowires can be indexed to the WO_3 monoclinic structure for conditions A and B while for condition C the peaks can be indexed to the WO_3 triclinic structure. The average crystalline size of the nanowires was found to be 14.83nm, 14.93nm and 14.39nm for conditions A, B and C respectively. For the co-doped samples (1c-1a-WO_3, 1c-2a-WO_3, 1c-4a-WO_3, 2c-1a-WO_3 and 4c-1a-WO_3) the XRD also showed that they all belong to the same monoclinic phase of WO_3. However, the peak positions were shifted to a lower angle. This can be attributed to an increase in lattice parameter which further confirms the intercalation of different Ca and Cl contents into the WO_3 layers of the nanowires.

HRSEM images of the undoped samples consist of a mixture of agglomerated spherical nanoparticles and bamboo like- nanowires of different sizes and aspect ratios while that of co-doped samples showed the formation of stacked and block bundles of nanowires with

varying lengths and diameters. In general, the produced block bundles of Cl-Ca-WO_3 nanocomposite samples were longer and wider in diameter (100 – 400 nm) than those of the pure WO_3 nanowires (100 -250 nm) due to the addition of the two dopants.

EDS analyses showed that only oxygen, tungsten were present in the undoped nanowires. No other impurity was present. For the co-doped samples oxygen and tungsten appeared as the dominant elements while the dopants appeared in proportionate amounts.

The HRTEM images of the undoped nanowires showed the capping of oxalic acid on the surface of W assisting the growth of the nanowires. Some secondary branches with random length and diameter were observed on the surface of the doped nanowires. These branches also increased as the amount of each of the dopants is doubled which is supported by the SEM result. (SAED) pattern of the undoped and Cl-Ca doped WO_3 nanowires indicates that all the samples exhibited diffraction rings, Also, it was observed that increase in the dopants influenced the growing patterns of the nanowires as a result of the interaction between the dopants and thus making the samples to have diffraction rings. BET results revealed an increase in surface area of the samples in the order of 4c:1a> 2c:1a> pure WO_3 such as 24.602 > 16.031 > 4.216 m^2/g respectively.

The photocatalytic activity of the samples showed that the removal efficiency of the photocatalyst clearly increased in the order of pure WO_3< 1c:1a < 1c:2a < 2c:1a < 4c:1a for both reactive dye and COD. The order of abundance of metals in the dyeing wastewater is Cu > Cr > Pb > Ni and the order of removal by each nanocatalyst at maximum time of 120 is as follows; WO_3: Cr > Ni > Cu > Pb, 2c:1a: Cu > Cr > Ni > Pb, 4c:1a: Cr > Cu > Ni > Pb.

The kinetics showed that Pseudo second-order fit perfectly well and thus the best kinetic model to describe the degradation of TOC and COD by the photocatalyst (WO_3, 2c:1a and 4c:1a)

5.2 Recommendations

The following are the recommendation for further studies:

- The antioxidant and antibacterial behavior of the nanowires should also be studied
- The electrochemical and optical nature of the nanowires should also be considered.
- Green synthesis (use of plant extracts) of WO_3 nanowires and its photocatalytic activity should be considered
- The particle size of the nanowires should be varied and their photocatalytic activity studied individually.
- Other methods of synthesizing WO_3 nanowires aside hydrothermal method should be employed and its photocatalytic activity on removal of wastewater should be tested. Also, other application of WO_3 nanowires such as gas sensing should be investigated. Metal doped WO_3 nanowires and non – metal doped WO_3 nanowires should be synthesized and their photocatalytic activity compared so as to know which one has better removal efficiency.

5.3 Contribution to Knowledge

In this study, pure WO_3 and Cl-Ca-WO_3 co-doped nanowires were synthesized using hydrothermal method. Response surface methodology (RSM) optimization based on box Behnken design was employed for the hydrothermal synthesis. Sodium tungstate dihydrate

and oxalic acid were used as precursor salt and stabilizer respectively while Sodium chloride and Calcium nitrate acted as dopants for Cl and Ca respectively.

The synthesized nanowires were characterised further using analytical methods like UV-Visible spectroscopy, HRSEM, EDS, HRTEM, XRD and BET for their absorption band, morphological phases, elemental composition and surface area respectively. The pure WO_3 nanowires absorbed light at the UV region at a wavelength of 280nm while the co doped nanowires absorbed light at the visible region of the spectrum at a wavelength of 600 nm, there was also a reduction in the band gap for the co doped samples from 2.7 ev – 2.2 ev. HRSEM results showed that the synthesized nanowires were monoclinic with diameter ranging between 104.5 nm – 125 nm. BET analysis showed an increase in surface area from 4.216 m^2/g to 16.031 m^2/g**.** The photocatalytic activity of the synthesized nanowires for the degradation of reactive dye under sunlight was also studied.

The physico-chemical characterisation of the Indigenous dyeing wastewater was also determined. It was observed that the pH of the dyeing wastewater after degradation reduced from 12.28 to 10, electrical conductivity reduced from 42.4 µS/cm to 39.60 µS/cm when the codoped sample was used. COD, BOD, TOC reduced significantly from 1073 mg/l to 80 mg/l, 245 mg/l to 10.20 mg/l, 150 mg/l to 0.05 mg/l respectively.

The degradation efficiency of the reactive dye in the dyeing wastewater was 35, 55, 60, 90, & 94 for WO_3, 1c:1a, 1c:2a, 2c:1a & 4c:1a respectively at contact time of 240 min while the percentage Chemical Oxygen Demand (COD) removal was 28, 47, 50, 80, and 90 for WO_3, 1c:1a, 1c:2a, 2c:1a & 4c:1a respectively.

REFERENCES

Abidemi, B.L., James, O.A., Oluwatosin, A.T., Akinroopo, O.J., Oraeloka, U. D., & Racheal, A.E.(2019). Treatment technologies for wastewater from cosmetic industry- A Review.*International Journal of Chemical and Bimolecular Science,* 4(4), 69-80.

Ahmadian, H., Tehrani, F. S., & Aliannezhadi, M. (2019). Hydrothermal synthesis and characterization of WO_3 nanostructures: effects of capping agent and pH. *Materials Research Express,* 6(10), 105024. doi:10.1088/2053-1591/ab3826.

Ajala, M. A., Abdulkarareem, A.S., Tijani, J.O., & Kovo, A.S. (2022). Adsorptive behavior of rutile phased titania nanoparticles supported on acid-modified kaolinite clay for the removal of selected heavy metal ions from mining wastewater. *Applied Water Science,* doi.org/10.1007/s/3201-021-01561-8.

Ajiboye, T. O., Oyewo, O. A., & Onwudiwe, D. C. (2021). Simultaneous removal of organics and heavy metals from industrial wastewater: A review. *Chemosphere,* 262, 128379.doi: 10.1016/j.chemosphere.2020.128379

Arshad, M., Ehtisham-ul-Haque, S., Bilal, M., Ahmad, N., Ahmad, A., Abbas, M., Nisar, J., Khan, M.I., Nazir, A., Ghaffar, A., & Iqbal, M. (2019). Synthesis and characterization of Zn doped WO_3 nanoparticles; Photocatalytic, antifungal and antibacterial activities evaluation. *Material Research Express,* doi.org/10.1088/2053-1591/ab6380.

Arvisdea, C.E., Gustiawan, K.H., Ramadhanty, L., Ainin, N.N., Sari, S.W., Rahmanin, T., & Nandiyato, A.B.D (2021). Review: Synthesis of nanoparticles and nanocomposites of WO_3. *Maghrebian Journal of Pure and Applied Science,* 7(1), 15-30.

Amigun, A.T., Adekola, F. A., Tijani, J. O., & Mustapha, S. (2022). Photocatalytic degradation of malachite green dye using nitrogen/sodium/iron-TiO_2 nanocatalysts. *Results in Chemistry,* doi-org/10.1016/j.rechem.2022.100480.

Azam, K., Akhtar, S., Gong, Y. Y., Routledge, M. N., Ismail, A., Oliveira, C. A. F., & Ali, H. (2021). Evaluation of the impact of activated carbon-based filtration system on the concentration of aflatoxins and selected heavy metals in roasted coffee. *Food Control*, 107583.doi:10.1016/j.foodcont.2020.107.

Baba, A., Garba, S.T., Kolo, B.,& Bello, H.S. (2020). Bioremediation of Effluents Samples from Textile Industry in Kano State, Nigeria. *Chemistry Research Journal*, 5(1), 56-70.

Bankole, M.T., Abdulkareem, A.S., Mohammed, I.A., Ochigbo, S.S, Tijani, J.O., Abubakre, O.K.,&Roos, W.D. (2019). Selected heavy metals removal from electroplating wastewater by purified and polyhydroxylbutyrate functionalized carbon nanotubes adsorbents. *Scientific Reports*, 9 (4475), doi.org/10.1038/s41598-018-37899-4.

Bayan, E. M., Lupeiko, T. G., Kolupaeva, E. V., Pustovaya, L. E., & Fedorenko, A. G. (2017).Fluorine-doped titanium dioxide: synthesis, structure, morphology, size and photocatalytic activity. *Advanced Materials*, 17–24. doi:10.1007/978-319560625_2.

Behzadi, S., Nonahal, B., Royaee, S. J., &Asadi, A. A. (2020). $TiO_2/SiO_2/Fe_3O_4$ magnetic nanoparticles synthesis and application in methyl orange UV photocatalytic removal. *Water Science and Technology*. doi:10.2166/wst.2020.509.

Belver, C., Bedia, J., Gómez-Aviles, A., Peñas-Garzón, M., & Rodriguez, J. J. (2019). Semiconductor Photocatalysis for Water Purification. Nanoscale Materials in Water Purification, 581–651. 10.1016/b978-0-12-813926-4.00028-8.

Cao, D. Q., Wang, X., Wang, Q. H., Fang, X. M., Jin, J.Y., Hao, X., Di, Iritani, E., & Katagiri, N. (2020). Removal of heavy metal ions by ultrafiltration with recovery of extracellular polymer substances from excess sludge. *Journal of Membrane Science*, 606, (118103) doi.org/10.1016/j.memsci.2020.118103.

Chen, P. R., Fu, H.W., Yang, S.M., &Lu, K.C. (2022). Chemical vapor deposition-fabricated manganese-doped and potassium-doped hexagonal tungsten trioxide nanowires withenhanced gas sensing and photocatalytic properties. *Nanomaterials,* 12,doi.org/10.3390/nano12071208.

Dada, A. O., Adekola, F. A., Odebunmi, E. O., Inyinbor, A. A., Akinyemi, B. A., & Adesewa, I., D. (2019). Kinetics and thermodynamics of adsorption of rhodamine b onto bentonite supported nanoscale zerovalent iron nanocomposite. *Journal of Physics: Conference Series,* 1299, 012106. doi:10.1088/1742-6596/1299/1/012106.

Dande, R., Bayero, A.S., & Koki,I.B. (2019). Determination of heavy metals in an industrial wastewater using atomic absorption spectrophotometer. *Proceedings*, 539-541.

Das, A., & Nair, R. G. (2019). Effect of aspect ratio on photocatalytic performance of hexagonal ZnO nanorods. *Journal of Alloys and Compounds*, 153277.doi: 10.1016/j.jallcom.2019.153277.

Dufantanye, I., Lee, Y., Kim, H.,& Lee, S. (2022) Industrial wastewater discharge and compliance investigation for environmentally resilient Rwanda. *Water*, 14, 3100. https://doi.org/10.3390/w14193100.

Durotoye, T. O., Adeyemi, A. A., Omole, D. O., & Onakunle, O. (2018). Impact assessment of wastewater discharge from a textile industry in Lagos, Nigeria. *Cogent Engineering*, 5(1), 1–11. doi:10.1080/23311916.2018.15316.

Dutta, S., Gupta, B., Srivastava, Suneel K., & Gupta, A. K. (2021). Recent advances on the removal of dyes from wastewater using various adsorbents: A critical review. *Materials Advances.* doi:10.1039/d1ma00354b.

El-Yazeed, W. S. A., Eladl, M., Ahmed, A. I., & Ibrahim, A. A. (2020). Fluorine-doped tin oxide as efficient solid acid catalyst: acidity and the catalytic activity relationship. *Journal of Sol-Gel Science and Technology*. doi:10.1007/s10971-020-05422-9.

Florescu, D., Ioadache, A.M., Costinel, D., Horj, E., Ionete, R. E.,&Culca, M. (2013). Validation procedure for assessing the total organic carbon in water samples.*Romanian Journal of Physics* 58, (1-2), 211–219.

Fu, L., Cai, W., Wang, A.,& Zheng, Y. (2014) Photocatalytic hydrogenation of nitrobenzene to aniline over tungsten oxide-silver nanowires. *Materials Letters* 142 (2015), 201–203.

Genchi, G., Carocci, A., Lauria, G., Sinicropi, M.S., & Catalano, A. (2020). Nickel: Human health and environmental toxicology. *International Journal of Environmental Research and Public Health*, 17(3), 679.

Govindaraj, T., Mahendran, C., Marnadu, R., Shkir, M., & Manikandan, V. S. (2020). The remarkably enhanced visible-light-photocatalytic activity of hydrothermally synthesized WO_3nanorods: An effect of Gd doping. *Ceramics International*. doi: 10.1016/j.ceramint.2020.10.004.

Gurkan, Y., Kasapbasi, E., Turkten, N., & Cinar, Z. (2017). Influence of Se/N co-doping on the structural, optical, electronic and photocatalytic properties of TiO_2. *Molecules*, 22(3), 414. doi:10.3390/molecules22030414.

Guo, X., Qin, X., Xue, Z., Zhang, C., Sun, X., Hou, J.,& Wang, T. (2016). Morphology-controlled synthesis of $WO_{2.72}$ nanostructures and their photocatalytic properties. *RSC Advances*, 6, 48537 DOI: 10.1039/c6ra08551b.

Han, F., Li, H., Fu, L., Yang, J.,& Liu, Z. (2016). Synthesis of S-doped WO_3 nanowires with enhanced photocatalytic performance towards dye degradation. *Chemical Physics Letters*, 183-187 http://dx.doi.org/10.1016/j.cplett.2016.03.017

Havancsak, K. (2017). High-resolution scanning electron microscopy. Retrieved www.technoorg.hu/news-and-events.

Hu, X., Xu, P., Gong, H., & Yin, G. (2018). Synthesis and characterization of WO_3/Graphene nanocomposites for enhanced photocatalytic activities by one-step *in-situ* hydrothermal reaction. *Materials*, 11(1), 147. doi:10.3390/ma11010147.

Ibrahim, Y., Naddeo, V., Banat, F., & Hasan, S. W. (2020). Preparation of novel polyvinylidene fluoride (PVDF)-Tin(IV) Oxide (SnO_2) ion exchange mixed matrix membranes for the removal of heavy metals from aqueous solutions. *Separation and PurificationTechnology*, 117250.doi: 10.1016/j.seppur.2020.117250.

Imtiaz, F., Rashid, J., & Xu, M. (2019). Semiconductor nanocomposites for visible light photocatalysis of water pollutants. *Concepts of Semiconductor Photocatalysis*. doi:10.5772/intechopen.86542.

Jamjourn, H. A. A., Umar, K., Adnan, R., Razali, R. M.,& Ibrahim, M. N. M. (2021). Synthesis, characterization and photocatalytic activities of graphene oxide/metal oxides nanocomposites: A Review. *Frontiers in Chemistry*, 9, (752276), doi:10.3389/fchem.2021.752276.

Kahng, S., Yoo, H.,& Kim, J.H. (2019). Recent advances in earth abundant photocatalyst materials for solar H_2 production. *Advanced Powder Technology*, https://doi.org/10.1016/j.apt.2019.08.035

Khanam, S.,& Rout, S. K. (2022). Synergetic effect of silver molybdenum tungsten oxide heterostructures for enhanced photocatalytic reaction. *Chemical Physics Impact*. Doi.org/10.1016/j.chphi.2022.100093.

Koe, W. S., Lee, J. W., Chong, W. C., Pang, Y. L., & Sim, L. C. (2019). An overview of photocatalytic degradation: photocatalysts, mechanisms, and development of photocatalytic membrane. *Environmental Science and Pollution Research.* doi:10.1007/s11356-019-07193-5.

Kong, L., Guo, X., Xu, J., Mo, Z., & Li, L. (2020). Morphology control of WO_3 nanoplate film on W foil by oxalic acid for photocatalytic gaseous acetaldehyde degradation. *Journal of Photochemistry and Photobiology A: Chemistry*, 401,112760 https://doi.org/10.1016/j.jphotochem.2020.112760

Kumar, G. S., & Rao, K. S. R. (2015). Tungsten-based nanomaterials ($WO_3$and Bi_2WO_6):Modifications related to charge carrier transfer mechanisms and photocatalytic applications. *Applied Surface Science, 355, 939–958.*doi: 10.1016/j.apsusc.2015.07.00.

Kyrii, S., Dontsova, T., Kosogina, I., Astrelin, I., Klymenko, N., &Nechyporuk, D. (2020).Local Wastewater Treatment by Effective Coagulants Based on Wastes. *Journal of Ecological Engineering*, 21 (5), 34-41.

Lee, S., Kim, J., Lee, J., Song, H., Lee, S., Choi, K., & Shin, G. (2014). Facile fabrication of high-efficiency near-infrared absorption film with tungsten bronze nanoparticle dense layer. *Nanoscale Research Letters*, 9(1), 294. doi:10.1186/1556-276x-9-294.

Leng, J., Wang, Z., Wang, J., Wu, H-H, Li, Y-X., Guo, H., Liu, Y., Zhang, Q., & Guo, Z. (2019). Advances in nanostructures fabricated via spray pyrolysis and their applications in energy storage and conversion. *Chemical Society Reviews,* 48 (3015). DOI: 10.1039/c8cs00904j.

Lellis, B., Fávaro-Polonio, C. Z., Pamphile, J. A., & Polonio, J. C. (2019). Effects of textiledyes on health and the environment and bioremediation potential of living

organisms. *Biotechnology Research and Innovation*.doi: 10.1016/j.biori.2019.09.001.

Li, D., Song, H., Meng, X., Shen, T., Sun, J., Han, W., & Wang, X. (2020). Effects of particlesize on the structure and photocatalytic performance by alkali-treated TiO_2. *Nanomaterials,* 10(3), 546. doi:10.3390/nano10030546.

Lin, P.C., Stephen, L., Wang, P.C. and Sridhar, R. (2013). Techniques for physicochemical characterization of nanomaterials. *Howard University Biotechnology Advance Journal*, 10 (1): 6-18.

Liu, G., Wang, S., Nie, Y., Sun, X., Zhang, Y., & Tang, Y. (2013). Electrostatic-induced synthesis of tungsten bronze nanostructures with excellent photo-to-thermal conversion behavior. *Journal of Material Chemistry*,1, pp. 10120–10129. doi: 10.1039/c3ta11479a.

Lu, H., Zhu, Q., Zhang, M., Yan, Y., Liu, Y., Li, M., Yang, Z.,& Geng P (2018) Synthesis of hexagonal ultrathin Tungsten oxide nanowires with diameters below 5nm for enhanced photocatalytic performance. *Superlattices and Microstructure.* DOI: 10.1016/j.spmi.2018.01.032.

Ma, B., Huang, E., Wu, G., Dai, W., Guan, N., and Li, L. (2017). Fabrication of $WO_{2.72}$/RGO nano-composites for enhanced photocatalysis. *Royal Society of Chemistry Advances*, 7, 2606–2614. doi:10.1039/C6RA26416F

Madare, C. C.,& Hassel, W. A (2019). Review on the versatility of tungsten oxide coatings. *Physica Status Solidi*, 21(6), 1-16. Doi:10.1002/pssa.201900047.

Maleki, A., Moradi, F., Shahmoradi, B., Rezaee, R., & Lee, S.-M. (2019). The photocatalytic removal of diazinon from aqueous solutions using tungsten oxide doped zinc oxide nanoparticles immobilized on glass substrate. *Journal of Molecular Liquids,* 111918.doi: 10.1016/j.molliq.2019.111918.

Mamba, G., & Mishra, A. K. (2016). Graphitic carbon nitride ($g\text{-}C_3N_4$) nanocomposites: A new and exciting generation of visible light driven photocatalysts for environmental pollution remediation. *Applied Catalysis B: Environmental*, 198, 347–377.

Maslova, M., Ivanenko, V., Yanicheva, N., & Gerasimova, L. (2020). The effect of heavy metalions hydration on their sorption by a mesoporous titanium phosphate ion exchanger. *Journal of Water Process Engineering,* 35, *(*101233).doi: 10.1016/j.jwpe.2020.101233.

Michel, M.M., Tytkowska, M., Reczek, L., Trach, Y., & Siwiec, T. (2019). Technological conditions for the coagulation of wastewater from cosmetic industry. *Journal of Ecological Engineering*, 20(5), 78-85.

Min, K. J., Kim, J. H., & Park, K. Y. (2021). Characteristics of heavy metal separation and determination of limiting current density in a pilot-scale electrodialysis process for plating wastewater treatment. *Science of the Total Environment*, 757, 143762.doi: 10.1016/j.scitotenv.2020.143762.

Mohammed, F.A., Ali, B.M., Nageib, R.M., & Elshaikh, H.A. (2020). Synthesis and characterizationof nanostructured tungsten trioxide (WO_3) thin films. *Aswan University Journal of Environmental studies(AUJES)*, 1 (1), 49-56.

Mood-Balali, M., Naseri, K., Tahergorabi, Z., Khazdair, M.R., & Sadeghi, M. (2021). Toxic mechanisms of five heavy metals: mercury, lead, chromium, cadmium and arsenic. *Frontiers in pharmacology*, 12, 643972, doi: 10.3389/fphar.2021.643972.

Mohagheghian, A., Ayagh, K., Godini, K., & Shirzad-Siboni, M. (2017). Using amino-functionalized Fe_3O_4-WO_3 nanoparticles for diazinon removal from synthetic and real water samples in presence of UV irradiation. *Journal of Advanced Oxidation Technologies*, 20(2). doi:10.1515/jaots-2016-0153.

Muszyński, A., Marcinowski, P., Maksymiec, J., Beskowska, K., Kalwarczyk, E., & Bogacki, J. (2019). Cosmetic wastewater treatment with combined light/FeO/H_2O_2 process coupled with activated sludge. *Journal of Hazardous Materials*.doi: 10.1016/j.jhazmat.2019.06.009.

Nagyne-Kovacs, T., Lukacs, I.E., Szabo, A., Hernadi, K., Igricz, T., Laszlo, K., Szilagyi, I. M., & Pokol, G. (2019). Effect of pH in the hydrothermal preparation of monoclinic tungsten oxide. *Journal of Solid-State Chemistry*, 281, (121044), 1–7. https://doi.org/10.1016/j.jssc.2019.121044

Navarro, J. R. G., Mayence, A., Andrade, J., Oleynikov, P., Parola, S., & Pawlicka, A. (2014). WO_3 nanorods created by self-assembly of highly crystalline nanowires under hydrothermal conditions, *Langmuir*, 1–6.

Navin, P.K., Kumar, S., Mathur, M. (2018). Textile Wastewater treatment: A critical review. *International Journal of Engineering Research and Technology*, 6 (11), 1-6.

Nekouei, F., & Nekouei, S. (2017). Comparative evaluation of BiOCl–NPls–AC composite performance for methylene blue dye removal from solution in the presence/absence of UV irradiation: Kinetic and isotherm studies. *Journal of Alloys and Compounds*, 701, 950–966. https://doi.org/10.1016/j.jallcom.2017.01.157.

Nkansah, M.A., Opoku, F., Ephraim, J.H., Wemegah, D.D., & Tetteh, L.P.M (2016). Characterization of beauty salon wastewater from Kwame Nkurumah University of Science and Technology, Kumasi Ghana, and its surrounding communities. *Environmental Health Insights*, 10, 147-154, doi:10.4137/EHI.S40360.

Nigerian Industrial Standard (NIS). Nigerian Standard for Drinking Water Quality. (2015).https://africacheck.org/wp-content/uploads/2018/06/Nigerian-Standard-for-Drinking-WaterQuality-NIS-554-2015.pdf

Ofori, F. A., Sheikh, F. A., Appiah-Ntiamoah, R., Yang, X., and Kim, H. (2015). A simple method of electrospun tungsten trioxide nanofibers with enhanced visible-light photocatalytic activity. *Nano-Micro Letters*, 7(3), 291–297. doi:10.1007/s40820-015-0042-8.

Ojediran, J. O., Dada, A. O., Aniyi, S. O., David, R. O., & Adewumi, A. D. (2021). Mechanism and isotherm modeling of effective adsorption of malachite green as endocrine disruptive dye using acid functionalized maize. *Scientific Reports*, 1–15. https://doi.org/10.1038/s41598-021-00993-1.

Pal Singh, J., Kumar, M., Sharma, A., Pandey, G., Chae, K. H., & Lee, S. (2020). Bottom-up and top-down approaches for MgO. Sonochemical Reactions.doi:10.5772/intechopen.91182.

Patra, J. K., & Back K. H. (2014). Green nanobiotechnology: factors affecting synthesis and characterization techniques. *Journal of Nanomaterial*, 2014(1), 125-138.

Pauekphong, K., Kooptarnond, K., Khangkhamano, M., Sikong, L., & Masae, M. (2019). Synthesis of WO_3/TiO_2 (B) nanowires by hydrothermal method. *Digest Journal of Nanomaterials and Biostructures*, 4(4), 1123-1130.

Pensupa, N., Leu, S.Y., Hu, Y., Du, C., Liu, H., Jing, H., Wang, H., & Lin, C.S.K (2017). Recent trends in sustainable situation and future prospects. *Topics in Current Chemistry*, 375, (76), Doi: 10.1007/s41061-017-0165-0.

Phuruangrat, A., Ham, J. D., Hong, J.S., Thongtem, S.,& Lee, J.S. (2010). Synthesis of hexagonal WO_3 nanowires by microwave-assisted hydrothermal method and their electrocatalytic activities for hydrogen evolution reaction *Journal of Material Chemistry*,20, 1683–1690.

Pradana, H. Y., Joni, I. M., Men, L. K., Yuliah, Y., Nulhakim, L., Muthukanan, V., & Panatarani, C. (2018). Synthesis and characterization of ZnO: Ca^{2+} prepared by simple solution method. doi:10.1063/1.5021231.

Pona, H. T., Xiaoli, D., Ayantobo, O. O., & Narh, D. T. (2021). Environmental health situation in Nigeria: current status and future needs. *Heliyon*, 7(3),doi: 10.1016/j.heliyon. 2021.e06330.

Razali, M.N. A., Wan Salleh, W. N., Aziz, F., Jye, L. W., Yusof, N., & Ismail, A. F. (2021). Review on tungsten trioxide as a photocatalysts for degradation of recalcitrant pollutants. *Journal of Cleaner Production*, 309, 127438.doi: 10.1016/j.jclepro.2021.12743.

Saritha, B., & Chockalingam, M. P. (2019). Evaluation and characterization of tannery wastewater. *International Journal of Pure and Applied Mathematics*, 119 (12), 8479-848

Shen, K., Sheng, K., Wang, Z., Zheng, J., & Xu, C. (2019). Cobalt ions doped tungsten oxide nanowires achieved vertically aligned nanostructure with enhanced electrochromic properties. *Applied Surface Science,* 144003.doi: 10.1016/j.apsusc.2019.14400.

Shewa W. A, Gunasekar V., Ponnusami V.,& Lalma J.A. (2016). Photocatalytic degradation of textile dye wastewater using green synthesized Ag/ZnO nano-composites catalyst under solar radiation. *International Journal of Chemical Science*, 14 (1), 313-320.

Silveria, J.V., Moreas, E.C., Moura, B. V. J., Sennna, C. A., Archango, B. S., Vascncelos, T. L., Filho A. G., Freire, P. T.,& Luz-lima, C. (2020). Mo-doped WO_3 nanowires for adsorbing methylene blue dye from wastewater. *Journal Of Material Science*, 55, 6429,6440. https://doi.org/10.1007/s10853-020-04472-2t

Sivakarthik, P., Thangaras, V., Perumal, K., & Balasi, S. (2016). Synthesis of co-dothdtin oxide Nanoparticles for Photocalytic degradation of synthetic organic dyes. *Digest Journal of Nanomaterial and Biostructures,* 11 (3), 934 – 943.

Sivakumar, M., & Dasgupta, A. (2019). Selected Area Electron Diffraction, a technique for determination of crystallographic texture in nanocrystalline powder particle of Alloy 617ODS and comparison with precession electron diffraction. *Journal of Materials Characterization,* 157 (109883), doi.org/10.1016/j.matchar.2019.109883.

Sotomayor, F.J., Cychosz, K.A.& Thommes, M. (2018). Characterization of micro/mesoporousmaterials by physiosorption: concepts and case studies. *Accounts of Materials by SurfaceResearch*, 3 (2), 34-50

Sun, J., Li, B., Wang, Q., Zhang, P., Zhang, Y., Gao, L., & Li, X. (2020). Preparation of Phosphorus –doped tungsten triode nanomaterials and their photocatalytic performances, Environmental Technology, Doi: 10.1080/09593330.2020.1745292.

Suwarnkar, M.B., Dhabbe, R.S., Kadam, A.N., & Garadkar, K.M. (2014). Enhanced photocatalytic activity of Ag doped TiO_2nanoparticles synthesized by a microwave assisted method. *Journal Ceramics International*, 40, 5489-5496.

Talebi, S., Chaibakhsh, N., &Moradi-Shoeili, Z. (2017). Application of nanoscale ZnS/TiO_2 composite for optimized photocatalytic decolorization of a textile dye. *Journal of Applied Research and Technology,* 15(4), 378–385.doi: 10.1016/j.jart.2017.03.007.

Tehrani, F. S., Ahmadian, H.,&Aliannezhadi, M. (2020). Hydrothermal synthesis and characterization of WO_3 nanostructures: Effect of reaction time. *Material Research Express*, 7 (015911) https://doi.org/10.1088/2053-1591/ab66fc

Thummavichai, K., Thi, L. A., Pung, S. Y., Ola, O., Hussain, M. Z., Chen, Y., Xu, F., Chen, W., Wang, N., & Zhu, Y. (2021). Sodium tungsten oxide bronze nanowires bundles in adsorption on of methylene blue dye under uv and visible light exposure. *Energies*, *14* (1322), 5,https://doi.org/10.3390/en14051322

Tijani, J.O., Abdullahi, M.N., Bankole, M.T., Mustapha, S., Egbosuba, T.C., Ndamitso, M.M.,Abdulkareem, A.S.,& Muzenda, E. (2021). Photocatalytic and toxicity evaluation of local dyeing wastewater by aluminum/boron doped WO_3 nanoparticles. *Journal of Water Process Engineering*, 44 (102376). Doi.org/10.1016/j.jwpe.2021.102376.

Tijani, J.O., Odeh, E.I., Mustapha, S., Egbosuba, T.C., Daniel, A.I., Abdulkareem, A.S., & Muya, F.N. (2022). Photocatalytic, electrochemical, antibacterial and antioxidant behavior of carbon-sulphur co-doped zirconium (IV) oxide nanocomposite. *Cleaner chemical Engineering*, 3 (100034), doi.org/10.1016/j.clce.2022.100034.

Tivol, W. F. (2020). Selected area electron diffraction and its use in structure determination. *Microscopy Today*, 18, (04), 22 - 28. Doi:10.1017/s1551929510000441.

Toston, S., Camarillo, R., Martinez, F., Jimenez, C.,& Rincon, S. (2017). Supercritical synthesisofplatinum-modified titanium dioxide for solar fuel production from carbon dioxide.*Chinese Journal of Catalysis*, 38 (1): 636-650.

Tomul, F., Arslan, Y., Kabak, B., Trak, D., Kendüzler, E., Lima, E. C., & Tran, H. N. (2020). Peanut shells-derived bio chars prepared from different carbonization processes: comparison of characterization and mechanism of naproxen adsorption in water. *Science of the Total Environment*, 726, 137828.

Turksoy, R., Terzioglu, G., Yalcin, I.E., TurksoyTerzioglu, O.,and Demir, G. (2021). Removal of heavy metals from textile industry wastewater. *Frontiers in Life Sciences and Related Technologies*, 2(2), 44 – 50.

Uko, C.A., Tijani, J. O., Abdulkareem, S. A., Mustapha, S., Egbosiuba, T. C., & Muzenda, E. (2022). Adsorptive Properties of MgO/WO_3 nano adsorbent for selected heavy metals removal from indigenous dyeing wastewater. *Journal of Process Safety and Environmental Protection*, 162, 775-794, doi.org/10.1016/j.psep.2022.04.057.

Vakilinezhad, M.A., Tanha, S., Montaseri, H., Dinarvand, R., Azadi, A., & Javar, A. (2018).Application of response surface method for preparation, optimization and characterization of nicotinamide loaded solid lipid nanoparticles. *Advanced Pharmaceutical Bulletin*, 8 (2), 245-256.

Wang, L., Huang, T., Yang, G., Lu, C., Dong, F., Li, Y., & Guan, W. (2020). The precursor guided hydrothermal synthesis of $CuBi_2O_4$/WO_3 heterostructure with enhanced photoactivity under simulated solar light irradiation and mechanism insight. *Journal of Hazardous Material*, 120956 doi.org/10.1016/j.jhazmat.2019.120956.

Wang, J., Liu, G., & Du, Y. (2013). Mechanochemical synthesis of sodium tungsten bronze nanocrystalline powders. *Materials letters*, 57, pp 3648-3652 doi:10.1016/S0167577X (03)00142-3.

Wang, Q., Zhu, S., Liang, Y., Cui, Z., Yang, X., Liang, C., & Inoue, A. (2017). Synthesis of Br- doped TiO2 hollow spheres with enhanced photocatalytic activity. *Journal of Nanoparticle Research,* 19(2). doi:10.1007/s11051-017-3765-2.

Wanjun, M.U., Qianhong, Y.U., Xingliang, L.I., Hongyuan, W., &Yuan, J. (2016). Hydrothermal synthesis of WO_3 nanowires in the presence of guanidine sulfate and its photocatalytic activity. *Journal of Wuhan University of Technology-Material Science*, 31(4) 731–735.

Wen, J., Xie, J., Chen, X., and Li, X. (2016). A review on g-C_3N_4 -based photocatalysts. *Applied Surface Science*, 391, 72–123. doi: 10.1016/j.apsusc.2016.07.030.

World Health Organization (2017). Safely Managed Drinking Water: Thematic Report on Drinking Water.

Wu, C. M., Naseem, S., Chou, M. H., Wang, J. H., & Jian, Y. Q. (2019). Recent advances in tungsten-oxide-based materials and their applications. *Frontiers in Materials,* 69,(49) doi:10.3389/fmats.2019.00049.

Xu, Y. J. (2021). Promises and challenges in photocatalysis. *Frontiers in Catalysis,* doi: 10.3389/fcts.2021.708319.

Yalcin, I.E., Ozyigit, I. I., Dogan, I., Demir, G., andYarci, C. (2020). Using the Turkish red pinetree to monitor heavy metal pollution. *Polish Journal of Environmental Studies*, 29(5),3881-3889.

Yaseen, D. A., & Scholz, M. (2018). Textile dye wastewater characteristics & constituents of synthetic effluents: a critical review. *International Journal of Environmental Science and Technology.* doi:10.1007/s13762-018-2130-z.

Yaseen, D. A., & Scholz, M. (2019). Textile dye wastewater characteristics and constituents of synthetic effluents: a critical review. *International Journal of Environmental Science and Technology.* doi:10.1007/s13762-018-2130-z.

Zappa, D. (2019). The influence of Nb on the Synthesis of WO_3 nanowires and the effects on hydrogen sensing performance. *Sensors,* 19(10), 2332. doi:10.3390/s19102332

Zhang, M., Cheng, G., Wei, Y., Wen, Z., Chen, R., Xiong, J., & Li, Z. (2020). Cuprous ion (Cu^+) doping induced surface/interface engineering for enhancing the CO_2 photoreduction capability of $W_{18}O_{49}$ nanowires. *Journal of Colloid and Interface Science*, 572, 306–317.doi: 10.1016/j.jcis.2020.03.090.

Zhang, M., Dong, H., Zhao, L., Wang, D., & Meng, D. (2019). A review on Fenton process for organic wastewater treatment based on optimization perspective. *Science of the Total Environment*.doi: 10.1016/j.scitotenv.2019.03.180.

Zhang, Y., Ram, M. K., Stefanakos, E.K., & Goswami, D.Y. (2012). Synthesis, characterization and applications of ZnO nanowires. *Journal of Nanomaterials*, doi:10.1155/2012/624520

APPENDICES

APPENDIX A: Kinetic Graphs

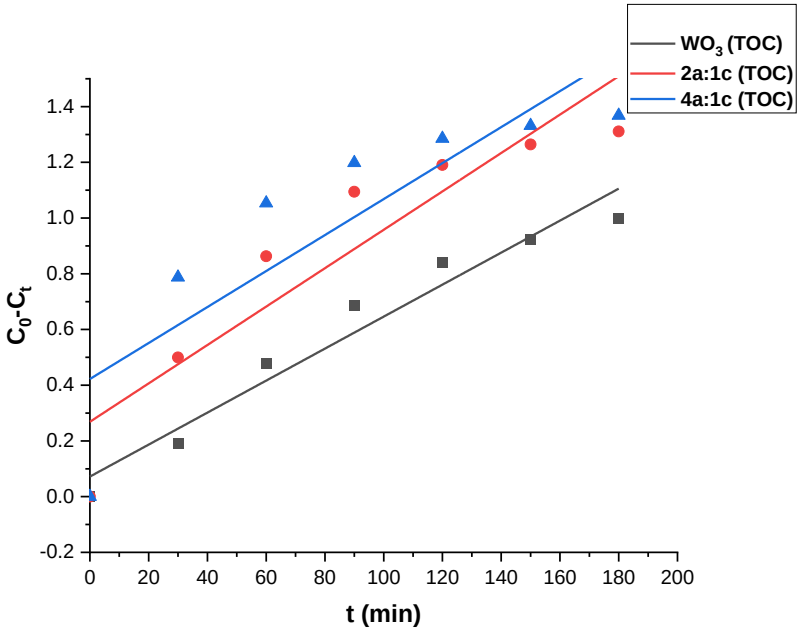

TOC zeroth order

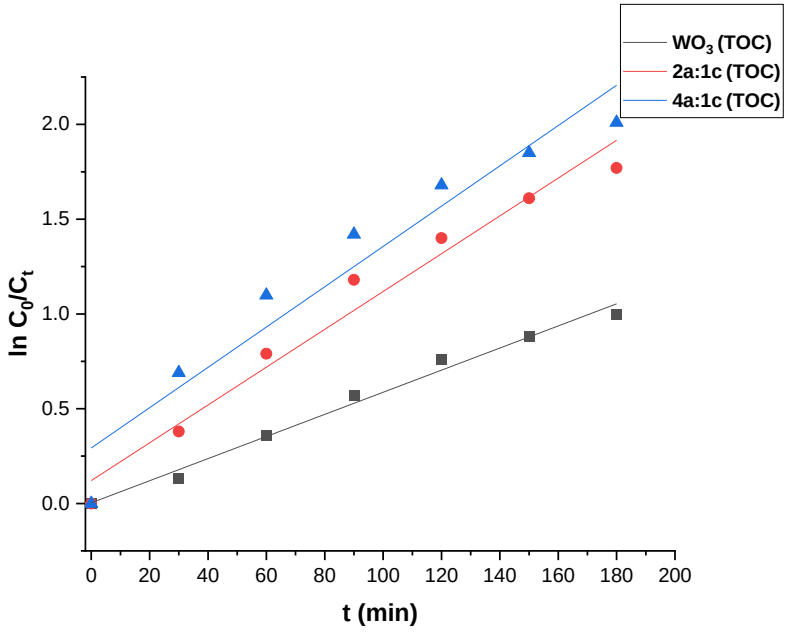

TOC first order

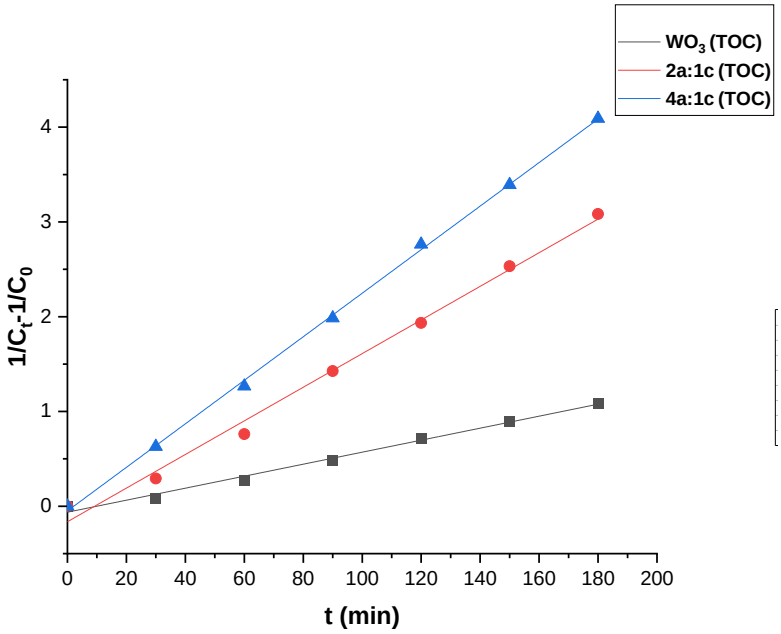

TOC second order

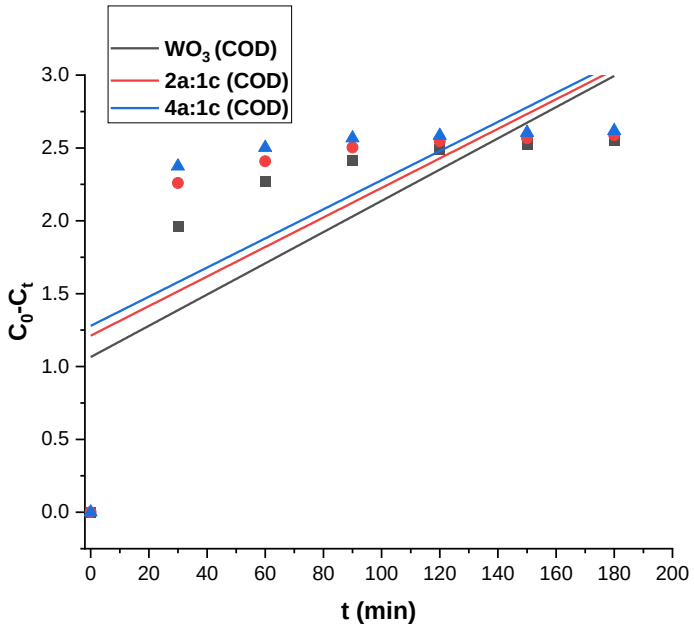

COD zeroth order

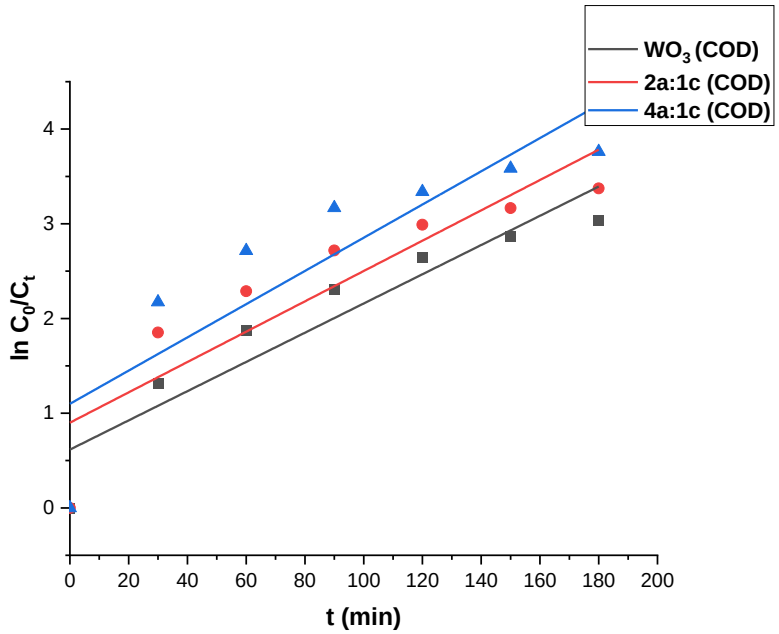

COD first order

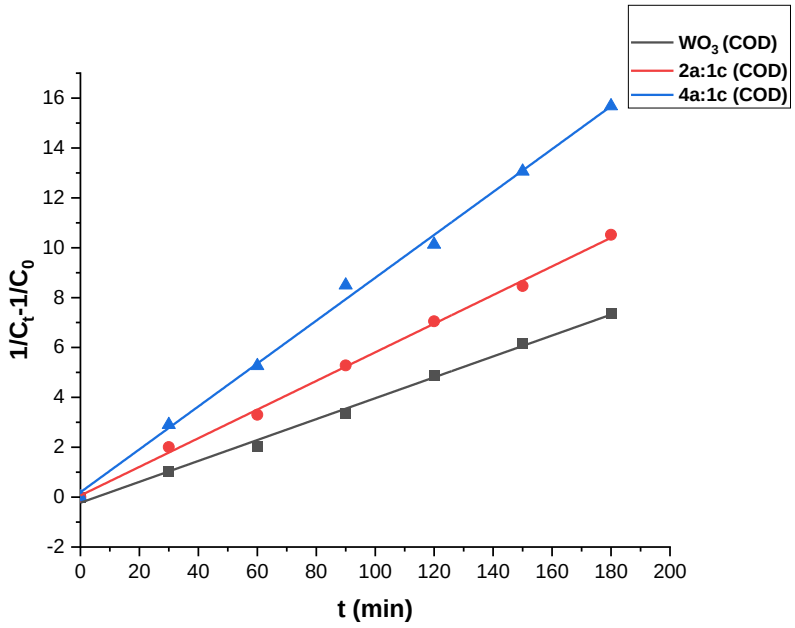

COD pseudo second order